MEASUREMENT OF THE LARGE-SCALE ANISOTROPY OF THE COSMIC BACKGROUND RADIATION AT 3 mm

LBL--17118

DE84 006774

Gerald Lewis Epstein
(Ph.D. Thesis)

Lawrence Berkeley Laboratory
University of California
Berkeley, California 94720

December 1983

DISCLAIMER

This research was supported by the Director, Office of Energy Research, Office of High Energy and Nuclear Physics, Division of High Energy Physics of the U.S. Department of Energy under Contract No. DE-AC03-76SF00098.

Measurement of the Large-Scale Anisotropy of the Cosmic Background Radiation at 3 mm

Gerald Lewis Epstein

Abstract

A balloon-borne differential radiometer has measured the large-scale anisotropy of the cosmic background radiation (CBR) with high sensitivity. The antenna temperature dipole anisotropy at 90 GHz (3 mm wavelength) is 2.82 ± 0.19 mK, corresponding to a thermodynamic anisotropy of 3.48 ± 0.24 mK for a 2.7 K blackbody CBR. The dipole direction, 11.3 ± 0.1 hours right ascension and $-5.7° \pm 1.8°$ declination, agrees well with measurements at other frequencies. Calibration error dominates magnitude uncertainty, with statistical errors on dipole terms being under 0.1 mK. No significant quadrupole power is found, placing a 90% confidence-level upper limit of 0.27 mK on the RMS thermodynamic quadrupolar anisotropy.

The cryogenically-cooled receiver has a double-sideband noise temperature of 135 K and a sensitivity of 12 mK for one second of integration time. Comparing two sky regions 45° from zenith and 180° apart in azimuth, it can resolve the dipole anisotropy in real-time as the balloon gondola rotates. In-flight calibrations show that gain stability is better than $\pm 1\%$. With flights from Palestine, Texas (31.8° north latitude) in November 1981 and April 1982, the radiometer has surveyed the sky between -15 and $+75$ degrees declination.

Since the magnitude of the dipole anisotropy induced by motion through the CBR depends on both the CBR intensity and its spectral index, anisotropy measurements at several frequencies provide information about the CBR spectrum. The ratio of the dipole magnitudes measured at 90 GHz by this experiment and at 24.5 GHz by another recent observation is consistent with a 2.7 K blackbody CBR but does not require such a spectrum. If the CBR spectrum is blackbody the two measurements establish a 90% confidence-level lower limit of 2.2 K on its temperature.

The region within five degrees of the galactic plane has been excluded from the fits. Including it changes the fitted parameters by less than one statistical standard deviation. Fitting to galactic models indicates that galactic emission averaged over the region within five degrees of the plane is on the order of 0.5 mK.

For Joel Orloff

Contents

Page

Chapter 1. Introduction and Theory 1
1.1 A Pocket History of Cosmology 1
1.1.1 Early Earth-Centered Models 1
1.1.2 The Copernican Revolutions 2
1.2 Modern Mathematical Cosmology 3
1.2.1 General Relativity 3
1.2.2 Big Bang Cosmologies 4
1.3 The Cosmic Background Radiation 5
1.3.1 CBR Prediction 6
1.3.2 Discovery 6
1.3.3 Properties 8
1.3.3.1 Spectrum 8
1.3.3.2 Polarization 10
1.3.3.3 Isotropy 10
1.4 Isotropy of the CBR 10
1.4.1 Isotropy of the Universe 10
1.4.1.1 Chaotic Cosmology 11
1.4.1.2 Anthropic Principle 11
1.4.1.3 The Inflationary Universe 13
1.4.2 Non-Intrinsic Sources of Anisotropy of the CBR 16
1.4.2.1 Peculiar Velocity and Antenna Temperature 16
1.4.2.2 Gravitational Radiation 18
1.4.3 Intrinsic Anisotropy 18
1.4.3.1 Anisotropic Cosmologies 18
1.4.3.2 Inhomogeneous Matter Distribution 20
1.4.4 Previous Experimental Results 20
1.4.4.1 Ground-Based Observations 20
1.4.4.2 Aerial Observations 21

Chapter 2. This Experiment 23
2.1 Design Considerations and Goals 23
2.1.1 Choice of Frequency 23
2.1.2 Choice of Technology 25
2.1.3 Choice of Platform 27

2.2 Radiometer Description . . . 27
2.2.1 Radiometer Hardware . . . 29
2.2.1.1 Cryogenic Temperature Components . . . 29
2.2.1.2 Non-Cryogenic Temperature Components . . . 33
2.2.2 Support Equipment . . . 35
2.2.2.1 Magnetometers . . . 35
2.2.2.2 In-Flight Calibrator . . . 36
2.2.2.3 Power . . . 36
2.2.2.4 Temperature Regulation . . . 36
2.3 System Configuration . . . 37
2.3.1 Experiment and Gondola . . . 37
2.3.2 Balloon and Flight Train . . . 37

Chapter 3. System Operation . . . 42

3.1 Radiometer Performance . . . 42
3.1.1 Noise Temperature . . . 42
3.1.2 Calibration . . . 42
3.1.3 Operating Parameters . . . 43
3.1.4 System Testing . . . 43
3.1.4.1 Magnetic Dependence . . . 44
3.1.4.2 Radio Interference and Other Tests . . . 44
3.2 Data Collection . . . 44
3.2.1 Flight Scheduling . . . 44
3.2.2 July 1981 Flight . . . 45
3.2.3 November 1981 Flight . . . 47
3.2.3.1 Modifications . . . 47
3.2.3.2 Flight . . . 48
3.2.4 April 1982 Flight . . . 50
3.2.4.1 Modifications . . . 50
3.2.4.2 Flight . . . 52
3.2.5 November 1982 Flight . . . 53
3.2.5.1 Modifications . . . 55
3.2.5.2 Flight . . . 55
3.2.5.3 Post Mortem . . . 56

Chapter 4. Data Reduction and Processing . . . 59

4.1 Data Format . . . 59
4.2 Beam Positional Reconstruction . . . 60
4.3 Data Editing and Sky Coverage . . . 61
4.4 Offset Analysis and Removal . . . 62
4.5 Conversion to Antenna Temperature and Correction to Barycenter . . . 66

Chapter 5. Data Analysis . . . 68

5.1 Spherical Harmonic Fits . . . 68
5.1.1 Results . . . 68
5.1.2 Data Weighting . . . 70
5.1.3 Chi-Square Statistics and Hourly Averages . . . 71
5.1.4 Individual Flight Dipole Fits . . . 76
5.1.5 Galactic Effects and Models . . . 77
5.2 Sky Maps . . . 80

5.3 Systematic Error Analysis . . . 82
5.3.1 Errors of the First Kind . . . 84
5.3.1.1 Galactic Sources . . . 84
5.3.1.2 Interplanetary Sources . . . 85
5.3.1.3 Ionospheric Free-Free Emission . . . 86
5.3.1.4 Atmospheric Molecular Emission . . . 86
5.3.1.5 Ground Pickup . . . 87
5.3.1.6 Balloon Contributions . . . 89
5.3.1.7 Synchronous System Modulations . . . 89
5.3.2 Errors of the Second Kind . . . 90
5.3.2.1 Calibration Uncertainty . . . 90
5.3.2.2 Pointing Errors . . . 91
5.4 Summary and Conversion to Thermodynamic Temperature . . . 91

Chapter 6. Interpretation . . . 93
6.1 Dipole Anisotropy . . . 93
6.1.1 Direction . . . 93
6.1.2 Magnitude . . . 95
6.1.3 CBR Spectral Distortion . . . 96
6.1.4 Solar Velocity . . . 101
6.2 Quadrupole Anisotropy . . . 105
6.3 Galactic Emission . . . 107
6.4 Summary . . . 108

Appendix A. Relativistic Flux Transformation . . . 109
A.1 Phase Space Density . . . 109
A.2 Intensity . . . 110

Appendix B. Radiometers . . . 112

Appendix C. Calibration . . . 115
C.1 Primary Calibration . . . 115
C.2 Corrections . . . 116
C.3 Stability of and Error in Calibration . . . 117

Appendix D. Linear Least Squares Estimation . . . 121
D.1 Best Fit Solution . . . 121
D.2 Uncertainty in Fitted Parameters . . . 122
D.3 Comparison of Independent Solutions . . . 123

Appendix E. Generation of Sky Maps . . . 125
E.1 Normal Equations . . . 125
E.2 Gauss-Seidel Sparse Matrix Inversion . . . 127
E.3 Jacobi Iterative Method . . . 128
E.4 Non-Iterative Method . . . 129

Appendix F. Radiometer Parts . . . 130

Appendix G. Azimuthal Anisotropy Coefficients . . . 131

Acknowledgements . . . 133

References . . . 135

Figures

Page

Figure 1.1. Woody-Richards Spectrum 9

Figure 1.2. $\Delta T_a/\Delta T$ 19

Figure 2.1. CBR Signal and Competing Backgrounds 24

Figure 2.2. Calculated Zenith Atmospheric Emission at 30 km 26

Figure 2.3. General Differential Radiometer Block Diagram 28

Figure 2.4. Block Diagram of the 90 GHz Anisotropy Radiometer 30

Figure 2.5. Antenna Beam Patterns 31

Figure 2.6. Radiometer Profile 38

Figure 2.7. Perspective View of Gondola 39

Figure 2.8. Balloon and Flight Train 41

Figure 3.1. November 1981 and April 1982 Flight Paths 49

Figure 3.2. Real-time Dipole Signal 51

Figure 3.3. Northern Sky Coverage 54

Figure 3.4. Reward notice for Gondola 57

Figure 4.1. Density of Sky Coverage 63

Figure 4.2. November 1981 Flight Data 64

Figure 4.3. April 1982 Flight Data 65

Figure 5.1. Hourly Sine and Cosine Anisotropy Coefficients 73

Figure 5.2. Hourly Sine and Cosine Residuals 74

Figure 5.3. HI Emission in the Northern Sky 79

Figure 5.4. Reconstructed 90 GHz Skymap 83

Figure 6.1. Consistency of 24.5 GHz and 90 GHz Dipole Anisotropies as a function of T_{CBR} . . . 99

Tables

Page

Table 1.1. Dipole Anisotropy Measurements 21

Table 5.1. Spherical Harmonic Basis Functions 69

Table 5.2. Global Dipole-plus-Quadrupole Fit 70

Table 5.3. *Dipole-only Anisotropy from Hourly Coefficients* 72

Table 5.4. Dipole-plus-Quadrupole Anisotropy from Hourly Coefficients 76

Table 5.5. Dipole-only Fits 78

Table 5.6. Effects of Galactic Cuts 80

Table 5.7. Effects of Galactic Models 81

Table 5.8. Contributions to Total Error 92

Table 5.9. Dipole-plus-Quadrupole Anisotropy at 90 GHz 92

Table 6.1. 90 GHz Dipole Anisotropy 94

Table 6.2. Comparison of Dipole Anisotropies 95

Table 6.3. Measured and Predicted Dipole Anisotropies 98

Table 6.4. Comparison of Dipole Anisotropies 100

Table 6.5. Solar Peculiar Velocity 103

Table 6.6. Comparison of Quadrupole Anisotropies 106

Table C.1. Pop-up Calibrator Ground Observations 120

Chapter 1

Introduction and Theory

People have speculated about the nature of their surroundings for as long as they have been aware of them. Quantitative cosmology, requiring accurate observations as well as world models which motivate and provide interpretation for observations, is somewhat more recent.

The earliest universe models were animistic — early man imbued his surroundings with spirits and demons based upon his own motivations and emotions. Magical explanations gave way to mythological ones as civilizations developed, and systematic, if not physical, descriptions were given for the nature of the world and its origin. Subsequent efforts to quantify and physically motivate descriptions of the universe represent what Harrison (1981) has called the transition from *anthropocentric* to *anthropometric* cosmologies. If not the center of the universe, man is at least a means by which the universe measures itself.

1.1 A Pocket History of Cosmology

1.1.1 Early Earth-Centered Models

Some of the earliest surviving attempts to relate astronomical observations to cosmological models, and to measure properties of the universe on scales larger than were immediately accessible, came from the ancient Greeks. By about the fourth century BCE, the Greek astronomers

and philosophers had generally agreed on a universe model consisting of a spherical, stationary earth suspended at the center of a rotating sphere which carried the stars (Kuhn, 1957). This world view, although not unanimously adopted, was elaborated by Aristotle and others and became institutionalized in Christian theology by Thomas Aquinas and his thirteenth century contemporaries.

1.1.2 The Copernican Revolutions

In 1543, Copernicus initiated a change in cosmological world view which removed the earth from its privileged location at the universal center. Successive displacements have expanded mankind's view of the universe and in many ways have further removed us from preferential status. Observations of non-uniformity in the distribution of stars led to the understanding that our sun was embedded within a larger system — the galaxy. In the late 1700's, Herschel placed the sun at the center of the Milky Way. By 1918, Shapley's observations of the anisotropic distribution of globular clusters showed the sun's actual position to be in the outskirts of our galaxy. The question of whether our "Island Universe" was unique or was rather one of many similar systems was resolved by Hubble's observations of the spiral nebulae, which showed them to be galaxies in their own right located far outside our own. Hubble's further discovery that the recession velocity observed for a galaxy was proportional to its distance established the idea of an expanding universe.

Hubble's Law, that recession velocity equals a constant H_0 times distance, does not mandate a privileged location for our galaxy. In a homogeneous, isotropically expanding universe, observers at all locations will find the recession velocities of other galaxies to be proportional to their distances. For each observer, however, there will be a unique *comoving* frame of reference in which this proportionality between distance and velocity is independent of direction. The frame of reference defined by our galaxy, then, *is* special to the extent that this isotropy holds.

1.2 Modern Mathematical Cosmology

Modern cosmological models have taken, as their basis, what was stated by Einstein and developed by Milne (1933) as

The Cosmological Principle:

All places in the universe are equivalent.

This is merely the Copernican idea that we do not possess a privileged status or location, and that the universe at large scales is *homogeneous*. Since we can only indirectly examine the distant universe, the Cosmological Principle must be postulated: it cannot be experimentally verified. Some models had adopted the stronger postulate (Bondi and Gold, 1948) of

The Perfect Cosmological Principle:

All places and times in the universe are equivalent.

However, the steady-state models resulting from this assumption have not been able to explain the observed evidence of change in the universe. As one looks farther out in space (and therefore further back in time), the universe looks different, so the present is not equivalent to the past. The cosmic background radiation, discussed below and the main subject of this thesis, gives perhaps the clearest evidence of such evolution.

1.2.1 General Relativity

Einstein's General Theory of Relativity provides the mathematical framework in which to test and express models describing the nature of our universe on the largest scales and earliest times. The theory relates how the geometry of space-time influences the mass distribution contained within it, and how the mass in turn determines the geometry. Within General Relativity, different assumptions concerning the mass distribution and overall structure of the

universe can be codified into different cosmological models; the features and predictions of the different models can then be compared with observations.

1.2.2 Big Bang Cosmologies

The simplest cosmological models describe universes which are homogeneous and isotropic. All points are equivalent, and at any point all directions are equivalent. Robertson and Walker showed in 1935 and 1936 (Misner *et al.*, 1973) that in all such universes, space-time can be separated into a curved three-dimensional space and a fourth time coordinate which can be consistently defined by any comoving observer. The geometry of space is determined by a *distance scale parameter* R which is a function only of time, being independent of position. The expansion or contraction of the universe, represented by the time evolution of the scale parameter, is determined by the distribution of matter and energy.

The "hot big bang" cosmology, which today is the most widely accepted description of the history and large-scale structure of our universe, is built upon on a Robertson-Walker space-time. It represents a class of solutions to the Einstein equations derived by A. Friedmann in 1922 and G. Lemaître in 1927 (Misner *et al.*, 1973) in which the universe expands and cools from an initial state of extreme temperature and density. Hubble's Law is a necessary consequence of the expansion of the universe embodied in these models.

In its barest form, a big bang universe model begins in a singularity; its subsequent properties are parameterized by elapsed time as measured by comoving observers. A more convenient parameter for many purposes is the ratio of the distance scale parameter R at a given epoch t_0 to its value at some other time t. Taking t_0 as the present time, this ratio can be shown to be equal to the ratio between the wavelength of a photon now, measured by a local comoving receiver, to its wavelength at time t, measured by a distant comoving observer:

$$\frac{\lambda(t_0)}{\lambda(t)} \equiv (1 + z(t)) = \frac{R(t_0)}{R(t)} \tag{1.1}$$

The first identity defines the *red shift parameter* z.

Another important parameter in Robertson-Walker universes describes the matter density. In the simplest models, universes having less than *critical density* will always expand following the initial singularity; space is *open* (infinite) and negatively curved. Universes having greater than the critical density will eventually stop expanding and will recontract into a "big crunch"; space in these universes is *closed* (finite) and positively curved. Universes having exactly critical density will always expand, but at an ever decreasing rate; space is infinite and flat. The ratio between the actual density of the universe and the critical density is denoted Ω, so $\Omega = 1$ is the value separating open from closed universes. Relativity theory, cosmology, and big bang models are described at various levels in many works (Misner *et al.*, 1973; Weinberg, 1972; Weinberg, 1977; Silk, 1980, to give just a few).

1.3 The Cosmic Background Radiation

Whether or not big bang models can validly be extrapolated all the way back to a singularity at $t = 0$, they have had great success in explaining many features of the universe today. The cosmic background radiation (CBR), a nearly isotropic, nearly blackbody radiation field giving the universe an effective temperature of about 3 K, has a natural interpretation as highly red-shifted thermal radiation remaining from a much earlier epoch. When it was some nine orders of magnitude hotter, this radiation was responsible for photo-dissociating deuterium which would otherwise have formed in the early universe. As a result, the combination of protons and neutrons into more stable heavier nuclei was prevented. Deuterium could persist when the temperature of the radiation field dropped below about 10^9 K, enabling further nucleosynthesis in which essentially all neutrons then present became bound into helium nuclei. The helium

mass fraction of the universe today, thought to be between 0.20 and 0.25 (Yang *et al.*, 1979), is consistent with this scenario.

The radiation field continued to maintain thermal equilibrium with matter until the universe expanded and cooled another six orders of magnitude. At the epoch of *recombination*, when the temperature had dropped to about 4000 K, the ionized plasma formed neutral hydrogen and helium and broke thermal contact with the radiation.

1.3.1 CBR Prediction

Several papers written in the late 1940's suggested that the universe may have passed through a hot early stage in which heavy elements were formed via thermonuclear reactions. Gamow (1946) argued the necessity of considering non-equilibrium nucleosynthetic processes in an expanding universe. Accounting for expansion time scales, Gamow (1948) showed that particle number densities of about 10^{18} cm^{-3} at temperatures of 10^9 K would be required in order for an appreciable fraction of protons and neutrons to form heavier nuclei. These conditions represent a universe dominated by radiation. Alpher and Herman (1949) calculated that the present temperature of that radiation would be on the order of 5 K.

At about the same time, experimental apparatus capable of measuring thermal radiation in the microwave band was being developed by Dicke at the MIT Radiation Laboratory (Dicke, 1946). In the process of making atmospheric absorption measurements, Dicke and colleagues put a limit of 20 K on the cosmic radiation temperature at three wavelengths near 1 cm (Dicke *et al.*, 1946).

1.3.2 Discovery

Detection and identification of the cosmic background radiation came some two decades

later. In 1965, Penzias and Wilson at Bell Laboratories reported finding an effective zenith noise temperature 3.5 ± 1.0 K higher than expected at 7.3 cm wavelength (Penzias and Wilson, 1965). The excess power was "isotropic, unpolarized, and free from seasonal variation" to the limits of their observation.[1] A companion paper by Dicke, Peebles, Roll, and Wilkinson (1965) from Princeton University suggested a cosmological origin for this power as greatly red-shifted blackbody radiation which had been in thermal equilibrium with ionized matter in the early universe.

The Princeton research had originated independently of the work at Bell Labs. Dicke had been considering oscillating universe models in which elements generated in one cycle would be destroyed by the extremely high temperatures occurring in the next contraction. By the summer of 1964, Dicke realized that red-shifted blackbody radiation remaining from a hot epoch, if present, should be observable. A literature search for existing upper limits to the temperature of a cosmological radiation field yielded the 20 K figure Dicke himself had made in the 1940's, as well as a limit of 15 K set in 1961 by the total system temperature of the apparatus later used by Penzias and Wilson (Wilson, 1979). To extend these results, Roll and Wilkinson of the Princeton group constructed a radiometer to measure cosmic background radiation at 3.2 cm. This experiment was in progress when news of the Bell Labs discovery reached Princeton. Roll and Wilkinson's publication, within a year of the initial CBR discovery papers, reported a temperature of 3.0 ± 0.5 K at over twice the frequency of the Penzias and Wilson observation and strongly supported the thermal origin of the radiation (Roll and Wilkinson, 1966 and 1967). The highly thermal and highly isotropic nature of the CBR, as confirmed by these and subsequent measurements, is generally taken as confirmation of its primordial origin.

[1]The limits on isotropy and polarization in the original detection of the CBR, not explicitly stated in Penzias and Wilson (1965), were 0.3 K and were independent of most of the errors contributing to the 1.0 K uncertainty in the CBR absolute temperature (Wilson 1979).

1.3.3 Properties

The CBR was quickly realized to be one of the few directly accessible probes of conditions and events in the early universe. Therefore, characterizing the CBR's properties as completely as possible became a high priority. Weiss (1980) has reviewed the status of CBR observations in the past twenty years.

1.3.3.1 Spectrum

Any distortion of the CBR spectrum from a purely thermal form would be of great interest since it might provide information about physical processes occurring in the early universe. In the low-frequency Rayleigh-Jeans region, the spectrum is consistent with a blackbody having a temperature (given by the weighted average of 21 measurements between 0.33 and 12 cm wavelength) of 2.76 ± 0.07 K (Smoot *et al.*, 1983; Weiss, 1980). At and above the peak, the measurement of Woody and Richards (1979) indicates a higher flux than the Rayleigh-Jeans measurements and shows deviation from a thermal spectrum at the two standard deviation level. The Woody-Richards spectrum has excess flux near the peak and a deficiency above when compared to the 2.96 K blackbody spectrum having the same integrated flux. Figure 1.1 shows the Woody-Richards spectrum along with some lower frequency measurements and a 2.96 K blackbody curve.

An indirect, but potentially quite precise, measurement of the CBR intensity at specific frequencies near and above the peak is obtained from interstellar cyanogen observations. The relative strengths of two lines in the CN absorption band at 3874 Å — one from the ground state and the other from the first rotationally excited state — permit determination of the relative populations of the states and hence of the CN excitation temperature. Since excitation mechanisms other than the CBR are possible, the excitation temperature is an upper bound to

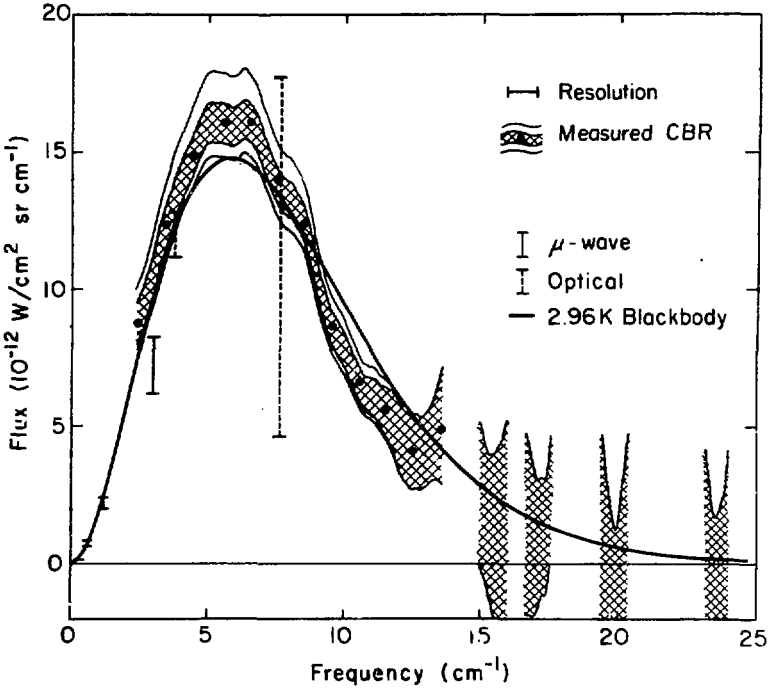

Figure 1.1. Woody-Richards spectrum (Woody and Richards, 1979).

the CBR temperature at the frequency of the transition linking the cyanogen states. Subsequent to the Woody-Richards measurement, Meyer and Jura (1984) have made a high signal-to-noise measurement of this excitation and find $T_{CBR} \leq T_{ex} = 2.73 \pm 0.04$ K at 11.4 GHz, in disagreement with the Woody-Richards results.

1.3.3.2 Polarization

Any anisotropy intrinsic to the CBR which was established prior to the CBR's last scattering will be accompanied by a net linear polarization due to the polarization dependence of Thompson scattering (Rees 1968). Lubin, Melese, and Smoot (1983b) have placed a 95% confidence level limit of 0.2 mK on any linearly polarized component at 9 mm wavelength.

1.3.3.3 Isotropy

The present universe is quite transparent to microwave radiation, so the CBR we measure today has propagated freely from regions of the universe where the line-of-sight optical depth becomes significant. Its angular intensity distribution carries information about the structure of the universe on these scales. A dipole anisotropy of a part in one thousand of the CBR, attributable at least in part to our motion relative to a comoving frame, is by now well established (Smoot *et al.*, 1977; Gorenstein, 1978; Corey, 1978; Cheng *et al.*, 1979). Further investigation of angular anisotropy in the CBR forms the subject of this work.

1.4 Isotropy of the CBR

1.4.1 Isotropy of the Universe

There are many mechanisms which can generate anisotropy in the cosmic background radiation. Indeed, the greater challenge for theoretical cosmology is explaining the CBR's unifor-

mity. In standard big bang models, which treat the early universe as a radiation-dominated Robertson-Walker space-time, radiation reaching us from opposite parts of the sky comes from regions which have never been in causal contact.[2] Without postulating specialized initial conditions, it is hard to understand why these independent regions should be at the same temperature.

1.4.1.1 Chaotic Cosmology

Misner (1968) hoped to account for the present isotropy by showing that in a large class of homogeneous but anisotropic models, initial anisotropy would damp out due to dissipative processes such as neutrino viscosity. However, it was later shown that the temperature of the cosmic background radiation itself limits the amount of dissipation that could have occurred in the very early universe (Barrow and Matzner, 1977). Collins and Hawking (1973a), examining the same question of whether initially homogeneous but anisotropic universes evolve towards isotropy, showed that those which do form a set of measure zero in the space of all spatially homogeneous models. In other words, a given chaotic universe model will in general *not* become isotropic. Instead, Collins and Hawking proposed an alternate explanation for the observed isotropy of our universe: only universes expanding just fast enough to avoid recollapse, those being the ones which approach isotropy, can form galaxies containing observers who measure isotropy.

1.4.1.2 Anthropic Principle

This last argument is an invocation of what Carter (1974) termed

The Anthropic Principle:

> What we can expect to observe must be restricted by the conditions necessary for our existence as observers.

[2] Taking the surface of last scattering to be at a red shift of 1500, regions more than $3\sqrt{\Omega}$ angular degrees apart on that surface are causally disconnected (Weinberg, 1972, p. 525).

Carter sees this as a qualification of the Copernican principle discussed earlier. We do not occupy a central location in the universe, but the fact that we exist indicates that our situation is necessarily privileged to some extent.

Many authors have used anthropic arguments to explain what otherwise might need to be attributed to coincidence or to undiscovered physics. Consider two very large but apparently independent dimensionless numbers: the ratio of the electrical to gravitational forces between proton and electron, and the Hubble time, or age of the universe, measured in the length of time light takes to cross a classical electron radius. Both are on the order of 10^{40}. Dirac's Large Number Hypothesis explains their near-equality by postulating a physical relationship which sets them equal. Dicke (1961), on the other hand, reasons that our very presence requires the existence of heavy elements. We cannot measure a universe to be younger than the lifetime of the stars required to produce those elements, which is on the order of several billion years. However, if the universe were much older than that, all stars and all observers would have died out. Therefore, we measure its age to be 10^{40} "light-electrons" old because we are here to measure it.

Carr and Rees (1979) discuss a number of relationships between mass, length, and time scales in the universe. Many of these relationships have straigbtforward physical derivations; others can be "explained" only by invoking anthropic arguments. Carr and Rees find the latter approach somewhat unsatisfying, from a physical point of view, for three reasons: the anthropic explanations supply *post-hoc* rationalizations rather than predictions, they may embody overly anthropomorphic assumptions concerning what is necessary for the existence of observers, and they cannot provide exact values for the constants that they are able to relate by order of magnitude. Nevertheless, Carr and Rees feel that the antbropic explanation was the only candidate (apart from the less general Large Number Hypothesis) able to account for the "remarkable coincidences" displayed by nature.

1.4.1.3 The Inflationary Universe

At least one of these "remarkable coincidences" of cosmology, the isotropy of the CBR, may have found a more physical justification in recent theoretical work. Isotropy is a puzzle in standard models since, as has been mentioned, different areas on the surface of last scattering are causally disconnected; no signal traveling from any common origin can have standardized all of them. However, the size of the region to which a given point can be causally connected, its *particle horizon*, depends on the rate of expansion of the universe.

If we lived in a static universe which had a finite age t, our present particle horizon would have a proper radius of ct. Light signals which left points on our horizon at $t = 0$ would now just be arriving after having traversed the distance ct between the horizon and us. In an expanding universe, the relationship between time and horizon size is more complicated. Our particle horizon at the present time still represents the portion of space which we are aware of — that portion from which we have received light signals. But the present location of the points on that horizon depends on how the universe expands during the time that the light is traveling to us. Furthermore, the size of the largest region which could have been causally connected at some earlier time, which is the particle horizon size for an observer at that time, depends on the nature of the expansion.

The scale parameter in early Friedmann-Robertson-Walker universes (standard big bang models) grows as $t^{\frac{1}{2}}$, for a radiation-dominated universe, or $t^{\frac{2}{3}}$, for a matter-dominated one. This is not fast enough to permit all points on the surface of last scattering of the cosmic background radiation to be inside each other's particle horizons at the time the CBR was last scattered. But if the scale parameter were to have grown exponentially rapidly for a period in the early universe, a very large region could be causally connected today. Extrapolating the present slower expansion rate back to the big bang, we greatly underestimate the size of the region which actually would have been in contact during and before the exponential growth.

Inflationary universe models (Guth, 1981; Press, 1981) isotropize the universe by splicing just such a period of exponential growth into the early universe. To see how this period arises, we must examine the concept of the *cosmological constant*. In the early twentieth century, when Einstein formulated the General Theory of Relativity, the universe was believed to be static. On discovering that only dynamic solutions existed to his original field equations, Einstein modified the equations by adding an additional term. This added cosmological constant represents a long-range repulsive force which just balances the gravitational attraction of mass over long distances, preventing collapse of the universe. It does so at the expense of destroying the equivalence of General Relativity to classical Newtonian gravitational theory in the limit of weak gravitational fields. After Hubble verified that the universe actually was expanding, Einstein abandoned the modification, later calling it "the biggest blunder of my life." (Misner *et al.*, 1972, p. 758).

The cosmological constant can be interpreted as a "vacuum" energy density attributable to free space, differing from ordinary matter or energy ("substance") density in that it has a negative effective pressure. The solution to the field equations for a universe having a cosmological constant, but devoid of matter, is exponential expansion. If there is a cosmological constant today, it must be sufficiently small so that its equivalent vacuum energy density is negligible compared to the mass-energy density of any system adequately described by Newtonian gravitation. Existing limits are sufficient to determine that the present dynamics of the universe are not dominated by a cosmological constant term.

However, according to certain particle physics grand unified gauge theories (GUTs), a large cosmological constant could have temporarily arisen in the very early universe. In these models, all non-gravitational interactions are equivalent at extremely high temperatures. When the universe cools below a critical transition temperature within a few orders of magnitude of 10^{28} K (10^{15} Gev), it undergoes a phase transition in which the strong interactions between quarks become distinguishable from the electroweak interactions among leptons. The symmetric

phase in which all interactions are equivalent, which is the minimum energy state at higher temperatures, becomes a "false vacuum" state which has a higher potential energy than the "true vacuum" state of broken symmetry. In the inflationary GUT models, the form of the vacuum potential is such that the universe becomes supercooled — it takes a relatively long time to evolve from the false vacuum to the true vacuum state. During that evolution, the potential energy of the false vacuum acts as a cosmological constant, and the universe undergoes a period of exponential expansion. As the universe reaches the true asymmetric vacuum state, the false vacuum energy is dissipated as heat, ending the exponential growth. The re-heated universe subsequently evolves according to the standard big bang models.

Inflationary scenarios are extremely attractive mechanisms for explaining the present isotropy of the universe. They also can explain some other presently outstanding cosmological puzzles. Recall that the difference between the dimensionless density Ω and unity is a measure of the curvature of space. In a spatially flat universe, $\Omega = 1$. Ω in our universe at present is most likely bounded by the limits 0.01 and 10 (Weinberg, 1972, p. 477–481; Misner *et al.*, 1972, p. 796–797); recent studies of galactic dynamics indicate a value on the order of 0.2 (Davis and Peebles, 1983a). Since Ω is on the order of one, space is close to flat. But the deviation between Ω and unity increases with time in big bang universes. Therefore, having Ω within two orders of magnitude of unity at present requires its value to have been within a part in 10^{15} of unity when the universe had a temperature of 10^{10} K -- thus, the flatness problem (Guth, 1981).

The exponential growth phase of inflationary scenarios solves the flatness problem. During that phase, the cosmological constant (representing vacuum, rather than substance, energy density) dominates the dynamics of the universe; the expansion rate then is exactly the rate for which the vacuum energy density is the critical density. Space in an exponentially growing universe is flat. During the phase transition ending the exponential growth period, vacuum energy emerges as substance (radiation or particles) which remains at the critical density. Space is flat

before and after the transistion, and it remains flat in the period of power-law expansion which follows. Inflationary models predict that the total density of the universe today should equal the critical density to very high accuracy.

Inflationary universe models, then, provide answers for some of the presently outstanding problems with conventional big bang models. They predict that the universe at present is critically dense, and more relevant to this thesis, that there should be no detectable intrinsic anisotropy in the CBR attributable to large-scale inhomogeneity in the early universe. The models are the subject of intense scrutiny by both particle physicists and cosmologists (Barrow and Turner, 1982).

1.4.2 Non-Intrinsic Sources of Anisotropy of the CBR

1.4.2.1 Peculiar Velocity and Antenna Temperature

At some level, we certainly expect to measure anisotropy in the CBR. Motion of the earth about the sun, the sun about the galaxy, and the galaxy relative to a comoving frame will introduce anisotropy into measurements of the CBR even if the CBR is isotropic in a comoving frame. Motion through a blackbody radiation field will preserve its blackbody spectrum but will give it an angle-dependent temperature (Peebles and Wilkinson, 1968). If Θ is the angle between the direction of observation and the direction of motion, the observed temperature is

$$T(\Theta) = T\frac{(1-\beta^2)^{\frac{1}{2}}}{(1-\beta\cos\Theta)} \tag{1.2}$$

where T is the temperature in the isotropic frame and $\beta = \frac{v}{c}$ is the dimensionless velocity of the moving observer relative to the isotropic frame. For small values of β, the expression can be linearized to yield

$$T(\Theta) = T(1+\beta\cos\Theta). \tag{1.3}$$

representing a first-order or dipole anisotropy with a fractional magnitude equal to β. In a blackbody radiation field of 2.7 K, a velocity of 330 km/sec induces a thermodynamic dipole anisotropy of 3 mK.

In general, consider the transformation of a radiation field described by intensity I (power per unit area per unit solid angle per unit bandwidth). At frequency ν_0 define the intensity spectral index α to be the logarithmic derivative $(\partial \log I \,/\, \partial \log \nu)$ at ν_0. If I is isotropic in some reference frame, the linearized intensity anisotropy in a frame moving at velocity β is given (see Appendix A) by

$$I' = I'_0(1 + \beta(3 - \alpha)\cos\Theta); \tag{1.4a}$$

$$\Delta I' = I'_0\beta(3 - \alpha) \tag{1.4b}$$

where $\Delta I'$ is the amplitude of the dipole anisotropy. Note that the spectral index as well as the velocity enter into the formula. In particular, an isotropic radiation field having an intensity proportional to ν^3 $(\alpha = 3)$ is isotropic in all frames: the frequency dependence $(\sim \nu^3)$ exactly balances the contraction of solid angle $(\sim \nu^2)$ and the transformation of photon energy $(\sim \nu)$ induced by the observer's motion.

A microwave radiometer measures power received in one polarization with a fixed collecting area, solid angle acceptance, and bandwidth. It is therefore directly measuring intensity I. Let the *antenna temperature* corresponding to intensity I measured at frequency ν be defined as

$$T_a = \frac{c^2}{2k\nu^2} I. \tag{1.5}$$

If measured in the Rayleigh-Jeans portion of the spectrum, the antenna temperature of a blackbody filling the beam of a microwave radiometer equals the blackbody's thermodynamic temperature. In the Wien limit, antenna temperature drops exponentially with frequency.

Letting x be the parameter $h\nu/kT$, the antenna temperature and thermodynamic temperature are related by

$$T_a = \frac{x}{e^x - 1} T, \text{ and} \tag{1.6a}$$

$$\Delta T_a = \frac{x^2 e^x}{(e^x - 1)^2} \Delta T. \tag{1.6b}$$

In principle, the frequency dependence of a motion-induced antenna temperature anisotropy permits the spectrum of a radiation field to be determined. Figure 1.2 shows how a CBR thermodynamic temperature anisotropy ΔT appears as a frequency-dependent antenna temperature anisotropy ΔT_a whose form is a function of the CBR spectrum. Plotted is the ratio ΔT_a to ΔT for both 2.7 K and 3.0 K CBR spectra.

1.4.2.2 Gravitational Radiation

An additional source of non-intrinsic anisotropy in the CBR would be the quadrupolar and smaller-scale distortion produced by long-wavelength gravitational radiation (Burke, 1975).

1.4.3 Intrinsic Anisotropy

1.4.3.1 Anisotropic Cosmologies

Large-scale anisotropy in the structure of the universe will produce red shifts dependent on direction. Hawking (1969) and Collins and Hawking (1973b) discuss the forms taken by the CBR due to rotation or vorticity, shear, and peculiar velocities in spatially homogeneous but anisotropic cosmological models. The CBR appearance due to a particular anisotropy of the universe is strongly dependent on the type of anisotropic model studied. For example, shear introduces a quadrupolar variation in the CBR in two particular anisotropic models; in other models the variation is more complex. In addition, the magnitude of induced anisotropy depends on how long ago the radiation was last scattered.

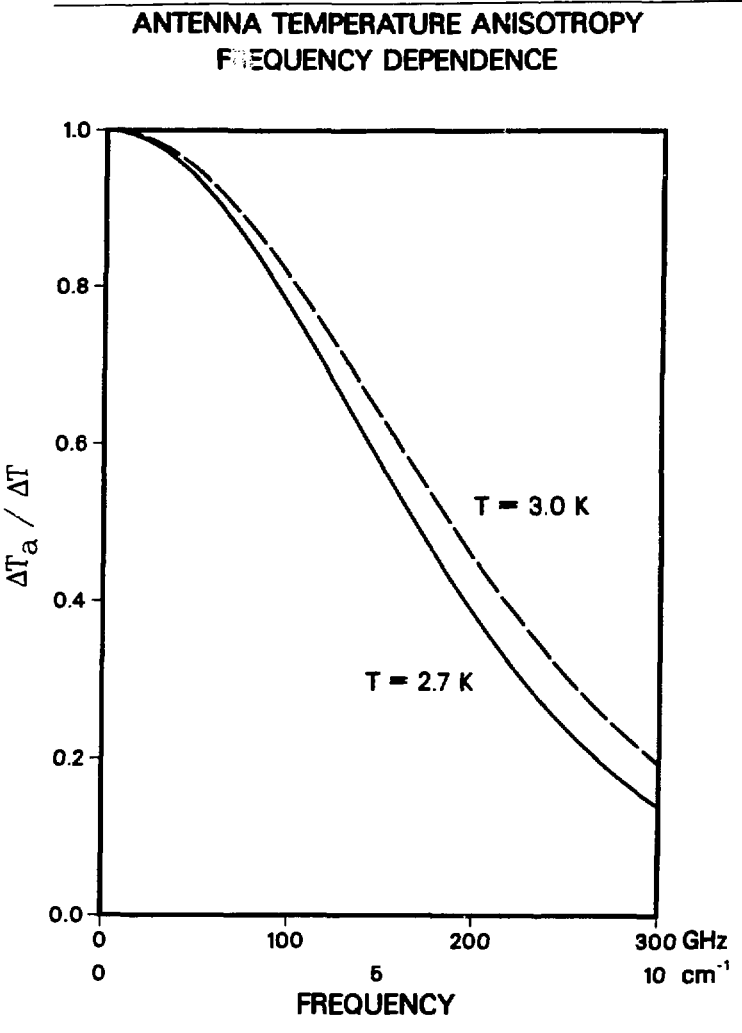

Figure 1.2. $\Delta T_a/\Delta T$ for 2.7 K and 3.0 K blackbody CBR spectra.

1.4.3.2 Inhomogeneous Matter Distribution

Matter inhomogeneity certainly exists today. Therefore, perturbations must have existed at some level in the early universe as well. They could have influenced the CBR in three ways — intensity (temperature) fluctuations on the surface of last scattering, differential red shifts due to velocity fluctuations of the last scatterers, and differential gravitational red shifts imparted by matter inhomogeneities between the surface of last scattering and the observer. Sachs and Wolfe (1967) used the last mechanism, along with the then-existing 1% upper limit on CBR anisotropy, to bound large-scale density fluctuations in the universe on scales of 1000 megaparsecs to be under 10%. Since then, considerable work has been done predicting what anisotropy in the CBR would be expected given various density distributions and cosmological models (e.g. Silk and Wilson, 1981; Peebles, 1982; Fabbri *et al.*, 1982; Hogan *et al.*, 1982).

1.4.4 Previous Experimental Results

Searches for large-scale CBR anisotropy have been undertaken since the discovery of the CBR in 1965. These are differential observations which directly compare power from different parts of the sky. Systematic environmental and instrumental effects are minimized by observing the same sky regions with different experimental configurations and differencing the measurements so that only CBR anisotropy contributes to the result. Results of previous measurements are given in Table 1.1. Only the most recent publication in ongoing series of experiments have been listed. The gap between 1971 and 1979 represents work which has been incorporated into the post–1979 publications.

1.4.4.1 Ground-Based Observations

The first anisotropy measurements were done at microwave frequencies (centimeter

Table 1.1. Dipole anisotropy measurements.

Source	Platform	Altitude (km)	Type[1]	ν (GHz)	λ (cm)	Dipole Magnitude[2] (mK)
Wilson and Penzias, 1967	Ground	0	R	4.1	7.32	<100
Partridge and Wilkinson, 1967	Ground	0	R	9.4	3.19	0.9 ± 2.1
Conklin, 1969	Mountain	3.8	R	8.0	3.75	1.6 ± 0.8
Boughn *et al.*, 1971	Ground	0	R	35.0	0.86	7.5 ± 11.6
Smoot and Lubin, 1979	Aircraft	20	R	33.0	0.91	3.1 ± 0.4
Fabbri *et al.*, 1980	Balloon	40	B	100-600	0.05 - 0.30	$2.9 \pm^{1.3}_{0.9}$
Muehlner and Weiss, 1980	Balloon	39	B	90-300	0.10 - 0.33	2.8 ± 0.8
Boughn *et al.*, 1981	Balloon	27	R	19.0	1.58	3.0 ± 0.8
				24.8	1.21	4.0 ± 0.3
				31.4	0.95	3.7 ± 0.3
				46.0	0.65	3.9 ± 1.0
Fixsen *et al.*, 1983	Balloon	25	R	24.5	1.21	3.18 ± 0.17
This work, 1983	Balloon	28	R	90.0	0.33	3.48 ± 0.23

[1] R = Radiometer; B = Bolometer

[2] Thermodynamic Temperature for $T_{CBR} = 2.7$ K

wavelengths) from the ground. Except for Conklin (1969), the ground-based observations provided upper limits. Conklin reported the first significant non-zero result for the equatorial 24-hour (dipole) anisotropy projected to 32 degrees declination. His result agrees with later observations but involved extrapolating a large galactic correction from lower frequency observations with a poorly known spectral index.

1.4.4.2 Aerial Observations

Definitive observations of CBR dipole anisotropy have all been made from the air. Radiometric observations have been done by the Princeton group from balloon-borne platforms (Corey, 1978; Cheng *et al.*, 1978; Boughn *et al.*, 1981; Fixsen *et al.*, 1983) and by the Berkeley

group from both the U-2 aircraft and balloons (Smoot *et al.*, 1978; Gorenstein, 1978; Lubin *et al.*, 1983a) Far-infrared bolometric observations have also been made from balloon-borne platforms (Weiss, 1980; Fabbri *et al.*, 1980) All aerial observations have measured the dipole anisotropy to have magnitude about 3 mK in roughly the same direction, although there are statistically significant discrepancies in magnitude and direction between experiments.

Radiometric anisotropy magnitudes in Table 1.1 have been converted from antenna temperature anisotropy to thermodynamic anisotropy according to equation 1.6b by assuming the CBR to have a thermal spectrum with a temperature of 2.7 K. Below 35 GHz, the ratio ΔT_a / ΔT is insensitive to the exact temperature or precise spectral shape of the CBR (Figure 1.2). At 90 GHz, the conversion factor of 0.81 becomes 0.85 if the CBR temperature is taken to be 3.0 K instead of 2.7 K. Conversion of the wideband bolometric infrared measurements to thermodynamic temperature is highly dependent on the detector frequency response and the assumed spectrum of the CBR; the assumptions made for the infrared works quoted here were not explicitly stated by the authors.

Fabbri *et al.* (1980) reported detection of a "quadrupole-like" anisotropy with magnitude $0.9^{+0.4}_{-0.2}$ mK. They were unable to characterize it in terms of second-order spherical harmonics due to insufficient sky coverage. Reanalysis of the data (Ceccarelli *et al.*, 1982) determined quadrupole coefficients and attributed at least part of the quadrupole to an extended infrared source; however, the reanalysis was still unable to specify the dipole and quadrupole anisotropies completely. Boughn *et al.*, (1981) reported significant quadrupolar anisotropy coefficients of 0.31 ± 0.15 mK and 0.54 ± 0.14 mK in the two second-order spherical harmonic components having twelve-hour periods in right ascension. This quadrupole detection was retracted in Fixsen *et al.* (1983), published simultaneously with the initial publication (Lubin *et al.*, 1983a) of the work reported here. The experiment reported in this thesis does not support claims of quadrupolar anisotropy in the cosmic background radiation.

Chapter 2

This Experiment

2.1 Design Considerations and Goals

The two principal goals of this experiment were a desire to measure the background radiation anisotropy with high sensitivity and to do so at a frequency significantly different from previous measurements. These two considerations, sensitivity and frequency, are not independent. The technology available to perform this experiment depends upon the operating wavelength, and the degree of sensitivity needed or desirable depends on what signal level is expected and what the competing backgrounds will be. The signal and the backgrounds are both frequency dependent.

2.1.1 Choice of Frequency

The most fundamental contaminant of measurements of the large-scale anisotropy of the cosmic background radiation is diffuse galactic radiation. Estimates of the galactic contribution to a seven-degree full width at half maximum (FWHM) beam on the galactic plane are identified in Figure 2.1. Since the galactic contributions have different frequency dependences from the CBR and from each other, comparison of measurements at different frequencies can in principle

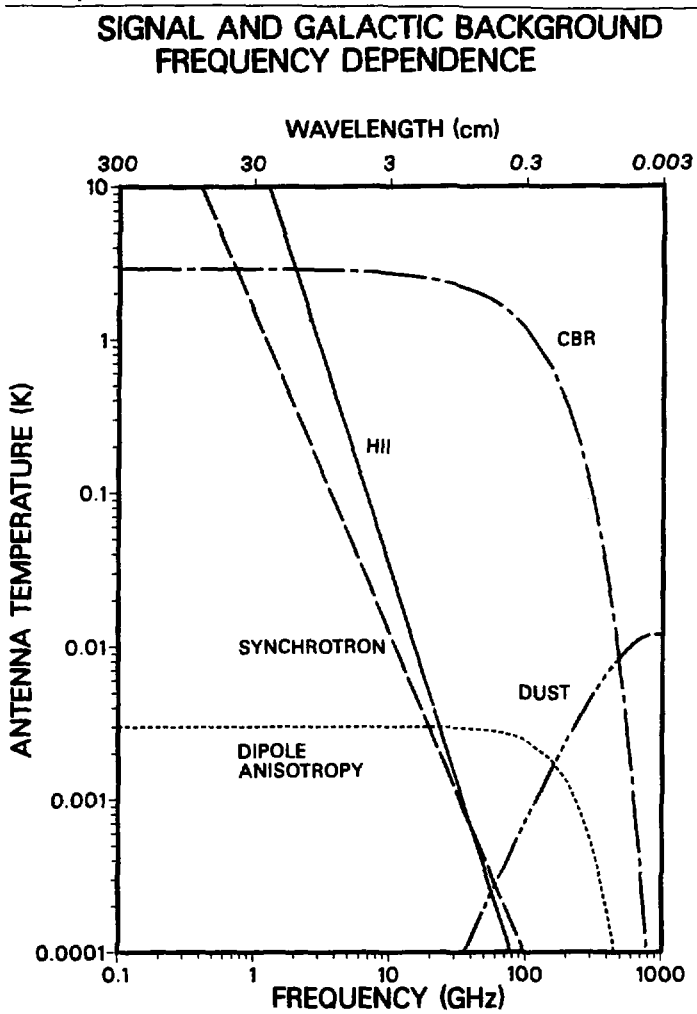

Figure 2.1. CBR signal and competing backgrounds. Galactic backgrounds are for a seven-degree beam on the galactic equator.

decouple the various contributions. This procedure is of course limited by the accuracy to which the frequency dependences are known.

Synchrotron radiation from electrons in the galactic magnetic field, and thermal brehmsstrahlung from ionized hydrogen regions, are the dominant contributions at centimeter wavelengths. In the infrared, thermal emission from interstellar dust predominates. If galactic radiation is significant, its angular distribution must be understood before attributing anisotropy to the CBR. Preferably, anisotropy measurements should be done at a frequency where the galactic contribution is minimized. Figure 2.1 indicates a window near 90 GHz where the total galactic emission is low. Exactly where this minimum occurs depends on how the dust emission is distributed spatially and spectrally.

Having a galactic window is of little use if one cannot see through the atmosphere. Figure 2.2 shows the calculated atmospheric zenith emission at 30 km altitude in the microwave region, indicating a window between two oxygen absorption peaks at 60 and 120 GHz. Within this window, the band between 86 and 92 GHz is protected for radio astronomy and was selected for this experiment.

2.1.2 Choice of Technology

Microwave technology is continually improving, both in sensitivity and in accessible frequencies. Development of high-performance millimeter and sub-millimeter radiometers has blurred the boundary between microwave and infrared. In the region where the two overlap, at a wavelength of about a millimeter, the distinctions are primarily in terminology and technique.

As to terminology, this microwave experimentalist will usually say the frequency of a 360 micro-electron-volt CBR photon is 90 GHz, whereas his infrared colleagues will label it 3 cm^{-1}. Differences in technique are more fundamental. A microwave receiver is a coherent detector —

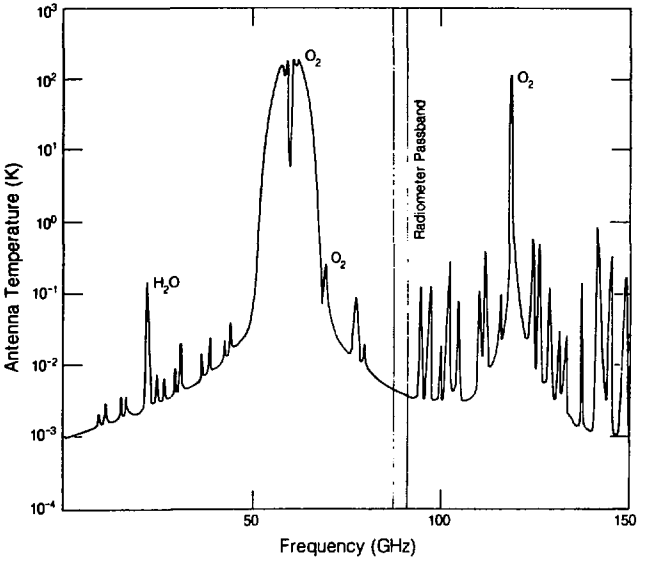

Figure 2.2. Calculated zenith atmospheric emission at 30 km. All unlabeled peaks are ozone lines.

it can preserve the phase of the incident signal. A bolometer used to detect infrared radiation is an incoherent device sensitive only to total incident power. In isotropy measurements, where ultimately only the power is measured, both types of devices can be used. This experiment uses a cryogenically-cooled radiometer, which can be made more sensitive than a bolometer in the region near 90 GHz. More importantly, a radiometer's passband can be defined much more precisely than can that of a bolometer, making it possible to take better advantage of windows between atmospheric emission peaks. The signal to noise ratio of a radiometer increases with the square root of the bandwidth of the detected radiation, whereas a bolometer's sensitivity is

directly proportional to its bandwidth. Therefore, the bolometer is better able to utilize large bandwidths.

2.1.3 Choice of Platform

The differential radiometers used to measure anisotropy compare incident intensity from two sky patches located at equal zenith angles. Atmospheric emission, to first order, contributes equally to both. However, atmospheric variation and misalignment of the apparatus will cause the actual atmospheric contributions to differ. By using a high-altitude platform, total atmospheric emission (and therefore differential atmospheric emission) is reduced to acceptable levels. At 30 km, the zenith atmospheric antenna temperature at 90 GHz is 4 mK.

The required altitudes can be reached by balloon, rocket, or satellite. Rocket flights do not last long enough to make sufficiently sensitive measurements. An orbiting platform is ideal; flight duration, sky coverage, and elimination of atmospheric background make a satellite experiment particularly attractive for measuring the CBR anisotropy. The Cosmic Background Explorer (Mather and Kelsall, 1980) has been under NASA development since 1974 to do so, but it will not be launched before 1987. This experiment was therefore designed to be carried by a scientific balloon.

2.2 Radiometer Description

The heart of this experiment is a cryogenically-cooled differential radiometer (Appendix B) which uses the sky for both source and reference. Such a device, with an output proportional to the difference in intensity between areas in the sky, permits anisotropy to be measured directly without the need to make absolute measurements to the 10^{-4} level. Figure 2.3 shows a general block diagram of a differential radiometer used in this configuration. Having the two radiometer

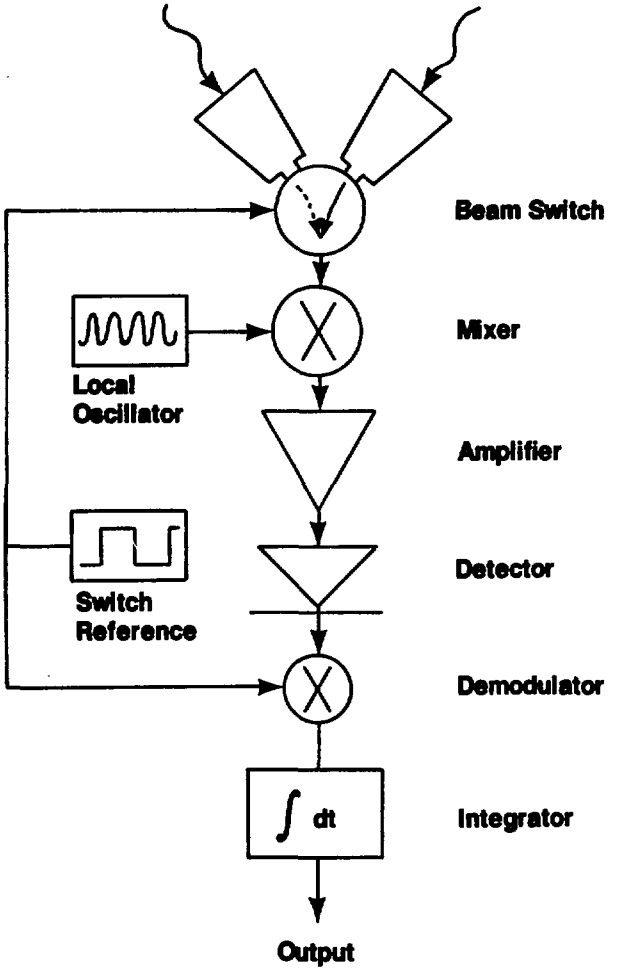

Figure 2.9. General differential radiometer block diagram.

fields of view at equal zenith angles balances residual atmospheric emission. Rotating the receiver, besides providing sky coverage, modulates anisotropy in the background radiation to distinguish it from asymmetry in the apparatus. Anisotropy will yield a difference signal which changes sign when the sky patches observed by each beam are interchanged; an asymmetry or offset will remain constant to the extent that the apparatus itself is unaffected by rotation. It is therefore very important to ensure that nothing internal to the receiver changes synchronously with rotation.

2.2.1 Radiometer Hardware

Since electronic waveguide switches at 90 GHz have high loss and would significantly degrade the performance of a cryogenic system, the radiometer in this experiment switches between fields of view using a rotating chopper wheel. The antenna, pointed towards the chopper at an angle of 45 degrees from vertical, alternately accepts reflected and transmitted radiation from two locations 90 degrees apart in the sky. A block diagram of this particular radiometer is given in Figure 2.4.

2.2.1.1 Cryogenic Temperature Components

Horn and Coupler: Power passes into the cryogenic dewar[1] through a 5-mil thick mylar window and is collected by a corrugated conical horn cooled to 77 K. The antenna half-power beam width is 7 degrees, and the gain pattern for an equivalent horn scaled to 33 GHz and measured at 31.4 GHz (Janssen *et al.*, 1979) is shown in Figure 2.5. Beam patterns of a 90 GHz horn identical to the one used in this experiment have been measured and are essentially the same as those shown in Figure 2.5 (C. Witebsky, private communication). A circular-to-linear polarization transition and a 5.4 cm copper-plated section of thin-wall stainless steel waveguide

[1]Specific components used in the radiometer are itemized in Appendix F.

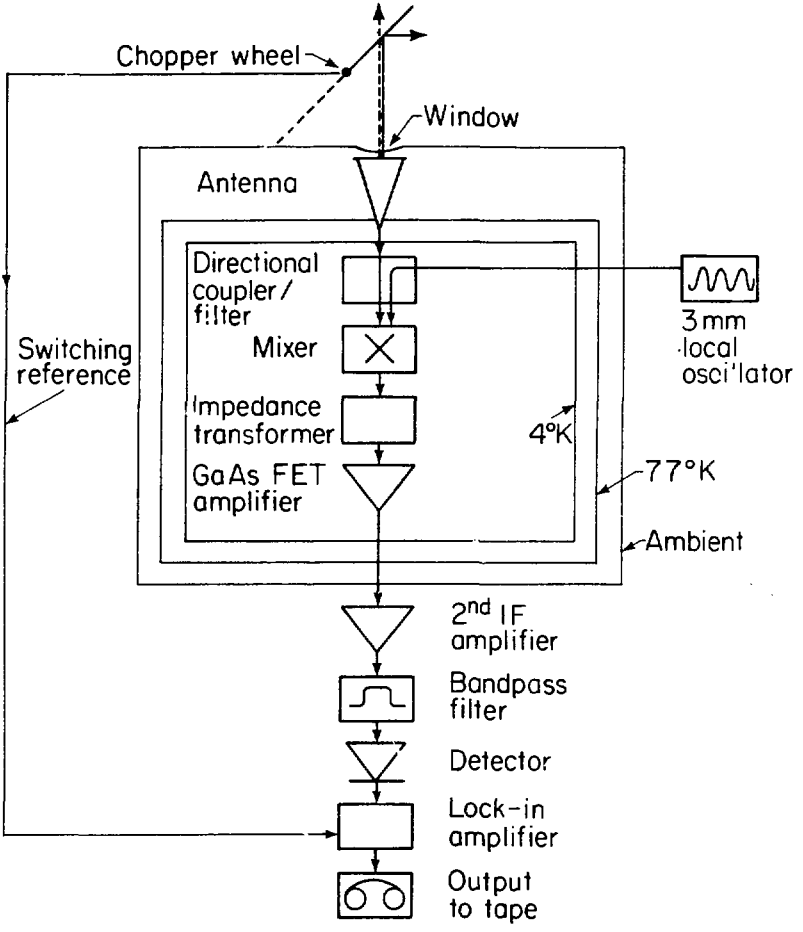

Figure 2.4. Block diagram of the 90 GHz anisotropy experiment.

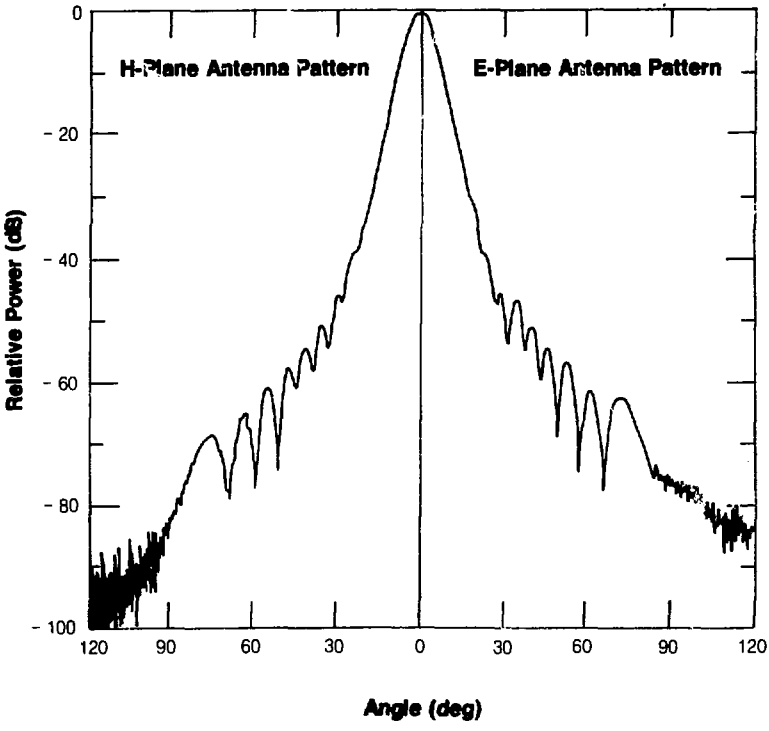

Figure 2.5. Antenna beam patterns. Data shown are for a proportionally scaled horn at 31.4 GHz (Janssen *et al.*, 1979); the 90 GHz beam patterns are essentially identical.

connect the horn to the components on the 4 K cold plate. Loss in the window and in the signal waveguide is less than 0.3 db.

The signal and the 90 GHz local oscillator (LO) power fed separately into the dewar enter two ports of a tunable resonant ring diplexer (Davis, 1977). The mixer block is mounted on the third port and the fourth port is terminated. Insertion loss of the coupler for the signal is 0.3 db at room temperature; local oscillator-to-mixer loss in the coupler when the coupler is tuned for maximum LO throughput is 4 db for the LO carrier and 23 db for non-resonant LO sideband noise.

Mixer: From the coupler, LO and signal power pass through a step-reduced-height waveguide transformer to a low-doped Schottky barrier diode. Noise theory of Schottky barrier mixers is discussed in Barber (1967). Weinreb and Kerr (1973) analyze cryogenically-cooled centimeter and millimeter mixers; the mixer used in this experiment is an updated version of the one described by Kerr (1975) and Cong, Kerr, and Mattauch (1979). The GaAs mixer diode is operated with a DC bias current of 780 μamp. It is mounted on a quartz microstrip and protrudes into the quarter-height WR-10 waveguide. A phosphor-bronze whisker extending across the waveguide contacts the metal surface of the Schottky barrier. Intermediate frequency (IF) power passes from the diode through a microstrip radio frequency choke and of the mixer block.

Behind the chip, an adjustable backshort tunes away the reactive component of the impedance seen by the junction. The tuning vernier on the ring coupler and the backshort are not accessible when the system is cooled. They were adjusted when the system was warm to maximize LO power coupled into the diode, as indicated by the change in diode voltage at constant bias current when the LO was turned on. When the system is cooled, the bias voltage is not as strongly affected by the LO.

IF Amplifier: A low-noise IF amplifier immediately following the mixer is essential to utilize the cooled mixer's low noise figure. The noise contributed by components downstream of the

first IF amplifier is reduced by a factor equal to the first IF's gain and is therefore not significant. This receiver uses a cryogenically-cooled two-stage GaAs FET amplifier described by Williams and Lum (1980) and built in the University of California's Radio Astronomy Laboratory. The amplifier is optimized for performance at L-band frequencies between one and two GHz. The actual IF bandwidth of 1080 to 1670 MHz was established by evaluating the receiver spot noise figure and gain as a function of frequency and maximizing the overall sensitivity. At 77 K, the amplifier has a noise temperature of 20 K and a gain of 25 db over an effective gain-weighted bandwidth of 540 MHz. Its output is attenuated 3 db by the low thermal conductivity stainless-steel rigid coaxial cable through which power leaves the dewar cold-space.

The amplifier functions best when viewing a source impedance of 50 to 70 ohms (Williams and Lum, 1980), whereas the incremental impedance of the biased mixer diode when cooled is closer to 200 ohms (Cong, Kerr, and Mattauch, 1979). Therefore, a broadband, partially tunable impedance transformer is used to match the two. While connected to the mixer, the transformer was trimmed to minimize VSWR over the IF amplifier operating band. The transformer also provides a terminal for feeding DC bias to the mixer.

2.2.1.2 Non-Cryogenic Temperature Components

Local Oscillator: A Gunn diode followed by a waveguide attenuator produces 6 mw of 90 GHz LO power which is further attenuated 10 db by passage through a mylar window, an unplated stainless-steel waveguide inside the dewar, and the ring coupler. Somewhat less than one milliwatt is delivered to the mixer. The LO power was adjusted to maximize radiometer sensitivity, which is only weakly dependent on the LO power level.

Second IF amplifier, Filters, and Detector: Outside the dewar, the radiometer signal passes through an isolator (which was later removed: see Chapter 3) and is amplified another 50 db by the second IF amplifier. The 180 K noise temperature of this amplifier adds less than 2 K to the

system noise, since its contribution is reduced by a factor equal to the first IF amplifier's gain. The IF passband is determined by an eight-pole bandpass filter following the second IF amplifier. The signal then passes through a notch filter at the balloon telemetry transmitter frequency of 1485.5 MHz (see Chapter 3) and is attenuated to keep the Schottky barrier detector diode in its linear range. After detection, the signal is fed to a lockin amplifier.

Beam Chopper and Lockin Reference: The beam is switched between sky patches with a polished aluminum rotating chopper wheel. The chopper emissivity into the mode accepted by the radiometer (linear polarization with H field vertical) can be calculated by considering the corresponding case of radiation incident on a conductor at 45 degrees with H field in the plane of incidence. The fractional power absorbed is given by

$$\epsilon = \frac{2\delta \cos 45^\circ}{\lambda}$$

with δ the skin depth and λ the free space wavelength over 2π. Upon substituting typical values for aluminum, ϵ equals 6×10^{-4} at 90 GHz. Fractional absorption is equal to emissivity, so this value predicts emission on the order of 135 mK from an aluminum chopper at 225 K. Emissivity increases as the square root of resistivity, so a warmer chopper has a higher emissivity as well as a higher physical temperature.

The chopper wheel, having low emissivity and surrounded by turbulent air, is assumed to be at the ambient air temperature. However, the ambient temperature is difficult to measure since the residual air at altitude does not make good thermal contact with sensors. The blackbody pop-up calibrator target, whose temperature ranged between 205 and 225 K during two different flights, most likely radiatively cooled below the ambient air temperature. The 225 K air temperature used in the emissivity calculation is that given in the U.S. Standard Atmosphere (Cole *et al.*, 1965; reprinted by Ulaby *et al.*, 1981) for ambient temperature between 28 and 30 km. The actual offset observed during flight is about 200 mK; the discrepancy can be attributed

to the large uncertainty in the conductivity of aluminum alloys depending on composition and preparation and to the uncertainty in chopper wheel temperature.

The chopper is a two-lobed wheel driven at 700 RPM and phase-locked to a crystal-controlled oscillator. The beam switching frequency is $23\frac{2}{3}$ Hz. When the chopper is phase-locked, the oscillator provides the $23\frac{2}{3}$ Hz reference signal to the lockin and also establishes the integration period of 50 switch-cycles (just over two seconds). The motor and clock circuits are electrically isolated from the rest of the apparatus.

Lockin Amplifier and Data Logger: The first stage of the synchronous-filter lockin amplifies the detector output. The amplified signal is used to charge one capacitor when the radiometer observes the direct beam and another when it observes the reflected beam. A differential amplifier produces an output voltage proportional to the difference between capacitor voltages. During the 20% of each switch cycle when the edge of the chopper crosses the horn, the lockin input signal is blanked to eliminate spurious diffracted signals. As a result, one second of observation time corresponds to a net integration time of 0.8 second. The lockin output is "boxcar-integrated" for a period of 2.11 seconds, digitized, and recorded by an onboard tape logger.

2.2.2 Support Equipment

2.2.2.1 Magnetometers

To reconstruct the positions of the direct and reflected beams, the radiometer's orientation is first determined relative to the earth's magnetic field. Two sets of magnetometers are included in the experiment. The primary system is a three-axis fluxgate unit; three orthogonally-mounted Hall probes provides a backup system.

2.2.2.2 In-Flight Calibrator

To determine the stability of the radiometer calibration in flight, a small blackbody target made of iron-loaded epoxy was periodically raised into the beam. The target subtends about 1% of the beam solid angle and contributes an antenna temperature on the order of 1% of its physical temperature. At altitude, the calibrator showed that the system gain is stable to better than $\pm 1\%$ over a flight. Calibration is discussed further in Appendix C.

2.2.2.3 Power

The system requires thirty watts of power with up to thirty more watts going to heaters in the temperature regulators. This power was supplied by five pounds of lithium batteries on the radiometer's first flight, when weight was particularly critical, and by 100 pounds of rechargeable lead-acid gelled electrolyte cells on subsequent flights. All power supply voltages were regulated by non-switching series-pass DC regulators.

2.2.2.4 Temperature Regulation

Cryogenic temperature stability is maintained independent of altitude and ambient pressure by venting the liquid helium and liquid nitrogen tanks through absolute-pressure regulators. Temperatures inside the dewar are monitored at three locations with silicon diodes. One sensor on the horn measures the temperature of the liquid-nitrogen-cooled shield, and two on the 4 K cold plate measure the GaAs FET IF amplifier and the mixer block temperatures, respectively.

Temperatures of the non-cryogenic electronics were regulated with proportional heaters. Integrated circuit sensors on the chopper motor, the LO, the second IF amplifier, the support

electronics cage, the dewar exterior, and the in-flight calibrator were used to measure and record these temperatures; the heater currents were also recorded.

2.3 System Configuration

2.3.1 Experiment and Gondola

The radiometer has flown four times in four different configurations. The radiometer dewar, chopper wheel, and motor remained unchanged for the four flights and are shown in profile in Figure 2.6.

The dewar is tilted back with the horn viewing the chopper at a 45 degree angle. In this position, the dewar could hold about two liters each of liquid nitrogen and liquid helium, sufficient to keep the system cold for at least 18 hours. Surrounding the aperture for the horn is a hexagonal groundshield, shown in cross-section in Figure 2.6, which was designed to keep ground radiation from contributing more than 0.1 mK. This groundshield is supplemented by shielding on the gondola. The chopper is enclosed, except where it crosses the horn, by an electrically-conductive guard (not shown in Figure 2.6) which minimizes modulation of any stray radio power and prevents the loss of significant digits (i.e. the author's).

The electronics not mounted in or on the dewar, and the flight batteries, are carried separately on the balloon gondola. Also on board is the telemetry and telecommand system linking the experiment to the balloon launching facility. The entire gondola is suspended under a motor and bearing which rotates the package. A perspective view of the gondola as flown in April 1982 is shown in Figure 2.7.

2.3.2 Balloon and Flight Train

The required size of a scientific balloon depends on the weight of the apparatus and

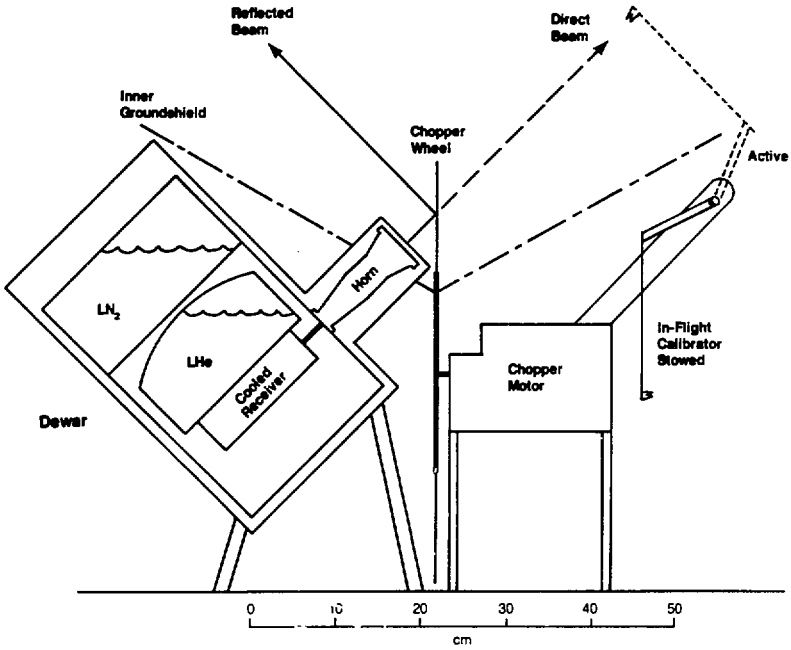

Figure 2.6. Radiometer profile.

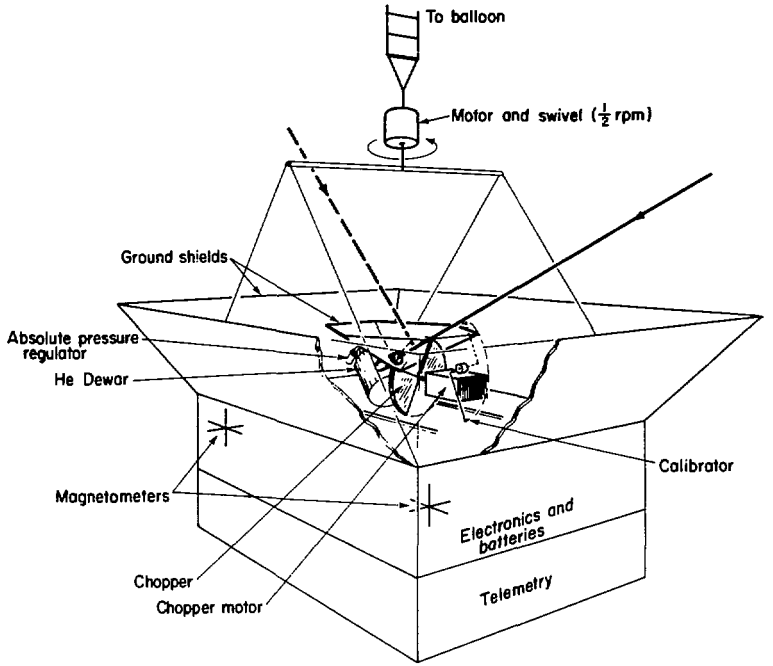

Figure 2.7. Perspective view of gondola in April 1982 configuration. Gondola dimensions are 0.8 × 0.9 × 1.7 m.

the desired altitude. With its various configurations and hosts, this experiment has flown with balloons ranging from six hundred thousand to six million cubic feet in volume. Hanging under the balloon, and connected to it by a termination fitting which is separated at the end of the flight, is the parachute. The rotor and gondola are attached to the parachute at the end of a wire cable ladder long enough to keep the balloon 30 degrees away from the radiometer beams. Figure 2.8 shows the balloon and flight train.

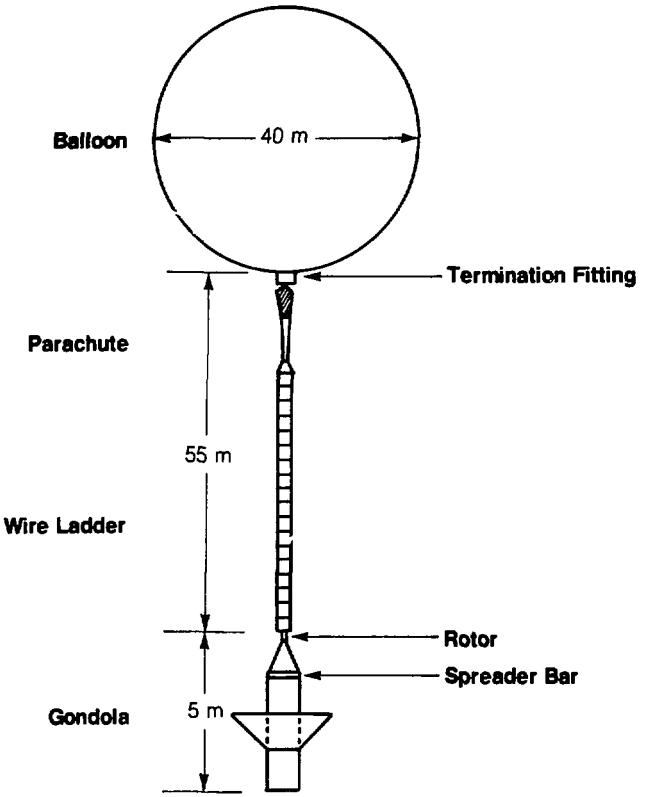

Figure 2.8. Balloon and flight train for April 1982 flight. Not to scale.

Chapter 3

System Operation

3.1 Radiometer Performance

3.1.1 Noise Temperature

The noise temperature of the radiometer at ambient temperature, in wideband measurements over the full 540 MHz IF bandwidth, is 650 K. At liquid nitrogen temperature, the noise temperature drops to 220 K, and at its normal operating temperature of 4 K the radiometer system temperature is 135 K. Over the IF bandwidth, this yields a system sensitivity of 12 mK for one second net integration time.

3.1.2 Calibration

The radiometer is calibrated by placing an ambient temperature blackbody emitter in one beam and a blackbody target saturated with liquid nitrogen in the other. The calibration constant (Kelvins antenna temperature per volt) changes by a factor of two between operation at 300 K and at 4 K. At 4 K, the system is quite stable, with the RMS scatter in widely separated calibrations throughout a year of 2%. Relative calibrations of the system during a flight are

provided by inserting a small blackbody into one of the radiometer beams every 27 minutes. The calibration sequences last 43 seconds, causing a 3% loss of potential observation time. Further details of system calibration and corrections are presented in Appendix C.

3.1.3 Operating Parameters

Several factors determine the operating parameters of this apparatus. The chopping frequency of $23\frac{2}{3}$ Hz is high enough to be in the region where thermal fluctuations with a flat spectrum dominate over fluctuations having the $1/f$ spectrum typical of gain variations. These drifts and gain fluctuations limit the gondola rotation period, which must be short enough so that the drifts are small compared to the minimum detectable signal over the same interval. At the same time, to preserve sensitivity to small-scale structure, the antenna field of view should not be unnecessarily broadened by gondola rotation. The boxcar integrator averages over 50 chopper cycles (2.11 sec) during which each beam scans an azimuthal range of 13 degrees at a rotation rate of 1 RPM. For one minute observation time, the radiometer sensitivity is 1.7 mK.

3.1.4 System Testing

In the laboratory, we investigated possible sources of systematic error by observing a stable load with the radiometer, modulating some parameter, and looking for a synchronous modulation in the radiometer output. However, testing to the 0.1 mK level on the ground is not feasible. Eleven hours of integration are necessary to reach that sensitivity with a 77 K target and over forty-five for an ambient temperature load. Instead, useful tests involved modulating some parameter (e.g. magnetic field) at a higher level than was expected in flight. The limit on the instrument's response was then scaled assuming a linear stimulus/response relation.

3.1.4.1 Magnetic Dependence

Since the radiometer rotates in the earth's magnetic field, any magnetic dependence of the output will yield a signal synchronous with gondola rotation and therefore will mimic background radiation anisotropy. With the isolator removed, there are no magnetically sensitive elements in the radiometer and no magnetic dependence was expected. Magnetic sensitivity was bounded by measuring a response of 0.4 ± 1.9 mK to a switched 10 gauss field. This puts a 0.1 mK limit to the effects of the 0.5 gauss peak-to-peak modulation of the horizontal component of the earth's magnetic field caused by gondola rotation.

3.1.4.2 Radio Interference and Other Tests

Sensitivity to radio interference was tested, particularly after data from first flight was severely affected by it, by transmitting near the apparatus. Sources of radio frequency (RF) leakage were located and shielded by adding filters or enclosing components within RF-tight shields. To insure proper system operation under conditions expected at altitude, the system was placed in a thermal/vacuum chamber which was evacuated and cooled. This provided a "zeroth order" test of system operation. However, all the problems of doing sensitive tests on the ground were exacerbated by inability to access the system or to calibrate while the chamber was evacuated.

3.2 Data Collection

3.2.1 Flight Scheduling

The sun is a 6000 K source which, when diluted in the radiometer field of view, must still be attenuated 50 db to contribute less than 0.1 mK. To achieve this rejection, it must be more than 35 degrees off the beam axis. Sunlight might also cause temperature cycling synchronous

with the gondola rotation. As a result, the radiometer collects useful data primarily at night. If coverage of a particular portion of the sky is important, flights can be scheduled only for that part of the year when the desired section is visible at night.

The moon can contribute a signal of up to 800 mK depending on lunar phase and position relative to the beam. To keep its effect under 0.1 mK, it must be more than 25 degrees off the beam axis. Depending on the moon's elevation, a significant amount of observation time will be lost in satisfying this requirement. On the other hand, the moon's signal is a valuable check on the radiometer pointing and can in principle provide an absolute calibration. In practice, inaccuracy in determining its position relative to the radiometer beam and the corresponding uncertainty in antenna gain prevented using the moon as an absolute calibrator.

There are two flight opportunities on either side of new moon, each of two or three days length, where the moon will be visible for a short period of time at the beginning or end of a flight. The determining factor in flight scheduling, though, invariably becomes the weather. Given the requirements on high-altitude wind speed and direction (particularly relative to the nearest large body of water), surface conditions at launch, and expected weather in the down-range recovery area, one rarely has the luxury of waiting for ideal celestial alignments.

3.2.2 July 1981 Flight

The 90 GHz radiometer was originally designed to fly in a gondola operated by David Wilkinson's group at Princeton University. This gondola, used to make the measurements reported in Cheng *et al.* (1979) and Boughn *et al.* (1981), had carried radiometers operating at 24.8, 31.4, and 46 GHz. The Berkeley radiometer replaced the 24.8 GHz Princeton radiometer. The gondola rotated at a rate of 1 RPM, and the Princeton magnetometers provided orientation information for both Princeton and Berkeley experiments.

Although presenting some of the inevitable difficulties of collaborating with another group, this gondola-sharing arrangement made my introduction to ballooning much easier. We at Berkeley were responsible for the 90 GHz radiometer; the balloon, gondola, and flight procedures were for the most part handled by the Princetonians.

In June, 1981, we packed the radiometer and all of our test and support equipment into the back of a station wagon and drove to the National Scientific Balloon Facility in Palestine, Texas. We tested our equipment in the NSBF thermal/vacuum chamber mentioned previously, mounted the radiometer on the gondola, fed the Princeton magnetometer signals into our in-flight recorder, and arranged for our radiometer output to be telemetered to the ground. We then checked for interference between the Berkeley experiment, the Princeton radiometers, and the NSBF-supplied command and telemetry equipment.

This last test revealed a significant problem. The telemetry downlink transmitter at 1.485 GHz fell in the middle of the 90 GHz radiometer's IF band and severely interfered with the radiometer's operation. Deploying the transmitting antenna on a long cable under the gondola, and adding more shielding, did not reduce the interference to acceptable levels. In addition to transmitting the Princeton data, the transmitter was required by the NSBF to command and locate the balloon and could not be turned off.

On July 1, weather conditions and the moon position were acceptable for launch. Taking advantage of the lull in surface winds at sunset, the balloon was launched at 19:13 Central Daylight Time (00:13 Univeral Time on July 2) and rose to float altitude of 25 km (25.1 millibar pressure) in 80 minutes. RF (or more precisely IF) interference was evident in the 90 GHz radiometer data which was being telemetered to the ground. The in-flight calibrator also failed to operate during the first half of the flight, due (it was discovered later) to an overheated relay.

The gondola drifted almost due west at about 40 knots during the night. As it neared mountainous terrain in west Texas the next morning, the flight was terminated, introducing

some further problems. When the parachute opened, the spreader bar separating the gondola suspension cables from each other snapped. Possibly as a result, the package flipped over on its back upon landing. The radiometer was checked out after the experiment was recovered and returned to the balloon base. Except for the chopper motor, which had burned out when the chopper wheel jammed on impact, the radiometer functioned normally.

3.2.3 November 1981 Flight

3.2.3.1 Modifications

Based on the experience gained from the July flight, several modifications were made to the apparatus. Most importantly, a notch filter providing over 70 db rejection at the telemetry transmitter frequency of 1485.5 MHz was placed immediately before the detector diode. The isolator between the first and second IF amplifiers, which had been one of the most RF-sensitive components and whose presence was not essential to system operation, was removed. The second IF amplifier, bandpass filter, notch filter, and detector diode were moved into an RF-tight enclosure mounted directly on the dewar. All lines to this enclosure, as well as those going directly to the dewar, entered through filters.

The radiometer found a new host with Rainer Weiss from MIT, who was planning flights from Palestine in the fall. His four-channel, far-infrared bolometer system was to fly then in two configurations: with wide-beam (seven-degree FWHM) horns for a large-scale anisotropy experiment, and with two-degree beams to search for far-infrared sources. The MIT gondola required some additional modifications to be made to the 90 GHz experiment. Although primary magnetometer signals were obtained from the MIT experiment, a backup set of three orthogonal Hall probe magnetometers was also flown. The lithium batteries powering the system for the July flight were replaced by gelled-electrolyte lead-acid cells to permit system testing in the

flight configuration. Although much lighter, the lithium batteries were not rechargable and could not be used to power the system during ground tests. Other changes included surrounding the window over the antenna with a perforated collar through which nitrogen gas was exhausted to prevent frost formation on the window. These modifications were all done in Berkeley; the problems of mounting the experiment onto the MIT gondola and interfacing with MIT and with NSBF were left as field exercises.

In early October, 1981, the radiometer and associated equipment were once again packed into a station wagon for the three-day drive to Palestine. On arrival, the equipment was checked out and a structure for mounting it onto the MIT gondola was developed and built. The Berkeley equipment was placed above the MIT apparatus on two platforms projecting out the sides not occupied by MIT optics. The end result was a package 3 m high and extremely top-heavy. The hexagonal groundshield surrounding the 90 GHz radiometer was extended on each face by adding foil-covered styrofoam panels. After waiting a month for weather, flights of other groups, and the completion of the the first MIT flight (which was done with the same gondola), the 90 GHz anisotropy experiment was ready to fly.

3.2.3.2 Flight

At sunset on November 4, 1981 (23:42 UT), the gondola was launched with a 6 million cubic foot balloon. The length of the parachute and flight train of 120 m gave the balloon an angular radius of 14 degrees at altitude when viewed from the gondola suspended underneath. Gondola rotation with a 74-second period was started fifteen minutes after launch. At this rate, each beam swept through 10.3 degrees in azimuth per 2.11-second integration period. The balloon rose more slowly than expected and never reached the 35 km altitude required by the MIT infrared experiment. It did reach 27.5 km (17.1 mbar pressure) two hours after launch and peaked at 30 km (11.8 mbar) another half-hour later. Slowly dropping for the remainder of the

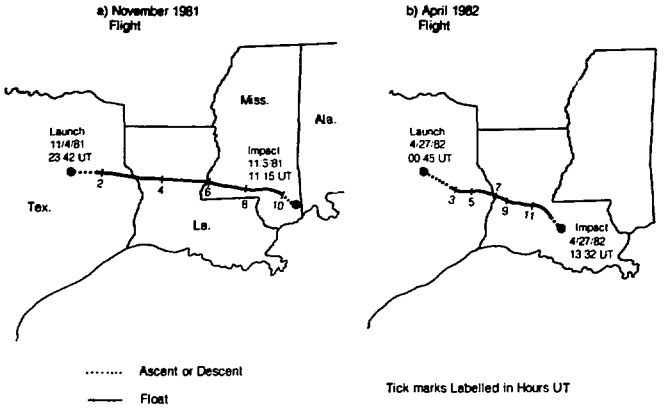

Figure 3.1. November 1981 and April 1982 flight paths.

flight, the balloon crossed 27.5 km again six hours after the peak altitude was reached. Two hours after that, the flight was terminated from an altitude of 26 km as the gondola neared the Gulf of Mexico, and the package landed in a wooded area near Mobile, Alabama. The flight path is shown in Figure 3.1a.

The Berkeley experiment worked well throughout the flight. As the gondola reached float altitude, the moon reached its maximum elevation of 39 degrees, six degrees off the beam. Because of contamination by the moon, one-quarter of the data taken in the first two hours at float had to be dropped from later analysis. On the ground, passing the telemetered lockin

amplifier output through a 55-second time constant RC filter clearly showed the 3 mK dipole anisotropy in real time as a modulation synchronous with the gondola rotation. Figure 3.2 shows an equivalent plot from the April 1982 flight.

Analysis of the twenty in-flight calibrations showed that the gain at altitude varied by less than $\pm 0.7\%$ (1 standard deviation). There were some periods of highly irregular rotation during the flight, probably arising from shear winds acting on the asymmetric surface and mass distribution of the gondola.

No damage was incurred on landing, and the system was tested upon its return to Palestine. At ambient temperature (with no cryogens), the system gain was within one percent of its ambient temperature pre-flight value. When the system was re-cooled following recovery, but had not yet reached equilibrium, the gain was within five percent of the pre-flight cooled value.

3.2.4 April 1982 Flight

The November flight provided good data covering half the northern sky. Filling in the other half would increase the value of the data by much more than just the additional observation time, since complete coverage decouples otherwise highly correlated dipole and quadrupole parameters.

3.2.4.1 Modifications

To get this additional coverage, we made plans to fly again in April. The radiometer remained basically unchanged. What needed to be added was the equipment which had previously been supplied by our hosts — primary magnetometers, a gondola, and a balloon. A multi-axis fluxgate magnetometer provided the primary x and y reference, with the Hall probe mag-

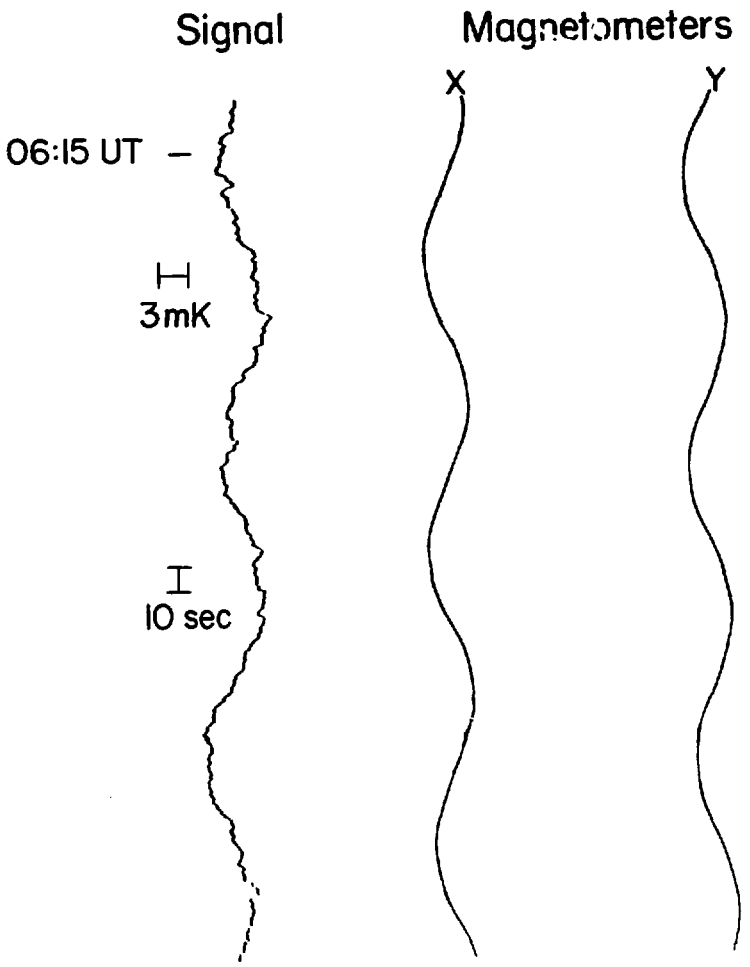

Figure 3.2. Real-time dipole signal.

netometers retained as a backup unit. A gondola, 0.8 x 0.9 x 1.7 m in size, was constructed and surrounded by an external aluminum sheet groundshield extending up to the height of the internal hexagonal shield. The gondola carried the radiometer, electronics, and batteries, and provided room for the NSBF telemetry package. Analysis of the radiometer's performance during the November flight showed that the gondola could be rotated more slowly, so the rotation was slowed down to a 110 second period for the April flight. At this rate, the radiometer beams swept through one beam-width (7.0 degrees) in one boxcar integration period.

3.2.4.2 Flight

Having obtained two balloons and authorization for flight, we packed the equipment (no longer fitting in a station wagon) into a van and took the by-now-familiar route to Palestine. After checking out the equipment, rigging the gondola, and connecting our telemetry and telecommand lines to the NSBF telemetry package, we were ready to fly four days after arrival. With a small (one million cubic foot) balloon, our flight was not as restricted by launch surface weather conditions as those using larger balloons. The high altitude wind and downrange weather requirements, though, still had to be satisfied.

On April 26, the 350 pound gondola was launched at sunset at 19:45 Central Daylight Time (00:45 UT on April 27). The gondola hung 55 m below the balloon, which had an angular radius of 16 degrees at altitude. The rotor was turned on just after launch. The gondola reached its maximum altitude of 28.5 km (14.6 mbar pressure) two hours after launch; it dropped very slowly after that but remained above 27.5 km (17.1 mbar) for the duration of the flight. The moon, setting as the instrument rose, was within 25 degrees of the beam for less than one-half hour after the balloon reached float altitude and did not contribute a signal strong enough to see above the radiometer noise.

Gondola rotation was more uniform than it had been in November, and the CBR dipole

anisotropy was again observable in real-time in the downlinked radiometer output (Figure 3.2). The pop-up calibrator rose every 27 minutes, as expected. However, the calibration signals were extremely erratic, varying by much more than would be consistent with the stability of the radiometer offset. Examination of the calibrator after recovery showed that the arm was severely bent, presumably having been caught just after launch by some of the tape fastening thermal insulation to the chopper motor assembly and causing it to rise to irregular positions during the flight.

The gondola drifted east during the night, taking a southward turn eleven hours into the flight near sunrise. Wanting to keep the gondola out of the Gulf of Mexico even more than we wanted to check our pointing with the sun, we terminated the flight just after sunrise near Baton Rouge, LA. The April ground track is shown in Figure 3.1b; sky coverage obtained from both November and April flights is shown in Figure 3.3.

After the apparatus had been recovered and returned, it was cooled and tested. Post-flight calibration was within 3% of the pre-flight value. Eight days after arrival, we were on the road back to Berkeley.

3.2.5 November 1982 Flight

With two successful Texas flights providing coverage of most of the northern sky, southern sky observations became extremely attractive. In addition to decoupling the axisymmetric dipole and quadrupole terms which cannot be separated in data taken from a single declination (see Chapter 5), southern hemisphere measurements permit observations of the galactic center. Dust emission should be maximized there, making possible either its measurement or the establishment of a firm upper limit to the galactic dust contribution. Additional motivations for further flights were the increased observation time and the chance to modify and re-fly the in-flight calibrator.

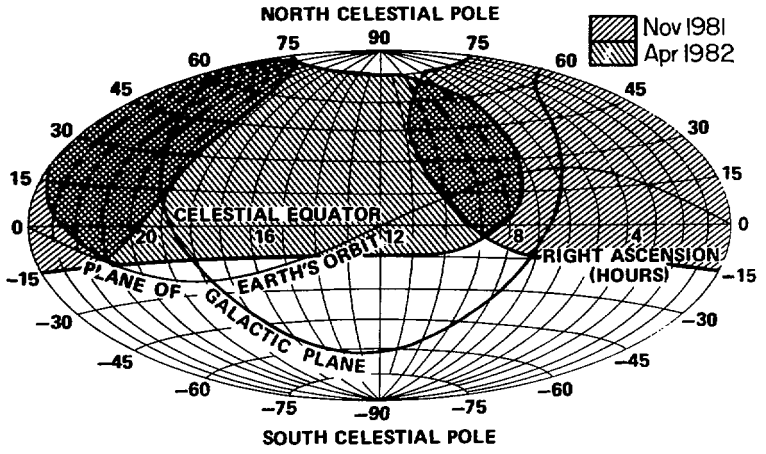

Figure 3.9. Northern sky coverage. Hammer-Aitoff equal area projection.

3.2.5.1 Modifications

The existing in-flight calibrator observations placed limits on gain variations during a flight. More useful would be a full-beam calibrator which could provide an absolute calibration of the radiometer at altitude to relate the radiometer's ground performance to its flight operation.

A blackbody target 10 cm by 10 cm in area with a front surface of cones 2.5 cm high was constructed at NASA's Goddard Space Flight Center out of iron-loaded epoxy. The target surface, including the valleys between the cones, was covered with styrofoam to keep the emitting surface at a stable temperature. Reflection off the target's front surface, minimized by the shape of the cones and by the high absorption of the epoxy, was suppressed by more than 24.5 db. The target was incorporated into a new calibrator arm and the lockin amplifier circuitry was modified to automatically reduce system gain by a factor of 100 when the target was inserted into one beam.

At the same time, we had been making arrangements with the Brazilian Institute for Space Research (Instituto de Pesquisas Espacias — INPE) to use their ballooning facilities. We modified the gondola slightly to accept the Brazilian telemetry system, and in late October, 1982, we air-freighted the equipment, two balloons, and 500 liters of liquid helium to INPE headquarters near Saõ Paulo, Brazil.

3.2.5.2 Flight

We ourselves arrived in early November to find our equipment and the helium (a significant addition to that nation's supply) in good shape. After a week's preparation and coordination, we moved to the launch facility at Cachoeira Paulista (latitude 23° South) 100 km away where the INPE flight crew rigged the gondola and flight train and prepared for launch. Three launch attempts were scrubbed over the next several days due to weather conditions or

telemetry problems, but at 17:14 local time (20:14 UT) on November 20, 1982, the gondola was launched. The 1.75 million cubic-foot balloon reached float altitude of 30.5 km two hours later.

Observed on the ground, the limited number of signals which the INPE telemetry could downlink indicated that the instrument was performing quite well. The moon, which passed through the center of the radiometer beams due to the later-than-desired launch date, was highly visible in data at the beginning of the flight, and the dipole anisotropy was clearly evident in real-time throughout the night. The balloon's altitude at float remained between 30 and 31 km. Fourteen hours after launch, the sun rose into the radiometer beams. After observing it for a few rotations to check the magnetometer alignment, we powered down the radiometer and gave the command to release the gondola from the balloon. Nothing happened. A long hour later, it became clear that despite four explosive bolts with redundant command circuits and power supplies, the termination fitting remained connected. The balloon and gondola stayed aloft that day, losing altitude and finally drifting out of telemetry range the following night.

Aerial searches for the signal from the on-board radio beacon were hampered by bad weather and by poor position fixes for the balloon's last known locations. The searches did not locate the gondola during the beacon's three-day lifetime. Subsequent searches and reward offers (Figure 3.4) were also unproductive, and the gondola has not been recovered.

3.2.5.3 Post Mortem

The down-linked analog telemetry data, intended for real-time monitoring (or worry) but not for data analysis, is of questionable quality. The onboard voltage-controlled-oscillators apparently drifted considerably, and much telemetery was contaminated with dropouts and interference. Nevertheless, downlinked data was recorded on the ground and has since been digitized. Some useful engineering data has been obtained from the Brazil flight, including limits

R E C O M P E N S A

Cr$450.000,00 (QUATROCENTOS E CINCOENTA MIL CRUZEIROS)

PARA INFORMAÇÕES QUE LEVEM À RECUPERAÇÃO DE UMA CARGA CIENTÍFICA EM BALÃO.

A CARGA, UMA CAIXA DE METAL DE APROXIMADAMENTE 1M x 2M x 1M, DEVE TER CAIDO APROXIMADAMENTE EM 26 DE NOVEMBRO DE 1982 NA REGIÃO PRÓXIMA DE CORNÉLIO PROCÓPIO, MOSTRADA NO MAPA EM ANEXO.

JUNTO COM A EXPERIÊNCIA DEVE ESTAR UM PÁRAQUEDAS COR LARANJA BRILHANTE E PODE SER VISTO DO AR.

PEDAÇOS DO BALÃO, DE PLÁSTICO BRANCO, DEVEM ESTAR POR PERTO.

PARA MAIORES INFORMAÇÕES LIGUE, À COBRAR PARA:

DR I M MARTIN
INSTITUTO DE PESQUISAS ESPACIAIS - INPE
CAIXA POSTAL 515 - 12.200 S J DOS CAMPOS - SP
TELEFONE: (0123) 22-9977
À QUALQUER HORA DO DIA OU NOITE

Figure 3.4. Reward notice for gondola.

on pointing accuracy. The reward for information leading to recovery of the onboard data cassette is still outstanding.

Chapter 4

Data Reduction and Processing

4.1 Data Format

The boxcar-integrated radiometer output and the horizontal magnetometer values were recorded on the on-board tape cassette every 2.1 seconds. Every 6.3 seconds, the Hall probe magnetometer values were written, and sixteen housekeeping signals were recorded once in every 25 second (12 integrator output) record along with Universal Time and some digital status bits. Gondola altitude and position, determined by a pressure transducer and an on-board OMEGA navigation receiver, were recovered after the flight from the downlinked telemetry data.

In Berkeley, the data on the flight cassette was read and transferred to disk. Absolute calibrations done before flight and recorded by hand were cross-checked with the values written on pre-flight and post-flight tapes. For the November flight, in-flight calibrations done every 27 minutes (64 records) were tabulated and removed from the data. For the April flight, since the in-flight calibrator was damaged soon after launch, observations were removed from the data but could not be used for relative calibration.

4.2 Beam Positional Reconstruction

The gondola position and orientation, obtained from magnetometer and tracking data, uniquely determine the position of each beam on the sky. The fluxgate x-y magnetometer values, recorded just after each boxcar-integrated radiometer value, were interpolated to times corresponding to the midpoint of the integration period. The midpoint and amplitude of the magnetometer signals were found from twenty-two minute running averages of the magnetometer extrema. Removing the DC level from the magnetometer signals and normalizing their amplitudes yielded the sine and cosine of the gondola azimuth angle with respect to the horizontal component of the earth's magnetic field. Correcting the magnetic azimuth by the deviation between magnetic and true north, obtained from National Oceanic and Atmospheric Administration sectional navigation maps, yielded the true azimuth angle.

Observations of the moon at the beginning of the November flight showed that the beam azimuth angles were within 1.5 degrees of the values determined by the above process. Although data recovered from telemetry from the Brazil flight was not put through an identical analysis, observations of the sun at the end of the flight showed the deviation between magnetometer-derived azimuth and true azimuth to be 0.2 ± 0.8 degree for the direct beam and 0.9 ± 0.8 degree for the reflected beam.

Gondola latitude and longitude were determined by the onboard OMEGA receiver and logged on the ground every five minutes. Comparison of the OMEGA positions with the launch and impact locations and with FAA radar fixes showed that the OMEGA positions were accurate in April and at the beginning of the November flight but gave a position 0.6 degree too far east and 0.5 degree too far north for the November impact point. The November positions were corrected for this offset by assuming the error in position was proportional to the distance from Palestine.

For both Texas data flights, the gondola drifted almost due east at a fairly uniform rate. For data analysis, a linear ground track with constant speed was assumed. This approximation was at all times within 0.5 degree of the OMEGA position (corrected, in the November case, for the position offset). The gondola location and azimuth were then used to reconstruct the sky position of each beam.

4.3 Data Editing and Sky Coverage

Data taken during calibration sequences, along with data taken when either radiometer beam pointed within 25 degrees of the moon, was removed. For the November flight, the moon cuts eliminated 25% of the first 2.3 hours at float or 6% of the total November data. Less than 0.2% of the April data was removed due to the moon. An additional twenty-minute section of data two-thirds of the way through the April flight, during which the offset changed by four mK and then returned to its previous value, was deleted. During that section, the RMS difference between consecutive 25-second data averages was more than twice the RMS difference between consecutive 25-second averages for the rest of the data. The RMS difference between consecutive 2.11-second integrator values in that section is not noticeably higher than in other sections, indicating that the excess noise in the deleted section is at longer time scales than 4 seconds. No other section of data showed similar behavior. Removing the section had negligible effect (less than 15% of the one-standard-deviation statistical error) on spherical harmonic coefficients fitted to the data. No additional non-statistical fluctuations were seen, and after the moon cuts, none of the 29000 radiometer 2.11-second boxcar integrator values differed from a local mean by more than 4.5 standard deviations.

Figure 4.1 shows the density of sky coverage of all data remaining after the moon cuts and the twenty-minute cut described above. Of the data remaining after the moon cuts, 17% of the November data and 10% of the April data had one of the radiometer beams within 5 degrees

of the galactic plane. These data, 13% of the total, were excluded from some of the spherical harmonic fits discussed in the following chapter. The galactic plane is indicated by Figure 5.3 in the next chapter, which is done to the same scale as Figure 4.1.

4.4 Offset Analysis and Removal

As stated previously, the chopper wheel introduced an offset between direct and reflected beams of the radiometer. This offset had an average magnitude of 201 mK in the November flight and 225 mK in April, implying emissivities of 8.9×10^{-4} and 1.0×10^{-3} for a chopper temperature of 225 K. The offset varied by no more $\pm 2.5\%$ in November and $+2.5/-5\%$ in April (even with the deleted section discussed above left in). Offset variations, except for the deleted section, correlated fairly well with changes in the temperature measured by a sensor on the in-flight calibrator.

Figures 4.2 and 4.3 show the behavior of the radiometer offset for the November and April flights, respectively. The lower box in each figure shows the radiometer output, including offset, averaged over 100-second intervals, and the upper box shows the calibrator temperature. With the lockin amplifier blanked while the chopper crosses the horn, each 100-second interval represents 80 seconds of net integration time. Moon-contaminated data are not included in the plots, but Figure 4.3 shows the twenty-minute section of the April flight deleted from later analysis. The smooth curve in the radiometer output plots is a ten-term Legendre-series fit to the offset.

To remove the offset, data were averaged in 6.5-minute sections, one-quarter of the interval between calibrations. A piece-wise cubic spline through the averages was subtracted from the data, removing low-frequency drifts but not affecting signals at the gondola rotation frequency (0.81 RPM in November and 0.55 RPM in April). After the section in the April flight discussed above was deleted, residual offset for each 3.3 minute segment of data (half the 6.5

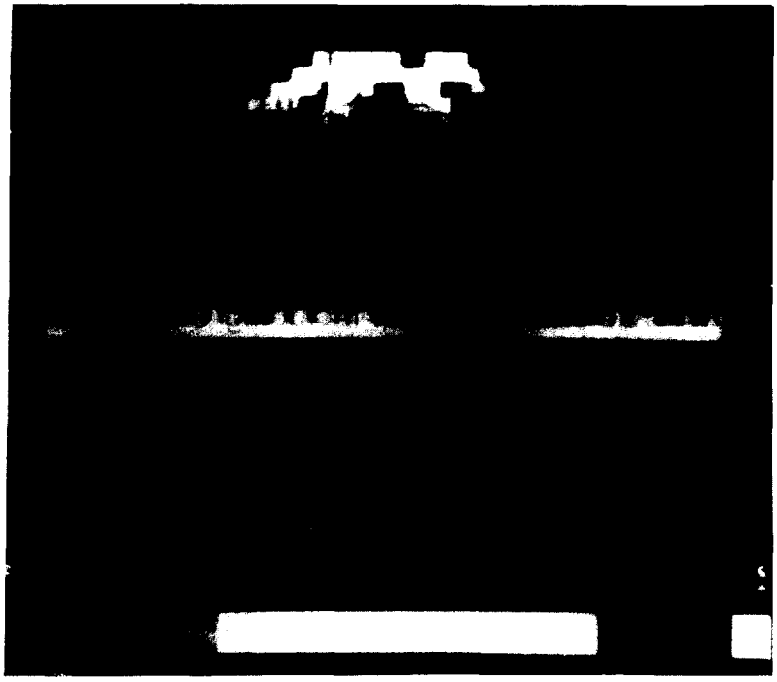

XBB 830-10236

Figure 4.1. Sine equal-area projection of the number of observations per pixel. Observation time equals 2.11 seconds times the number of observations. Declination of displayed region ranges from $-15°$ at the bottom to $+80°$ at the top; RA decreases from 24 hours at left to 0 hours at right. Pixels are 5° high in declination δ by $3°/\cos\delta$ wide in RA, having equal areas on the sky of 15 square degrees.

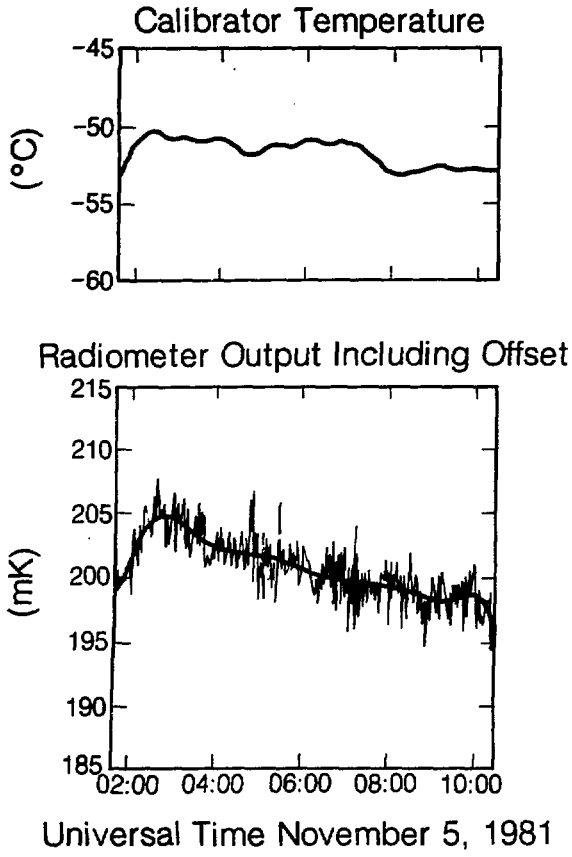

Figure 4.2. November 1981 Flight: Lower figure is radiometer offset in mK, averaged over 100-second intervals and excluding moon-contaminated data. Smooth curve is 10-term Legendre-series fit. Upper figure is calibrator temperature in degrees C. over the same period.

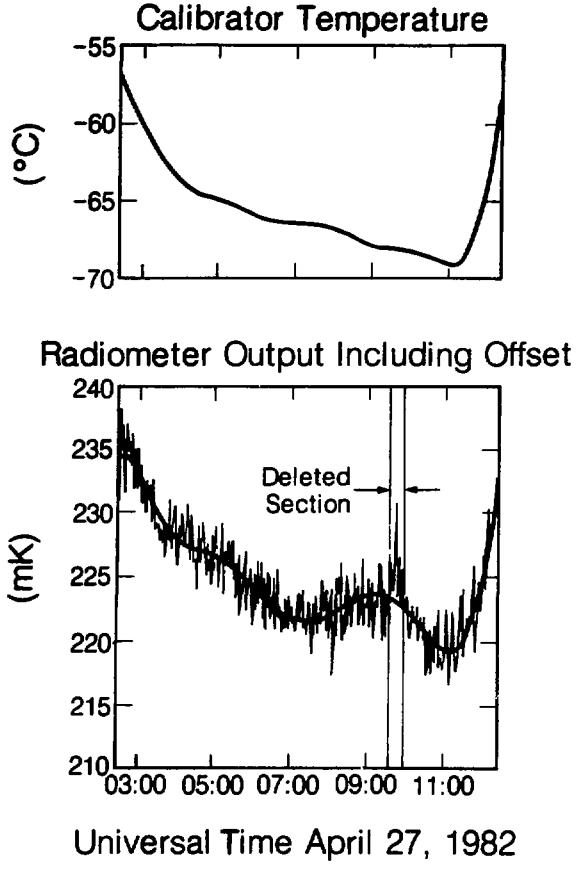

Figure 4.8. April 1982 Flight: Lower figure is radiometer offset in mK, averaged over 100-second intervals and excluding moon-contaminated data but showing the twenty-minute segment deleted from later analysis. Smooth curve is 10-term Legendre-series fit. Upper figure is calibrator temperature in degrees C.

minute averaging interval) was less than 2 mK except for three 3.3-minute segments of the April flight which had residual offsets under 3 mK.

The data analysis is insensitive to the technique used to remove the offset. Fitting and removing a 10-term or a 25-term Legendre series to the offset rather than a spline changes fitted parameters by less than 25% of the statistical error. Since the total variance of the data set after removal of a spline fit to the offset is less than the variance after removal of a Legendre series, the spline is a better approximation. Sky maps inverted from the data after a spline has been removed converge faster than when a Legendre series is used.

Although no sensor directly measured the temperature of the chopper wheel, an upper limit to the variation in chopper temperature synchronous with gondola rotation can be found using measurements of the calibrator temperature. The calibrator's small thermal mass and more exposed location should make it more sensitive than the chopper to synchronous temperature modulation. The temperature sensor on the in-flight calibrator survived whatever happened to the calibrator itself early in the April flight, so temperature variation could be examined. Synchronous variation of the calibrator temperature was less than 0.03° C at all times. Giving the chopper a synchronous variation of this amplitude would generate a spurious anisotropy signal of less than 0.03 mK.

4.5 Conversion to Antenna Temperature and Correction to Barycenter

After the data edits had been made and the offset removed, the radiometer output values were multiplied by the system calibration to yield the antenna temperature difference between beams. As is discussed further in Appendix C, the same calibration value was used for both flights, and observations of the in-flight calibrator in November indicated that this value did not change during a flight. Observations were referred to the solar system barycenter by subtracting from each data point the temperature difference generated by the earth's orbital

motion, assuming a blackbody CBR with a temperature of 2.7 K. The maximum value of this correction to either radiometer beam is 0.22 mK, and with the 90 degree opening angle between beams the maximum adjustment to their temperature difference is 0.31 mK. Therefore, a 30% error in this correction would change any data point by less than 0.1 mK.

Chapter 5

Data Analysis

5.1 Spherical Harmonic Fits

5.1.1 Results

The radiometer output is a measurement of the temperature difference between two parts of the sky. The most straightforward way to analyze the differences is to do a least-squares fit to a spherical harmonic multipole expansion. Table 5.1 gives the basis functions chosen, and the fitting procedure is described in Appendix D.

The best-fit dipole and quadrupole terms, excluding data taken less than five degrees from the galactic plane, are given in Table 5.2. The galactic cut eliminates 17% of the November data and 10% of the April data, or 13% of the total. The fitted terms change by less than one statistical standard deviation when data near the galactic plane is included (Table 5.6), and they are not significantly affected by including a galactic model term in the fits (Table 5.7). Galactic contributions are discussed further in Section 5.1.5.

The data from the two Texas flights analyzed in this work were all taken at constant latitude. As a result, the axisymmetric quadrupole term $Q_1(\frac{3}{2}\sin^2\delta - \frac{1}{2})$ and the dipole term $T_z \sin\delta$ cannot be decoupled, as can be seen from the following argument: The difference in values

Table 5.1. Spherical harmonic basis functions.

$$T(\hat{n}) = T_0 + \vec{T} \cdot \hat{n} + \sum_{i=1}^{5} Q_i \cdot q_i(\hat{n})$$

δ is declination measured north from celestial equator

α is right ascension measured east from 0

$\hat{n}$ is unit vector in direction of observation

Basis Function	Spherical Harmonic	Angular Dependence	Rectangular Representation
n_x	$-\sqrt{\frac{2\pi}{3}}(Y_{11} - Y_{1,-1})$	$\cos\delta\cos\alpha$	x
n_y	$i\sqrt{\frac{2\pi}{3}}(Y_{11} + Y_{1,-1})$	$\cos\delta\sin\alpha$	y
n_z	$\sqrt{\frac{4\pi}{3}}Y_{10}$	$\sin\delta$	z
q_1^*	$\sqrt{\frac{4\pi}{5}}Y_{20}$	$\frac{1}{2}(3\sin^2\delta - 1)$	$\frac{1}{2}(3z^2 - 1)$
q_2	$-2\sqrt{\frac{2\pi}{15}}(Y_{21} - Y_{2,-1})$	$\sin 2\delta\cos\alpha$	$2xz$
q_3	$2i\sqrt{\frac{2\pi}{15}}(Y_{21} + Y_{2,-1})$	$\sin 2\delta\sin\alpha$	$2yz$
q_4	$2\sqrt{\frac{2\pi}{15}}(Y_{22} + Y_{2,-2})$	$\cos^2\delta\cos 2\alpha$	$x^2 - y^2$
q_5	$-2i\sqrt{\frac{2\pi}{15}}(Y_{22} - Y_{2,-2})$	$\cos^2\delta\sin 2\alpha$	$2xy$

* not fitted for

of the Q_1 term between beams at declinations δ_a and δ_b is $\frac{3}{2}Q_1(\sin\delta_a - \sin\delta_b)(\sin\delta_a + \sin\delta_b)$. For constant balloon zenith declination δ_z and radiometer opening angle θ, the factor $\frac{3}{2}(\sin\delta_a + \sin\delta_b)$ has a fixed value equal to $3\sin\delta_z\cos(\theta/2) = 1.10$ for our latitude. The Q_1 differences are strictly proportional to the T_z differences, and as a result, the Q_1 term was not included in multipole fits. The true Q_1 component of the anisotropy, if any, will have been incorporated into the fitted T_z coefficient by the relation T_z (fitted) = T_z (true) + 1.10 Q_1 (true). All references to T_z in this thesis refer to the fitted T_z value.

Table 5.2. Global dipole-plus-quadrupole fit in mK antenna temperature. Data within 5 degrees of the galactic plane has been excluded. All errors are statistical only.

Term	Magnitude	Correlation Coefficients					
T_x	-2.760 ± 0.084	1.000	−0.094	0.032	−0.335	0.261	−0.018	0.045
T_y	0.541 ± 0.090		1.000	−0.008	0.254	−0.363	−0.097	0.048
T_z	-0.252 ± 0.076			1.000	0.090	0.100	0.078	0.235
Q_2	0.118 ± 0.102				1.000	−0.126	−0.053	0.007
Q_3	0.129 ± 0.100					1.000	−0.033	0.161
Q_4	-0.050 ± 0.069						1.000	0.055
Q_5	0.070 ± 0.065							1.000
$\chi^2 = 25811/25354$								

5.1.2 Data Weighting

Since the fluctuations in radiometer output throughout a flight are consistent with noise having constant variance, all data from a given flight are weighted equally. The data variance used for each flight is half the mean-squared difference between consecutive two-second integrated output values. The square root of this variance, proportional to the system noise temperature, was 10.0 ± 0.1 mK for the November flight and 9.9 ± 0.1 mK for April. The contribution of the dipole anisotropy signal to the RMS point-to-point differences is under 0.05%. Once this contribution is removed, half the mean squared difference provides an accurate measure of the true variance of the data if the noise is white (equal power per unit frequency). If there is relatively enhanced power at longer time scales, the mean squared point-to-point difference underestimates the true variance.

The variance of the entire November data set after offset removal is $5.2 \pm 1.1\%$ higher than the variance determined from point-to-point differences; removing the dipole signal gives a variance $0.8 \pm 1.1\%$ higher than that determined from the differences. For the April flight, the

variance of the entire data set after offset removal is $8.8 \pm 1.1\%$ higher than that found from the differences. Removing the dipole signal accounts for about half of the excess, leaving a variance for the entire data set $3.1 \pm 1.1\%$ greater than that computed from the point-to-point differences. This excess suggests some noise power with a period longer than 4 seconds remains even after the anomalous twenty-minute section (see Chapter 4) has been removed. If the weighting used for the April data is decreased by 3% to account for the excess variance, no fitted coefficient changes by more than 12% of the statistical error.

5.1.3 Chi-Square Statistics and Hourly Averages

The χ^2 value presented in Table 5.2 of 25811 for 25324 degrees of freedom (DOF) is not very meaningful. Taken literally, it represents a 2% probability that the data can be modeled by dipole and quadrupole coefficients alone. However, χ^2 statistics with so many degrees of freedom are very sensitive to the values used for the formal errors σ_i of the individual data points. A 1% increase in the uncertainty assigned to each of the 25300 observations lowers χ^2 from 25810 to 25301 and increases the confidence level from 2% to 54%. While the χ^2 values computed in the global fits may be used to compare one fit to another, they are not useful goodness-of-fit indicators in the absence of a very accurate determination of uncertainty σ_i of each observation.

By averaging the data in bins before fitting, the number of degrees of freedom is drastically reduced and the χ^2 values are much less sensitive to the values used for the individual-observation errors. In addition, it is possible to determine the uncertainties in each bin average from the scatter within the bin rather than from some external estimate of the data uncertainty.

A convenient way to group balloon-gathered anisotropy data is to Fourier-analyze data gathered during some interval as a function of gondola azimuth angle ϕ (Corey 1978; Cheng *et al.*, 1979). The dipole and quadrupole anisotropy can be determined from the $\cos\phi$ (north – south) and $\sin\phi$ (east – west) coefficients alone and will not contribute to $\cos n\phi$ or $\sin n\phi$ coefficients

Table 5.8. Dipole-only parameters determined from hourly averages, in mK antenna temperature. Data within 5 degrees of the galactic plane has been excluded. Errors are statistical only.

Term	Include all Data	Exclude Final Interval of Each Flight
T_x	-2.74 ± 0.08	-2.75 ± 0.09
T_y	0.55 ± 0.08	0.54 ± 0.08
T_z	-0.28 ± 0.07	-0.29 ± 0.08
Chisquare/DOF	46.42/39	33.24/35
Confidence Level	19.3%	55.3%

for n $>$ 1. No anisotropy power of any order is contained in coefficients with even n, since any celestial signal must change sign as the gondola rotates 180°. The expressions relating the dipole and quadrupole parameters to the $\cos\phi$ and $\sin\phi$ coefficients and the radiometer opening angle are given in Appendix G.

The 90 GHz data has been binned into 54-minute intervals (two calibration segments) for which $\cos\phi$ and $\sin\phi$ Fourier coefficients have been determined. The dipole-only anisotropy determined from the Fourier coefficients is given in Table 5.3, and the dipole-plus-quadrupole fit is presented in Table 5.4. Figure 5.1 shows the hourly sine and cosine coefficients. The curves in Figure 5.1 are the coefficients which would be generated by the combined dipole and quadrupole anisotropy in Table 5.4. The residual sine and cosine coefficients between the data and the dipole-only fit are shown in figure 5.2 along with smooth curves giving the difference between the dipole-plus-quadrupole fit and the dipole-only fit.

Since the individual two-second observations are spaced 7 to 10 degrees apart in azimuth angle, short segments of data do not provide good azimuthal coverage. As a result, Fourier

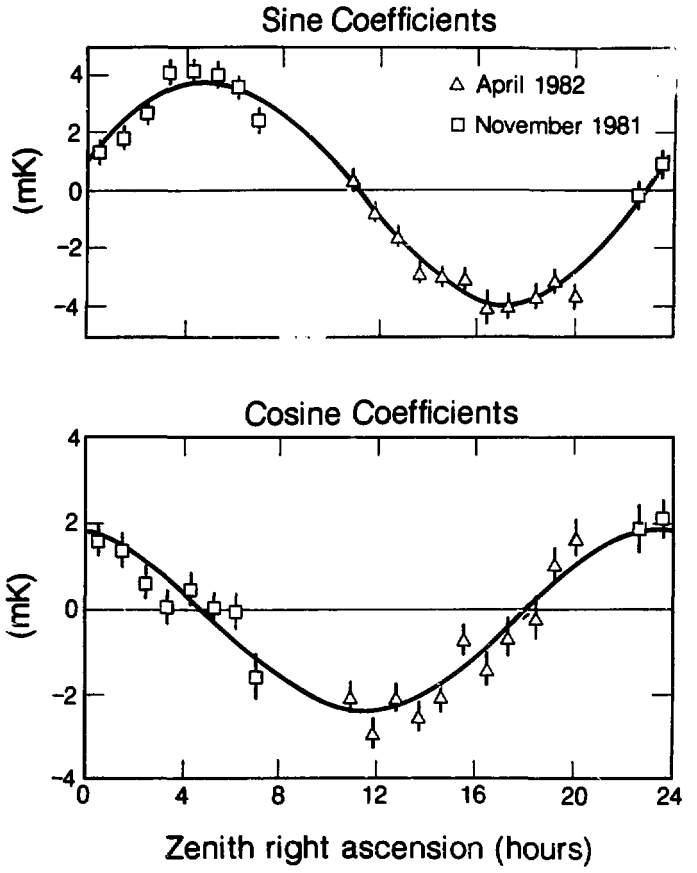

Figure 5.1. Hourly sine and cosine anisotropy coefficients. Data within 5 degrees of the galactic plane has been excluded. Curves are the sine and cosine terms corresponding to the dipole-plus-quadrupole fits in Table 5.4.

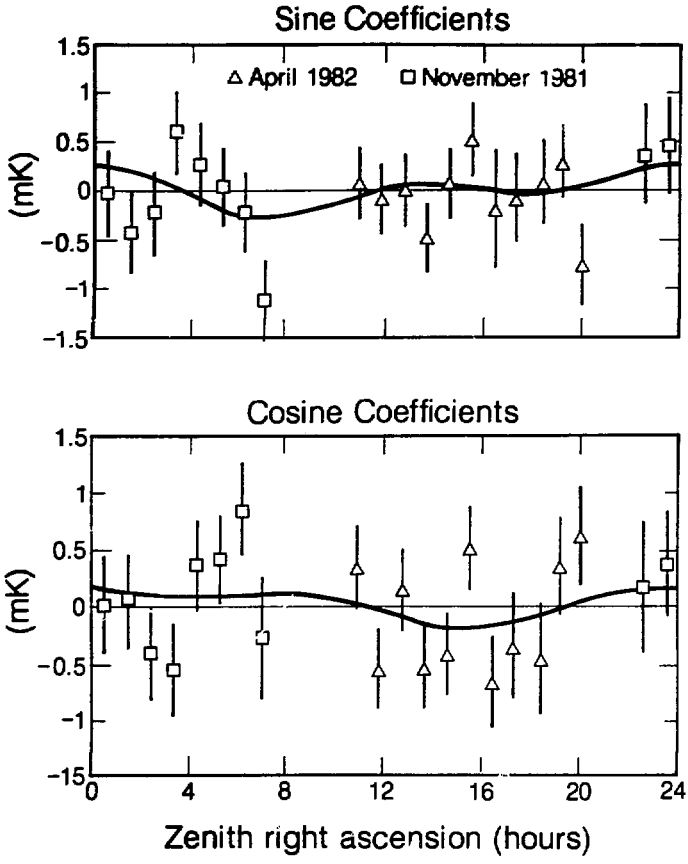

Figure 5.2. Points are residuals between hourly sine and cosine anisotropy coefficients and the dipole-only fit given in Table 5.3. Curves are the difference between dipole-plus-quadrupole (Table 5.4) and dipole-only (Table 5.3) fits. Data within 5 degrees of the galactic plane has been excluded.

analyses were done for each 54-minute interval in its entirety. The errors of the hourly coefficients are not determined from a scatter of individual coefficients, as would be possible if coefficients for many small intervals were averaged, but instead represent statistical errors of the Fourier fits. The same individual-observation uncertainties used in the global spherical harmonic fits are also used to estimate errors in the Fourier coefficients. Since the fits in Table 5.4 have 35 degrees of freedom, as opposed to the 25324 in Table 5.2, the χ^2 value in Table 5.4 is much less sensitive to small changes in the individual observation uncertainties.

The χ^2 for the dipole-only fit in Table 5.3 is 46.42 for 39 degrees of freedom (19.3% confidence level). Adding quadrupole terms (Table 5.4) reduces χ^2 to 42.07 for 35 DOF without improving the confidence level (19.1%) and barely changing the dipole terms, showing that quadrupole terms are not compelled by the data. The value of χ^2 is slightly higher than statistical error alone would be expected to generate. Essentially all the excess is contributed by the last intervals in both the November and April flights: the last November point (RA 7.09 hours) contributes a χ^2 of 7.31, and the last April point (RA 20.12 hours) contributes 5.78. This allocation of the chi-square motivated a search for systematic effects which could have influenced the ends of the flights. Positional error should be minimized at the end of the flight since the impact point is well determined. Synchronous heating effects were not detected in the calibrator temperature sensor and would be highly unlikely in the November flight, which ended at a local solar time of 04:23 when the sun was 20 degrees below the horizon. At the end of the April flight (06:18 local solar time), the sun was 14 degrees above the horizon or 9 degrees above horizontal (the horizon at balloon altitude being 5 degrees below horizontal). The sun was therefore 36 degrees off the beam and should not have contributed a detectable signal unless diffraction over the groundshields has been grossly underestimated (see Section 5.3.1.5). The top one-half inch or so of the chopper wheel may have been directly illuminated at termination.

Fits were done excluding the last hourly coefficients in each flight to test the sensitivity

Table 5.4. **Combined dipole-plus-quadrupole anisotropy determined from hourly coefficients, in mK antenna temperature. Data within five degrees of the galactic plane has been excluded; errors are statistical only.**

Term	Include all Data	Exclude Final Interval of Each Flight
T_x	-2.74 ± 0.09	-2.71 ± 0.09
T_y	0.55 ± 0.09	0.49 ± 0.10
T_z	-0.25 ± 0.07	-0.28 ± 0.08
Q_2	0.11 ± 0.10	0.05 ± 0.11
Q_3	0.12 ± 0.10	0.18 ± 0.11
Q_4	-0.03 ± 0.07	0.03 ± 0.07
Q_5	0.08 ± 0.06	0.02 ± 0.07
Chisquare/DOF	42.07/35	29.51/31
Confidence Level	19.1%	54.3%

of the fits to those points. The resultant parameters, given in the second columns of Tables 5.3 and 5.4, change by less than one statistical standard deviation. The χ^2 for the dipole-only fit drops to 33.24 for 35 DOF, with the confidence level rising to 55.3%. The dipole-plus-quadrupole χ^2 becomes 29.51 for 31 DOF at the 54.3% confidence level. Although it is certainly not valid to exclude data simply because they generate large contributions to χ^2, it is reassuring that the dipole and quadrupole parameters do not change significantly when the possibly discrepant points are deleted. Since no unambiguous evidence of systematic error in the ends of the flights could be found, all data were used in the global fits. Systematic error is explored further in Section 5.3.

5.1.4 Individual Flight Dipole Fits

Each of the November or April flights, taken alone, covers about half the northern sky.

Combined dipole-plus-quadrupole fits to data with such limited sky coverage are highly correlated and are not very useful. However, dipole-only fits to each individual flight give meaningful results which are shown in Table 5.5 along with the dipole-only fit to the two flights combined. Using the comparison analysis described in Appendix D, the difference between the two single-flight dipole fits is consistent with zero at the 21% confidence level.

5.1.5 Galactic Effects and Models

One of the prime motivations for measuring anisotropy at 90 GHz was to minimize the galactic contribution. This hope appears to have been fulfilled. Including or excluding the galactic plane has little effect on dipole and quadrupole fits, as is shown in Table 5.6. Galactic emission at 90 GHz is thought to be dominated by thermal emission from interstellar dust. However, maps of the galactic dust distribution, inferred from infrared emission, have not yet (i.e. pre-IRAS) been made over large areas. Two models for galactic emission at 90 GHz, convolved over the radiometer beamwidth, were therefore constructed. The simplest is a slab galaxy, modeled by a cosecant distribution in galactic latitude which levels off five degrees from the plane. Since dust and neutral hydrogen are correlated, a better estimate of the dust distribution may be given by surveys of neutral hydrogen emission at 21 cm wavelength. Two surveys covering the northern sky (Heiles and Habing, 1974; Weaver and Williams, 1973) were integrated over the velocity-dispersed line profiles and convolved with the radiometer beam to form the second galactic model, which is shown in celestial coordinates in Figure 5.3.

Fits including galactic models are given in Table 5.7. The fitted "galaxy model" coefficient in Table 5.7 represents galactic emission averaged over the region within five degrees of the galactic plane, in mK. Galaxy model 1, the truncated cosecant law, has maximum and average values within five degrees of the plane of 11.5 with respect to its value at the pole. Model 2, the convolved neutral hydrogen map, reaches a maximum value of 34 times its polar value at

Table 5.5. **Dipole-only fits to individual flights and to combined flights in mK antenna temperature. Data within five degrees of the galactic plane has been excluded, and errors are statistical only.**

November Flight

Term	Magnitude	Correlation Coefficients		
T_x	$-2.532 \pm .136$	1.000	0.319	0.553
T_y	$0.725 \pm .147$		1.000	0.509
T_z	$-0.039 \pm .146$			1.000
$\chi^2 = 11465/11296$				

April Flight

Term	Magnitude	Correlation Coefficients		
T_x	$-2.833 \pm .114$	1.000	0.220	-0.369
T_y	$0.514 \pm .113$		1.000	-0.379
T_z	$-0.310 \pm .110$			1.000
$\chi^2 = 14346/14059$				

Both Flights

Term	Magnitude	Correlation Coefficients		
T_x	$-2.757 \pm .077$	1.000	0.075	0.042
T_y	$0.545 \pm .080$		1.000	-0.009
T_z	$-0.283 \pm .073$			1.000
$\chi^2 = 25816/25363$				

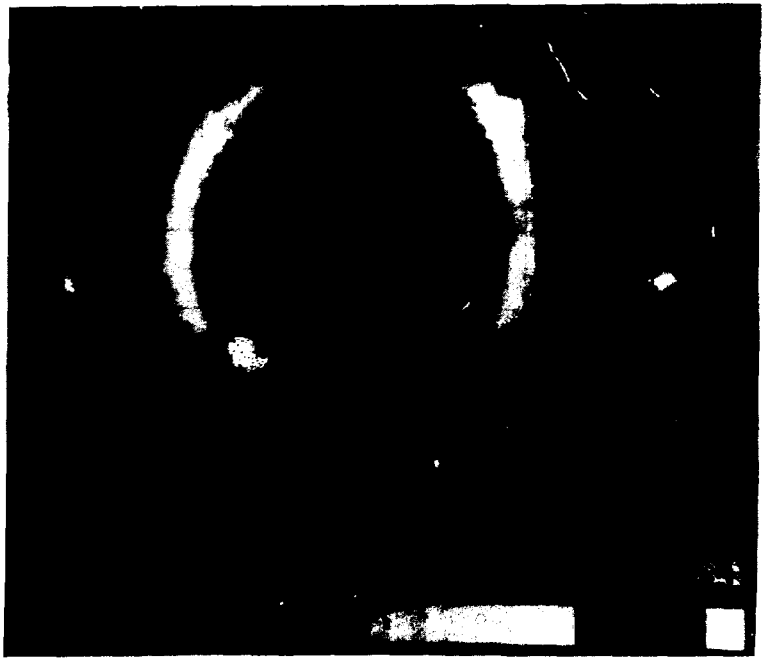

XBB 830-10234

Figure 5.8. Sine equal-area projection of 21-cm HI emission in the northern sky, used for galaxy model 2. *Map coordinates are the same as for* Figure 4.1. Units are proportional to integrated 21-cm line strength averaged over a frequency range which includes most galactic HI emission. Data are from Heiles and Habing, (1973) and Weaver and Williams, (1974)

Table 5.6. **Effects of galactic cuts on dipole-plus-quadrupole fits, in mK antenna temperature. All errors are statistical only.**

Term	No Galactic Cut	Cut $\|b\| < 5°$	Cut $\|b\| < 10°$
T_x	$-2.73 \pm .08$	$-2.76 \pm .08$	$-2.77 \pm .09$
T_y	$0.47 \pm .08$	$0.54 \pm .09$	$0.56 \pm .10$
T_z	$-0.22 \pm .07$	$-0.25 \pm .08$	$-0.22 \pm .08$
Q_2	$0.18 \pm .10$	$0.12 \pm .10$	$0.14 \pm .11$
Q_3	$0.19 \pm .09$	$0.13 \pm .10$	$0.11 \pm .11$
Q_4	$-0.06 \pm .06$	$-0.05 \pm .07$	$-0.04 \pm .08$
Q_5	$0.05 \pm .06$	$0.07 \pm .06$	$0.05 \pm .07$
Number of Points	29161	25363	21691

one spot on the galactic plane and averages 23 times the polar intensity over the band within five degrees of the galactic equator.

Table 5.7 implies an averaged galactic emission over the region less than five degrees from the galactic plane of 0.53 ± 0.22 mK for model 1 and 0.50 ± 0.21 mK for model 2. Neither galactic model yields a significant fit when data within five degrees of the galactic plane is excluded.

5.2 Sky Maps

In addition to being fitted to spherical harmonics, the data can in principle be inverted to yield a map of the sky. Formally this involves a least-squares fit of the data to coefficients representing the temperature of each pixel in the inverted map. Since the data are insensitive to the addition of a constant to all points in the map, an additional parameter such as the temperature of a given cell must be specified to determine the solution uniquely. Furthermore, depending on the sky coverage and the interconnectedness of the data (i.e., the way in which map elements are linked to each other by measurements), other degeneracies can exist. With balloon

Table 5.7. Dipole-plus-quadrupole fits, in mK antenna temperature, with and without galactic models. Galactic model coefficients represent emission averaged over the region within five degrees of the galactic plane. Correlation coefficients between the galactic terms and multipole parameters are shown; coefficients among the multipole parameters are similar to those given in Table 5.2. No galactic cuts were made, and all errors are statistical.

Fits				Galaxy Term Correlation Coefficients	
Term	No Galaxy Model	Model 1	Model 2	Model 1	Model 2
T_x	$-2.73 \pm .08$	$-2.72 \pm .08$	$-2.72 \pm .08$	.05	.04
T_y	$0.47 \pm .08$	$0.49 \pm .08$	$0.50 \pm .08$	.10	.12
T_z	$-0.22 \pm .07$	$-0.25 \pm .07$	$-0.25 \pm .07$	$-.19$	$-.17$
Q_2	$0.18 \pm .10$	$0.06 \pm .11$	$0.05 \pm .11$	$-.47$	$-.50$
Q_3	$0.19 \pm .09$	$0.17 \pm .09$	$0.16 \pm .09$	$-.09$	$-.11$
Q_4	$-0.06 \pm .06$	$0.03 \pm .08$	$0.03 \pm .07$	.54	.49
Q_5	$0.05 \pm .06$	$0.11 \pm .06$	$0.10 \pm .06$	.39	.28
Galaxy Model 1 (mK, equatorial)	—	$0.53 \pm .22$	—	1.00	—
Galaxy Model 2 (mK, equatorial)	—	—	$0.50 \pm .21$	—	1.00
χ^2	29760.39	29754.78	29754.15		
DOF	29153	29152	29152		

data taken at a single latitude, the radiometer compares the sky at one declination with exactly one other declination. An intensity distribution independent of right ascension and symmetric in declination about the midpoint between the two beams will not be seen in, or recoverable from, differential measurements.

Making a sky map with 3 degree by 5 degree pixels from this data set is equivalent to inverting a 2269 by 2269 matrix whose non-diagonal terms represent the differential measurements connecting different pixels. Fortunately for the analysis but unfortunately for the quality of the end result, very few (20000) of the over five million terms are non-zero. Details of the iterative Gauss-Seidel inversion used to create a map are given in Appendix E. The iterations converged, but since the matrix is poorly conditioned, it is not clear how well the solution represents the original intensity distribution.

A reconstructed sky map from the flight data is shown in Figure 5.4. Spherical harmonic fits to the map qualitatively recover the coefficients found in direct fits to the data for both flight data and Monte Carlo flight simulations. However, the quantitative agreement between direct fits and fits to reconstructed maps is poor, with there being only a 1% chance that the fits represent the same data set when considered as independent measurements. Furthermore, the inversion procedure introduces noise. In maps reconstructed from flight data, the chi-square for spherical harmonic fits to the map increased with the number of iterations performed in inverting the map. Comparison of single and double precision inversion routines showed that numerical error was not responsible for the increase. The same increase in noise was observed in fits to maps inverted from Monte Carlo flight simulations.

5.3 Systematic Error Analysis

Errors quoted in the fits earlier in this chapter represent only statistical uncertainty resulting from radiometer noise. Two kinds of systematic errors must also be estimated — those

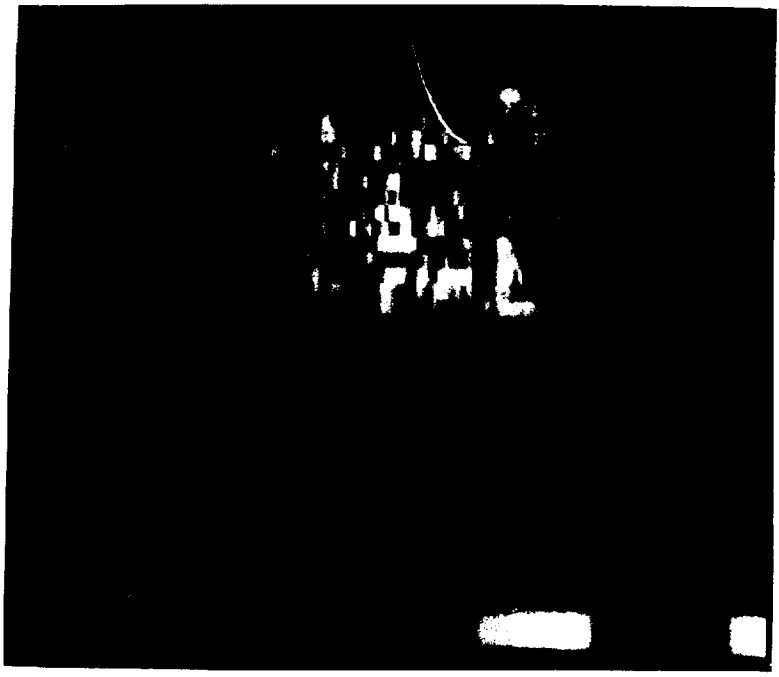

XBB 8311-10235

Figure 5.4. Reconstructed 90 GHz sky map as a sine equal-area projection in the same coordinates as Figures 4.1 and 5.3. Scale runs from -8 to 8 mK.

such as atmospheric or galactic emission which can generate spurious signals, and those such as pointing errors which can have the effect of generating quadrupole terms from the existing dipole anisotropy.

5.3.1 Errors of the First Kind

5.3.1.1 Galactic Sources

At centimeter and longer wavelengths, galactic emission is primarily synchrotron radiation (antenna temperature $T_a \sim \nu^{-2.8}$) and thermal brehmsstrahlung emission ($T_a \sim \nu^{-2.1}$). Bounds on these contributions are obtained by scaling lower frequency surveys. Scaling the Haslam *et al.* (1982) 408 MHz galactic survey, which is dominated by synchrotron radiation, limits the maximum synchrotron contribution anywhere in the sky at 90 GHz to under 0.1 mK when convolved over the radiometer beamwidth.

Data on thermal emission from ionized hydrogen regions has been collected, convolved with a 7 degree beam, and referred to 33 GHz by Witebsky (1978). Scaling these data to 90 GHz with a temperature spectral index of -2.1 gives a maximum intensity of 0.5 mK on the galactic plane for the Cygnus arm of the galaxy. The maximum value more than five degrees off the galactic plane is about 0.1 mK.

At millimeter wavelengths and shorter, dust emission is the primary galactic contaminant. The spectral and spatial distribution of dust emission is poorly known, and observations made at other frequencies cannot be scaled to 90 GHz (3 cm^{-1}) as easily for dust as for thermal and synchrotron radiation. Owens *et al.* (1979) measured dust emission in the galactic plane in the 10 to 25 cm^{-1} band. For a source having an emissivity proportional to frequency squared over that band, their observed flux corresponds to antenna temperatures at 22 cm^{-1} averaging about 28 mK on the galactic plane between 0 and 45 degrees galactic longitude. Only

one source, having a peak antenna temperature of 15 mK, was found more than five degrees off the plane. Owens *et al.* state that their "best guess" for scaling observations to different frequencies is to take the emissivity to be proportional to frequency squared.

The best experimental limits to the intensity of dust emission at 90 GHz are the fits to galactic models in this thesis. These show the galactic emission less than five degrees from the galactic plane to be on the order of 0.5 mK. Any diffuse thermal emission, which was not included in the compilation by Witebsky (1978), is included in this limit.

Possible effects of diffuse off-plane galactic emission on multipole fits were investigated by generating simulated observations of an extended source in the region of the off-plane emission reported by Owens *et al.* The worst-case source intensity is given by scaling the 15 mK Owens *et al.* intensity to 90 GHz (3 cm^{-1}) using a temperature spectral index of 1.5. The center frequency of the Owens *et al.* apparatus for a source with that spectral index is 16.7 cm^{-1} (S. Meyer, private communication). Scaling from 16.7 cm^{-1} with a temperature spectral index of 1.5 gives a source intensity at 3 cm^{-1} of 1.1 mK. Such a source would contribute $+70$ μK to Q_2 and would change the other dipole and quadrupole terms by less than 50 μK.

5.3.1.2 Interplanetary Sources

At still shorter wavelengths (10 to 100 micron), the dominant source of diffuse emission is likely to be interplanetary dust particles (zodiacal light). Zodiacal emission at wavelengths longer than its peak at about 10 microns is not well characterized. Measurements are not inconsistent with a 300 K spectrum having an emissivity proportional to frequency and an optical depth at 10 microns of about 5×10^{-8} (NASA, 1977). This spectral dependence gives a zodiacal contribution of tens of nanokelvins at 90 GHz.

5.3.1.3 Ionospheric Free-Free Emission

A more local source of extraneous radiation is the residual atmosphere above the balloon. Corey (1978) has calculated a firm upper limit of 0.6 mK on ionospheric free-free emission at 19 GHz with a probable value significantly less than that. The antenna temperature of thermal free-free emission is inversely proportional to frequency squared, so the corresponding upper bound at 90 GHz is a negligible 0.03 mK.

5.3.1.4 Atmospheric Molecular Emission

Molecular emission from the atmosphere can be estimated from the emission line parameters of atmospheric constituents, together with a description of atmospheric physical parameters as a function of altitude. The Air Force Cambridge Geophysical Laboratory has compiled line parameters from the radio to the optical (referenced in Weiss, 1980), and the 1962 U. S. Standard Atmosphere (Cole, 1965; tabulated in Ulaby *et al.*, 1981) describes atmospheric physical properties. Calculated zenith atmospheric emission at 30 km is shown in Figure 2.2 for frequencies less than 150 GHz. At 90 GHz, the dominant contribution is 5 mK from the pressure-broadened wings of oxygen magnetic dipole transitions centered at 60 and 120 GHz. Wings of rotational water lines, the nearest of which are at 22 and 183 GHz, add another 0.2 mK. The ozone spectrum is full of rotational lines in the microwave region, but the 90 GHz radiometer RF passband between 88.4 and 91.6 GHz does not include any major ones and at 30 km picks up about 0.1 mK from ozone line wings. Both the zenith column density and the line widths increase with pressure, so off-peak atmospheric emission grows faster than linearly with pressure. At 27.5 km, the oxygen emission is 15 mK and it increases to 40 mK at 25 km.

For a layered slab atmosphere with zenith temperature T_0, the emission at zenith angle Θ is given by

$$T(\Theta) = T_0 \sec \Theta. \tag{5.1}$$

A gondola tilt angle of $\Delta\theta$ generates a difference between the beam zenith angles of $2\Delta\theta$ and a differential atmospheric signal of

$$T(\Theta, \Delta\theta) = 2T_0 \sec \Theta \tan \Theta \Delta\theta. \tag{5.2}$$

For radiometer beam zenith angles of 45 degrees at 27.5 km altitude, the atmospheric signal is 23 mK and the differential atmospheric signal is 0.8 mK per degree radiometer tilt.

5.3.1.5 Ground Pickup

The earth has a radiometric temperature on the order of 300 K at 90 GHz. The antenna sidelobe pattern, together with the groundshields, must therefore provide 65 db of rejection to ensure that radiation from the ground contributes less than 0.1 mK. Since it was not possible to measure the far-sidelobe radiometer response after the gondola was lost, we instead calculate an estimate of the power diffracted over the groundshield.

The groundshield is modeled by a cylindrical cone having an opening angle equal to that of the actual hexagonal shield, with a radius equal to that of the hexagon's inscribed circle. For the calculation, the horn aperture is taken to be in the center of the cone, 12.7 cm below the plane of the cone's edge, and pointing upwards at a 45 degree angle. (The real horn was at the same depth and angle but was set back 4.3 cm behind the chopper wheel, which was at the center of the shield.)

At each point on the edge of the shield, the far-field antenna pattern is used to determine the antenna gain. However, with the far-field approximation strictly valid for regions farther than $\pi a^2/\lambda \approx 60$ cm, with a the horn radius, using far-field patterns for the groundshield edge 33 cm away is not strictly justified. Radiation from each region on the ground is assumed to diffract

over only that section of the groundshield edge directly between it and the horn. Fresnel theory for diffraction over a conducting straightedge is used to compute the ratio of the power diffracted into the horn to the power incident (Born and Wolf, 1964, p. 578). The diffracted power over each portion of the edge, multiplied by the appropriate antenna gain, is integrated around the groundshield to give the total diffracted contribution.

The intensity of radiation diffracted over a conducting edge is polarization-dependent. In the polarization accepted by the horn, E field parallel to the shield edge, the interior shield diffracts an estimated 0.03 mK into the horn. Diffracted power in the rejected mode is 0.98 mK.

The accuracy of this calculation, in light of the assumptions made, is certainly not high. However, several factors indicate that ground contamination may be less than that estimated here. On all flights, there was shielding in addition to the interior hexagonal shield. In November, 1981, panels extending the hexagonal groundshield horizontally for 13 cm were attached to all six sides, requiring ground radiation to diffract around two edges to reach the horn. On the April, 1982 flight, a second groundshield completely surrounded the gondola; the tops of the two shields were at the same height which again required ground radiation to diffract twice in order be detected. Furthermore, only the anisotropy in diffracted ground radiation can contaminate CBR anisotropy data. Although the radiometric temperature of seawater is on the order of 100 K less than that of land (Ulaby *et al.*, 1981), atmospheric emission reflected off the water and also added between the ground and the balloon minimize the observed temperature difference between land and water. Since power from near the horizon dominates the diffracted contribution, the atmospheric path lengths are long enough for their optical depth to become appreciable. If the maximum antenna temperature difference from horizon to horizon is 30 °C, the effect of anisotropic ground emission is an order of magnitude less than the total power diffracted into the horn.

5.3.1.6 Balloon Contributions

The balloon emits thermal radiation and also reflects power from the ground. Both contributions are negligibly small. The absorption coefficient of polyethylene was measured to be $1.5 \times 10^{-2}\text{cm}^{-1}$ at 90 GHz. The balloon thickness t is 0.5 mil $= 1.3 \times 10^{-3}$ cm. Averaging the $4\pi r^2 t$ volume of the polyethylene membrane over its projected area of πr^2 gives an average projected thickness of $4t$ or 5.2×10^{-3} cm, for a mean optical depth of 7.8×10^{-5}. At a physical temperature of 300 K, the balloon would have a brightness temperature of 23 mK.

The reflection coefficient for a thin dielectric film of thickness t and dielectric constant n at normal incidence is

$$R = \left(\frac{4\pi n t}{\lambda}\frac{n-1}{n+1}\right)^2.$$

For a 1.3×10^{-3} cm film of polyethylene ($n \approx 1.5$) at $\lambda = 0.33$ cm, $R = 2.1 \times 10^{-4}$. Reflected earth power will have a brightness temperature of $R \times 300$ K or 62 mK. Although the reflection coefficient increases as the angle of incidence increases, reflection paths having incidence angles greater than 50 degrees do not intercept the earth and need not be considered.

Summing the two contributions gives the balloon a brightness temperature of 87 mK when viewed head-on. Since all points on the balloon are at least 29 degrees off the antenna axis, the antenna gain over the balloon is less than 3.0×10^{-5}. Using this bound as an upper limit and integrating over the balloon gives a maximum emitted plus reflected contribution to the radiometer signal of 23 μK.

5.3.1.7 Synchronous System Modulations

Modulations in system parameters (gain, offset) synchronous with gondola rotation will be interpreted as a spurious anisotropy signal. As discussed in Chapter 3, signals generated by rotation within the earth's magnetic field are under 0.1 mK; variations in the chopper wheel's

physical temperature bounded in Chapter 4 induce a signal less than 0.03 mK. Variations of the second (non-cryogenic) IF amplifier temperature synchronous with balloon rotation were found to be less than 0.025 °C during flight. With the temperature dependence of the second IF gain measured to be less than 0.5% per degree C, temperature-induced gain variations acting on the 200 mK offset generate a spurious synchronous signal of less than 30 μK.

5.3.2 Errors of the Second Kind

5.3.2.1 Calibration Uncertainty

Determination of the system calibration constant, known to $\pm 6\%$, is discussed in Appendix C. The calibration was found to be the same throughout a flight (to 1%) and from one flight to another (to 3%). Unmodeled variation in the system calibration from flight to flight or within a flight would be a source of error which would have the effect of taking part of the dipole anisotropy and attributing it to higher order moments. These errors were bounded by sensitivity studies in which the system gain was assumed to vary within or between flights. The consequent changes in the values for fitted multipole parameters indicate possible effects of calibration errors. Varying the relative November to April calibration by $\pm 3\%$ changes the fitted value of T_x by 40 μK, T_y and T_z by less than 20 μK, the quadrupole parameters Q_2 and Q_3 by less than 10 μK, and Q_4 and Q_5 by less than 20 μK.

The error in the absolute calibration of 6% cannot put dipole power into the quadrupole terms. Instead, it introduces an uncertainty in each coefficient proportional to the coefficient's magnitude and is significant only for T_x, where the 170 μK absolute calibration uncertainty is the dominant error.

5.3.2.2 Pointing Errors

Errors in determining the gondola orientation can also redirect the dipole anisotropy into other dipole or higher order terms. Moon and sun observations in Texas (November, 1981) and in Brazil (November, 1982) indicate that the azimuth angle of the radiometer beams is known to ± 1.5 degrees. Total error in the radiometer beam positions is taken to be less than ± 2 degrees.

Sensitivity studies were done in which the calculated azimuth angle of the gondola was skewed by ± 2 degrees for the November and April flights. Since different magnetometers were used for the two flights, the errors in azimuth for November and for April are not necessarily correlated, so the results were added in quadrature. The total change in the T_x component was less than 20 μK, T_y less than 70 μK, T_z less than 50 μK, Q_2 and Q_3 less than 40 μK, and Q_4 and Q_5 less than 30 μK.

5.4 Summary and Conversion to Thermodynamic Temperature

The breakdown of the total estimated errors on the multipole parameters given in Table 5.2 are shown in Table 5.8. The specified contributions itemized in Section 5.3 are listed along with the statistical errors, and all components are summed in quadrature to give the total error in microKelvins.

The dipole and quadrupole anisotropy coefficients, with total errors, are given in Table 5.9 both in antenna temperature and in thermodynamic temperature corresponding to a 2.7 K CBR temperature. The conversion from antenna to thermodynamic temperature is discussed more fully in the following chapter.

Table 5.8. Contributions to total error of dipole and quadrupole parameters, in microKelvins.

Term	Statistical Error	Absolute Calibration	Relative Calibration	Pointing Error	Total Error
T_x	80	170	40	20	190
T_y	90	30	20	70	120
T_z	80	20	20	50	100
Q_2	100	10	10	40	110
Q_3	100	10	10	40	110
Q_4	70	0	20	30	80
Q_5	60	0	20	30	70

Table 5.9. Dipole-plus-quadrupole anisotropy at 90 GHz in antenna temperature and in thermodynamic temperature. Error estimates include systematic errors.

Term	Antenna Temperature	Thermodynamic Temperature (for $T_{\rm CBR} = 2.7$ K)
T_x	-2.76 ± 0.19	-3.40 ± 0.23
T_y	0.54 ± 0.12	0.67 ± 0.15
T_z	-0.25 ± 0.10	-0.31 ± 0.12
Q_2	0.12 ± 0.11	0.15 ± 0.14
Q_3	0.13 ± 0.11	0.16 ± 0.14
Q_4	-0.05 ± 0.08	-0.06 ± 0.10
Q_5	0.07 ± 0.07	0.09 ± 0.09

Chapter 6

Interpretation

6.1 Dipole Anisotropy

The dipole anisotropy measured by this experiment is presented with total errors in Table 6.1. Table 6.2 repeats these results in spherical coordinates and also includes results of the most recent publications by the Princeton and the Berkeley groups. Not included in Table 6.2 is Lubin *et al.*, (1983a), the initial publication of the results reported in this thesis. Those initial results differ from the ones reported here primarily in a 6% (1 σ) adjustment of the value used for the system calibration. The calculation of system gain used in the initial results included a term based on the in-flight pop-up calibrator observations which increased slightly the calibration (mK/volt) at altitude relative to that on the ground. Further analysis has shown that the pop-up calibrator observations on the ground were not sufficiently well-determined to justify the increase, and no such correction has been applied in this work. See Appendix C.

6.1.1 Direction

The direction of the dipole measured by this experiment agrees with that of the others in Table 6.2 except for a statistically significant discrepancy in declination with respect to Smoot

Table 6.1. 90 GHz dipole-only anisotropy in antenna temperature and in thermodynamic temperature for $T_{CBR} = 2.7$ K. Data within five degrees of the galactic plane has been excluded, and error estimates include systematic errors.

Term	Antenna Temperature	Thermodynamic Temperature (for $T_{CBR} = 2.7$ K)
T_x	-1.76 ± 0.19	-3.40 ± 0.23
T_y	0.54 ± 0.11	0.67 ± 0.14
T_z	-0.28 ± 0.09	-0.35 ± 0.11

and Lubin (1979). In the comparisons, dipole-only fits are quoted for experiments not claiming significant quadrupole terms. The dipole-only fit should equal the dipole part of a dipole-plus-quadrupole fit if there is no significant quadrupole power and if there are small correlations between dipole and quadrupole terms. A comparison of Tables 5.9 and 6.1 shows that the dipole-only and the dipole-plus-quadrupole fits agree quite well for this experiment. Although Fixsen *et al.* (1983) found no evidence for a quadrupole, their T_z and Q_1 components are rather highly correlated (correlation coefficient $= -0.70$). The dipole result quoted in Table 6.2 for Fixsen *et al.* has been reconstructed from their dipole-plus-quadrupole fit by inverting the solution vector and error matrix to recover their original data vector and moment matrix, and solving again for only the dipole terms. The Fixsen *et al.* dipole-only result in Table 6.2 has a declination 3 degrees more positive and a right ascension 1 degree greater than their dipole-plus-quadrupole fit. The Fixsen *et al.* dipole direction agrees very well with this measurement.

Comparison of this experiment to Boughn *et al.* (1981) is complicated by the quadrupole anisotropy claimed by Boughn *et al.* If the quadrupole were real, then dipole-only fits with incomplete sky coverage would be corrupted by quadrupole power and would not represent the true dipole anisotropy. Boughn *et al.* give data for the dipole and four of the five quadrupole components, with T_z (fitted) $= T_z$ (true) $+ 1.1\ Q_1$. Their quoted dipole anisotropy, given

Table 6.2. Comparison of dipole anisotropies measured by different experiments. Magnitude is mK thermodynamic temperature for $T_{CBR} = 2.7$ K.

Reference	Frequency (GHz)	Magnitude (mK)	Right Ascension (degrees)	(hours)	Declination (degrees)
This work	90	3.48 ± 0.24	168.8 ± 1.9	11.3 ± 0.1	-5.7 ± 1.8
Fixsen *et al.*,[1] 1983	24.5	3.12 ± 0.18	169.2 ± 1.6	11.3 ± 0.1	-5.3 ± 1.6
Smoot and Lubin, 1979	33	3.1 ± 0.4	172 ± 6	11.5 ± 0.4	9.6 ± 6
Boughn *et al.*,[2] 1981	19, 24.8, 31.4, 46	3.78 ± 0.30	174 ± 3	11.6 ± 0.2	-12 ± 5

[1]Dipole-only fit reconstructed according to Section 6.1.1. Table 1.1 entry is dipole portion of combined dipole-plus-quadrupole fit.

[2]Dipole portion of combined dipole-plus-quadrupole fit.

in Table 6.2, is the dipole part of the combined dipole-plus-quadrupole fit, with the fitted T_z converted to true T_x by removing the Q_1 term of 0.38 ± 0.26 reported by Smoot and Lubin (1979). If the same dipole-only reduction used on Fixsen *et al.* is applied to Boughn *et al.*, the dipole declination becomes -6 ± 5 degrees and the right ascension decreases to 171 degrees (11.4 hours), which is in better agreement with this experiment. The magnitude of the reconstructed Boughn *et al.* dipole-only fit is 3.74 ± 0.30 mK.

6.1.2 Magnitude

The magnitudes of the dipole results are qualitatively in agreement. They are reported in Table 6.2 as thermodynamic temperature anisotropies assuming a CBR 2.7 K blackbody spectrum. A simple weighted average of their amplitudes is 3.33 ± 0.12 mK. The χ^2 value of the entries with respect to this average is 4.38 for 3 DOF, with over half coming from the Boughn *et al.* measurement. The confidence level is 22%. In order to account for the direction as well in the average, a quantitative analysis would need to generate an effective total moment matrix

and data vector for the four experiments, solve the combined system, and compute the total χ^2 for consistently-defined solutions (e.g. all dipole-only fits). This procedure is strictly valid for experiments dominated by statistical error, which is not the case for the ones here. Since the dipole directions are in agreement, with the largest discrepancy being in the least-heavily weighted measurement, averaging the magnitudes is an adequate indication of the consistency of the experiments under the assumption of a 2.7 K blackbody spectrum.

Since the magnitude of a motion-induced antenna temperature anisotropy depends upon the CBR spectral shape as well as its intensity, it is necessary to model the CBR spectrum in order to quantitatively compare the results. Conversely, by assuming that the *antenna temperature* anisotropies measured at different frequencies represent the same *thermodynamic* anisotropy, information about the CBR spectrum can be obtained (Danese and De Zotti, 1981; Lubin *et al.*, 1983c).

For an arbitrary CBR spectrum, the anisotropy at frequency ν is given in terms of the velocity β, the intensity spectral index α, and the CBR antenna temperature T_a by substituting equation (1.5) into equation (1.4b):

$$\Delta T_a = (3-\alpha)\beta T_a. \tag{6.1}$$

For a blackbody CBR with frequency-independent thermodynamic anisotropy ΔT, the parameters α and T_a are related, so anisotropy measurements at different frequencies unambiguously scale according to equation (1.6b):

$$\Delta T_a(\nu) = \frac{x^2 e^x}{(e^x-1)^2}\Delta T, \qquad \text{with } x = \frac{h\nu}{kT}. \tag{1.6b}$$

6.1.3 CBR Spectral Distortion

Distortions from a CBR blackbody spectrum will induce corresponding departures from (1.6b). In particular, near 90 GHz the measurement of Woody and Richards (1979) suggests

a higher temperature and a flatter spectral index than those for blackbody spectra. For the Woody-Richards data at 90 GHz, T is $3.18^{+0.25}_{-0.19}$ K with corresponding antenna temperature $T_a \simeq 1.47 \pm 0.2$ K. The spectral index is $\simeq 0.88$, but values between 0.85 and 1.15 cannot be ruled out. At 90 GHz, a 2.7 K blackbody has $T_a = 1.09$ and $\alpha = 1.00$; a 3 K blackbody has $T_a = 1.34$ and $\alpha = 1.11$. Both the flux and the spectral slope of the Woody-Richards spectrum would enhance the 90 GHz anisotropy relative to what would be expected by scaling lower frequency observations using (1.6b).

The consistency between this experiment and lower frequency observations can be examined with respect to different models for the CBR spectra, paralleling the analysis of Lubin *et al.*, (1983c). Given the CBR antenna temperature T_a and temperature spectral index α at frequency ν, the velocity vector $\vec{\beta}_i$ corresponding to each dipole anisotropy observation $\Delta\vec{T}_i$ can be calculated from (6.1). If the two observations $\vec{\beta}_i$ truly represent the same $\vec{\beta}$, then the scalar product

$$S^2 = (\vec{\beta}_1 - \vec{\beta}_2)^T \{\mathbf{M}_1^{-1} + \mathbf{M}_2^{-1}\}^{-1} (\vec{\beta}_1 - \vec{\beta}_2), \tag{6.2}$$

where the $\mathbf{M}_i^{-1}$ are the error matrices corresponding to the $\vec{\beta}_i$, has a χ^2 distribution for three degrees of freedom (Appendix D). A measure of the consistency of two measurements, then, is the probability that χ^2 for 3 DOF would exceed the S^2 value calculated here.

Dipole magnitude measurements do not yet have precision sufficient to place very stringent limits on the CBR spectrum. Furthermore, the variation in measurements made at the same frequency suggests that systematic errors may be underestimated. Nevertheless, an analysis comparing the 90 GHz experiment to the Fixsen *et al.* result at 24.5 GHz has been carried out. Of the experiments in Table 6.2, these two are the most recent and the most precise. They are also the only ones with in-flight calibration. The dipole anisotropy results for this experiment and for Fixsen *et al.* are given in antenna temperature in Table 6.3, along with the expected anisotropies $(3 - \alpha)\beta T_a$ corresponding to different CBR models.

Table 6.3. Measured dipole anisotropy at 90 and 24.5 GHz, along with predicted anisotropies for different CBR spectra.

	This experiment	Fixsen *et al.*
Frequency (GHz)	90	24.5
Measured Components in mK antenna temperature:		
$\Delta T_{a,x}$	-2.76 ± 0.19	-3.01 ± 0.17
$\Delta T_{a,y}$	0.54 ± 0.11	0.58 ± 0.09
$\Delta T_{a,z}$	-0.28 ± 0.09	-0.28 ± 0.08
Magnitude		
ΔT_a	2.83 ± 0.19	3.07 ± 0.17
Expected Magnitude $(3 - \alpha)T_a\beta$ in K antenna temperature:		
2.7 K Blackbody	2.191β	2.658β
3.0 K Blackbody	2.531β	2.962β
Woody-Richards	3.116β	—

Table 6.4 gives the S^2 values and corresponding confidence levels for the comparisons. CBR blackbody spectra with temperatures of 2.7 K and 3.0 K are examined, as are spectra which are 2.7 K or 3.0 K blackbodies at 24.5 GHz but are consistent with the Woody-Richards data at 90 GHz. For completeness, CBR spectra which are a 2.7 K blackbody at one of the two frequencies and 3.0 K blackbody at the other are also examined. Table 6.4 shows that a 2.7 K thermal CBR spectra is quite consistent with the 24.5 GHz and 90 GHz anisotropy measurements. Neither the quality of the anisotropy observations, nor the precision with which the anisotropy expected from the Woody-Richards spectrum can be calculated, allows significant conclusions to be made concerning the Woody-Richards data.

For a blackbody CBR, the cases $T_{CBR} = 2.7$ K and $T_{CBR} = 3.0$ K can be generalized to arbitrary temperature. Figure 6.1 presents, as a function of T_{CBR}, the confidence levels at which

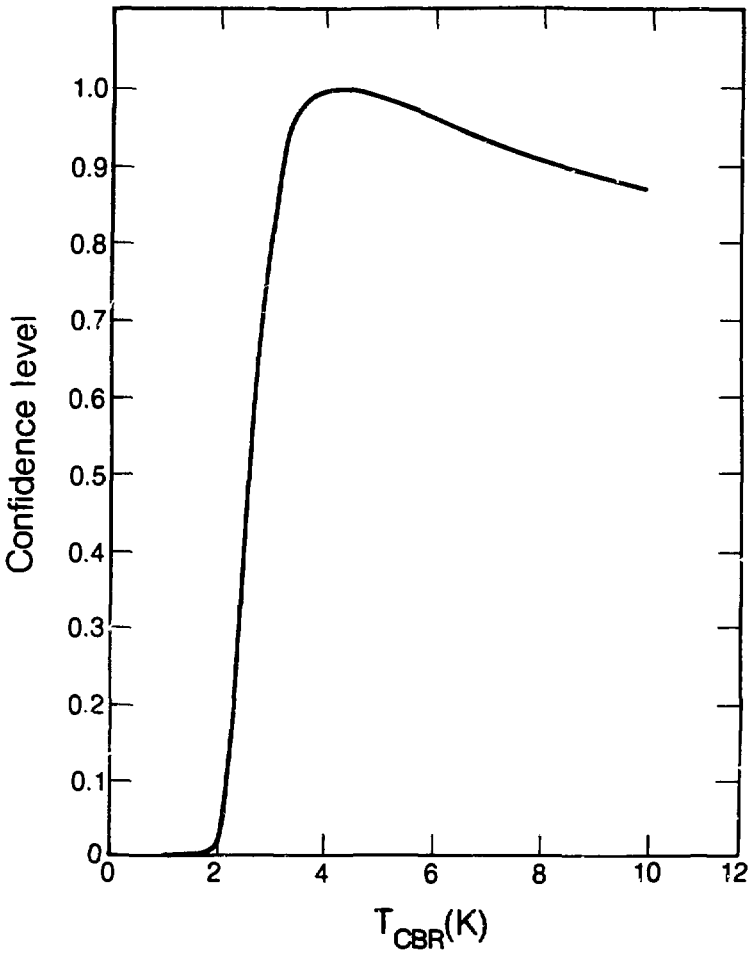

Figure 6.1. Confidence levels at which 24.5 GHz and 90 GHz dipole observations agree with each other assuming a blackbody CBR, as a function of CBR temperature

Table 6.4. Confidence levels at which anisotropies measured at 24.5 GHz and at 90 GHz are consistent with each other assuming various CBR spectra.

CBR Spectrum at 24.5 GHz	CBR Spectrum at 90 GHz	Value of S^2	Confidence Level
2.7 K	3.0 K	0.2027	97.7%
3.0 K	3.0 K	0.9133	82.2%
2.7 K	2.7 K	1.9048	59.2%
3.0 K	W–R	2.7451	43.3%
3.0 K	2.7 K	6.9941	7.2%
2.7 K	W–R	9.0799	2.8%

the 24.5 GHz and the 90 GHz anisotropy measurements are consistent with each other assuming a blackbody CBR spectrum. It shows that no CBR temperature less than 2.19 K is consistent with the observations at higher than a 10% confidence level, putting a 90% confidence-level minimum of 2.2 K on the CBR temperature. Unlike most other conclusions about the CBR spectrum derivable from anisotropy measurements, this CBR temperature lower limit is quite firm. Physically, a blackbody CBR spectrum cooler than the minimum would have so much less power at 90 GHz than at lower frequencies that that the measured 90 GHz anisotropy would imply enormous anisotropy at 24.5 GHz.

No upper bound can be placed on the CBR temperature from this analysis alone. Since the difference between the expected anisotropies at 24.5 GHz and 90 GHz for high temperature blackbody spectra is so small, all sufficiently high temperatures are equivalent and cannot be distinguished by the two measurements. The confidence level vs. CBR temperature plot in Figure 6.1 has a very broad maximum, showing that a CBR temperature of 4.2 K is formally most consistent with the 24.5 GHz and the 90 GHz observations but also indicating that an infinitely hot CBR is consistent with the ratio of those measurements at a confidence level of 79%.

6.1.4 Solar Velocity

The dipole anisotropy is most readily interpreted as a measure of velocity relative to a comoving frame of reference. Since dipole anisotropy generated by other mechanisms would in general be accompanied by higher order anisotropies, the lack of quadrupole moment (see next section) supports the peculiar velocity origin of the dipole, as does the dipole's frequency independence.

Assuming a 2.7 K blackbody CBR, the dipole anisotropy measured by this experiment represents a solar velocity of 387 ± 25 km/sec towards right ascension $\alpha = 11.^h3 \pm 0.^h1$ and declination $\delta = -6° \pm 2°$ (galactic latitude $b = 50° \pm 2°$ and longitude $l = 266° \pm 3°$). The weighted average magnitude found in Section 6.1.1 corresponds to a velocity of 367 ± 13 km/sec in essentially the same direction. This velocity can be decomposed into several components at different levels of aggregation. The sun moves relative to the "local standard of rest" defined by nearby stars, the closest of which are on the order of parsecs away. This ensemble participates in galactic rotation about the galactic center some 10 kiloparsecs distant. The Milky Way galaxy is a member of the "Local Group", a collection of ten to twenty primarily dwarf galaxies within about a megaparsec. The entire Local Group belongs to yet a larger structure, the equally prosaically-named Local Supercluster, which is dominated by the Virgo cluster of galaxies some 15 Mpc away. Only the vector sum of all the relative velocities is measured by the CBR anisotropy.

Referring the sun's velocity $\vec{v}_\odot$ to the centroid of the Local Group by subtracting their relative motion $\vec{v}_\odot - \vec{v}_{LG}$ of 308 km/sec towards $(\alpha, \delta) = (22.^h9, 51°)$; $(l, b) = (105°, -7°)$ (Yahil *et al.*, 1977), the 90 GHz anisotropy shows the Local Group to have a velocity of 640 km/sec towards $(\alpha, \delta) = (11.^h1, -26°)$. This direction is 43° away from the Virgo cluster centered at $(\alpha, \delta) = (12.^h4, 13°)$ (Sandage and Tammann, 1976), yielding a velocity component towards Virgo of 470 ± 30 km/sec.

Studies of Local Group velocity relative to objects closer to us than the last scatterers of the CBR are required in order to decouple currents within the Local Supercluster from large-scale bulk flow of the entire supercluster. Several such studies have been made, but they are not all in agreement. They are reviewed in a recent paper by Davis and Peebles (1983b) which discusses anisotropy in the Hubble flow.

Anisotropy in the hard x-ray background has been observed which is not inconsistent with the CBR measurements. However, the sources of the x-ray background are not well understood. If the x-rays are produced at the present epoch, then an increased concentration of sources in the local supercluster proportional to the observed enhancement of optical luminosity could account for most of the x-ray asymmetry (Boldt, 1981).

Three studies of solar velocity derived from anisotropy in galactic red shifts are compared with the velocity relative to the CBR in Table 6.5. Using luminosity as a distance indicator, Rubin *et al.* (1976) examine spiral galaxies outside the Local Supercluster and assign the sun a peculiar velocity of 600 km/sec towards $(\alpha, \delta) = (2.^h1, 53°)$. The Sc galaxies studied have recession velocities between 3500 and 6500 km/sec, corresponding to distances of $35h^{-1}$ to $65h^{-1}$ Mpc with the Hubble constant H_0 expressed as $100h$ km sec^{-1} Mpc^{-1}. Removing the solar velocity, Rubin *et al.* find their data is consistent with isotropic Hubble expansion.

Table 6.5. Solar peculiar velocity relative to the CBR and to three samples of galaxies. Velocity direction is given both in celestial and galactic coordinates. No correction for solar motion within the galaxy and Local Group has been applied.

	This Work	Rubin *et al.*, 1976	De Vaucouleurs *et al.*, 1981	Hart and Davies, 1982
Magnitude: (km/sec)	387 ± 25	600 ± 125	306 ± 40	310 ± 55
α: (hours)	11.3 ± 0.1	2.1 ± 1.3	17 ± 7	12.3 ± 0.7
δ: (deg)	-6 ± 2	53 ± 11	84 ± 7	30 ± 12
l: (deg)	266 ± 3	135 ± 12	117 ± 12	192 ± 60
b: (deg)	50 ± 2	-8 ± 12	30 ± 7	83 ± 12

De Vaucouleurs *et al.* (1981) study the motion of 300 spiral galaxies receding at between 200 and 2900 km/sec. Assuming isotropic expansion and fitting observed galactic red shifts to the dipole anisotropy which would be generated by a solar peculiar velocity, they find a relative motion between the sun and the galaxy sample of 306 ± 40 km/sec towards $(\alpha, \delta) = (17^h, 84°)$. Galactic distances are determined by the Tully-Fisher method of comparing the observed optical luminosity to the absolute luminosity determined from the hydrogen 21-cm linewidth. Solutions excluding galaxies near the supergalactic center are consistent with the results of the full sample.

Hart and Davies (1982) analyze a sample of 78 Sbc galaxies receding at between 1000 and 5000 km/sec. The redshift of the hydrogen 21-cm line provides velocity data, and the line's

integrated flux, parameterized by its width, serves as a standard candle. Their result for solar peculiar velocity is 310 ± 55 km/sec towards $(\alpha, \delta) = (12.^h3, 30°)$.

The angular resolutions of the peculiar velocity studies relative to galaxies are on the order of ten degrees. None of the velocity directions in Table 6.5 agree to that level. The Hart and Davies velocity is closest to the velocity implied by the CBR anisotropy at 90 GHz, with a difference between the directions of two velocities of 39 degrees. Discrepancies in magnitude among the studies make the disagreement even worse. After being referred to the centroid of the Local Group, the Hart and Davies finding shows the Local Group to have a velocity 463 km/sec directed 26° from Virgo. The direction of this velocity is 17° from the Local Group's velocity with respect to the CBR, with the difference vector between Hart and Davies velocity and the CBR velocity having magnitude 242 km/sec. Inconsistency among Local Group velocities relative to different sets of galaxies would imply either relative motion between the galaxy sets or else underestimated systematic error. Disagreement between galactic studies and CBR anisotropy similarly implies either large-scale motion of the supercluster as a whole, or systematic error.

The Rubin result, in particular, is highly controversial. Fall and Jones (1976) argue that inhomogeneity in the distribution of galaxies (inferred from the known inhomogenous distribution of clusters), together with use of a narrow magnitude window, can cause selection of galaxies in an isotropically expanding universe which will display an anisotropic velocity distribution. Hart and Davies (1982) repeat their 21-cm line analyses on those Sc galaxies in the Rubin *et al.* sample which have recession velocities between 1000 and 5000 km/sec, augmented by some additional southern hemisphere galaxies. They find a result consistent with their own (Hart and Davies) Sbc galaxy sample and inconsistent with the Rubin *et al.* findings. In their review, Davis and Peebles (1983b) lend greater credence to studies such as Hart and Davies (1982) which employ an additional distance-independent variable such as 21-cm linewidth.

The similarity of the Hart and Davies velocity to the CBR-derived motion suggests

that the dipole anisotropy could be caused be motion within the supercluster, although with a several standard-deviation discrepancy remaining this conclusion is certainly not required. In supercluster internal-flow models, the component of velocity towards Virgo results from the gravitational attraction of the enhanced matter distribution in that direction, while a transverse component could arise from a lack of spherical symmetry in the supercluster collapse (Davis and Peebles, 1983b). The Local Group velocity with respect to the CBR need not point directly towards Virgo if this is the case. Alternatively, discrepancy between the CBR anisotropy and the Milky Way motion within the supercluster implies either an intrinsic component to the CBR anisotropy or the existence of bulk flow on larger scales than have yet been examined.

6.2 Quadrupole Anisotropy

This experiment detects no significant quadrupolar anisotropy in the CBR. It does not reproduce the "quadrupole-like" anisotropy of Fabbri *et al.*, (1980) nor the significant quadrupole terms reported in Boughn *et al.* (1981), which were attributed in a later publication by that group to ground radiation and excess radiometer noise synchronous with gondola rotation (Fixsen *et al.*, 1983). Table 6.6 presents the quadrupole coefficients reported by the experiments whose dipole terms are given in Table 6.2. In the absence of true quadrupolar anisotropy, an experiment with statistical errors and correlations equivalent to those of this work would measure quadrupole power equal to or greater than that detected here 45.5% of the time.

A limit on quadrupolar anisotropy can be quantified by defining the average quadrupole temperature

$$T_{Q,rms} = \left(\frac{1}{4\pi} \int_{4\pi} T_Q^2(\Omega)\, d\Omega \right)^{\frac{1}{2}}, \quad \text{where} \tag{6.3a}$$

$$T_Q(\Omega) = \sum_{i=1}^{5} Q_i q_i(\Omega) \tag{6.3b}$$

Table 6.6. Comparison of quadrupole coefficients in mK thermodynamic temperature.

Reference	Q_1	Q_2	Q_3	Q_4	Q_5
This work	—	0.15 ± 0.14	0.16 ± 0.14	-0.06 ± 0.10	0.09 ± 0.09
Fixsen *et al.*, 1983	0.15 ± 0.08	0.15 ± 0.11	0.14 ± 0.07	0.06 ± 0.11	-0.01 ± 0.07
Smoot and Lubin, 1979	0.38 ± 0.26	-0.34 ± 0.29	0.02 ± 0.24	-0.11 ± 0.16	0.06 ± 0.20
Boughn *et al.*, 1981	—	0.28 ± 0.22	0.13 ± 0.21	-0.31 ± 0.15	-0.54 ± 0.14

and the quadrupole basis functions q_i are defined in Table 5.1. Evaluating the angular integrals,

$$T^2_{Q,rms} = \frac{1}{5}Q_1^2 + \frac{4}{15}\sum_{i=2}^{5} Q_i^2. \tag{6.4}$$

Since this experiment is insensitive to Q_1, only four of the five quadrupole degrees of freedom can be examined. Assuming that the universe is not aligned with the earth's north pole, the total quadrupole power ($\sim T^2_{Q,rms}$) can be bounded by augmenting the limit on power in the measured Q_2 to Q_5 terms by an additional 25%.

Neglecting Q_1, the value $T_{Q,rms}$ in antenna temperature for the 90 GHz data is 0.10 mK. Monte Carlo calculations show that ninety percent of the time, a radiometer having the statistical errors and correlations of this experiment and observing a true quadrupole anisotropy given by the Q_2 to Q_5 values in Table 5.9 will have $T_{Q,rms} \leq 0.20$ mK. The calculation involves diagonalizing the error matrix to express the quadrupole coefficients in uncorrelated basis functions, jittering each transformed coefficient with noise values taken from a distribution whose variance is the coefficient's mean-square error, histogramming the resultant values of $T_{Q,rms}$, and finding that value marking the 90^{th} percentile of $T_{Q,rms}$ distribution. Multiplying this value by the square root of 1.25 to account for the missing Q_1 power gives a 90% confidence-level upper limit of 0.22 mK antenna temperature. The equivalent thermodynamic rms quadrupole upper limit for

$T_{CBR} = 2.7K$ is 0.27 mK, or a part in 10^{-4} of the CBR.

The rms dipole anisotropy is given by an analogous formula,

$$T_{D,rms} = \left(\frac{1}{4\pi}\int_{4\pi} T_D^2(\Omega)\, d\Omega\right)^{\frac{1}{2}},$$
$$= \left(\frac{(T_x^2 + T_y^2 + T_z^2)}{3}\right)^{\frac{1}{2}}. \qquad (6.5)$$

Substituting the values in Table 5.9, the rms dipole anisotropy $T_{D,rms} = 2.01$ mK (thermodynamic), yielding $(T_{Q,rms}/T_{D,rms}) \leq 0.13$ at 90% confidence.

Fixsen *et al.* (1983) present values for all five quadrupole components, so $T_{Q,rms}$ can be computed directly from equation (6.4). The 90% confidence-level limit calculated from those components by the Monte Carlo technique described above is 0.23 mK (thermodynamic). An alternative method of comparing the quadrupole limit of Fixsen *et al.* to this work is to re-solve the Fixsen *et al.* system without a Q_1 term. Following the identical procedure on the re-determined error and solution parameters as was performed on the 90 GHz results gives a 90% confidence-level quadrupole temperature limit of 0.22 mK for the Fixsen *et al.* data. The 90% limit actually quoted by Fixsen *et al.* is 0.19 mK, but the method of analysis is not explicitly described.

6.3 Galactic Emission

Fits to the 90 GHz data are unaffected by inclusion of the galactic plane (Table 5.6), showing that the data are not severely contaminated by dust emission. At 24.5 GHz, where galactic emission is much stronger, failure to model or exclude the galaxy changes the fitted T_y component of the dipole by almost 0.5 mK (Fixsen, 1983). Fits of the 90 GHz data to galactic models are consistent with dust emission, averaged over the region within five degrees of the galactic plane and convolved with the radiometer beam, of about 0.5 mK. This value represents

a global fit to the entire observed sky; dust emission in any specific region can be estimated only to the extent that the overall galactic model correctly reflects the dust distribution in that region.

6.4 Summary

The dipole anisotropy measured by this experiment at 90 GHz has an antenna temperature magnitude of 2.82 ± 0.19 mK directed towards 11.3 ± 0.1 hours right ascension and -5.7 ± 1.8 degrees declination. The direction is consistent with lower frequency observations, and the dipole magnitude measured by this experiment relative to that observed at 24.5 GHz by Fixsen *et al.*is consistent with motion through a 2.7 K blackbody CBR. With that CBR spectrum, the thermodynamic anisotropy measured by this experiment has magnitude 3.48 ± 0.24 mK, corresponding to a solar velocity of 387 ± 25 km/sec. Correcting for the sun's motion relative to the Local Group gives a Local Group peculiar velocity of 640 km/sec directed 43° from the Virgo cluster. Motion solely within the Local Supercluster may be responsible for the entire CBR anisotropy, but the discrepancies among studies of Local Group velocity with respect to other galaxies make it impossible to draw this conclusion with high confidence.

This experiment finds no evidence for higher order anisotropy in the cosmic background radiation. The universe appears isotropic on the largest directly accessible scale, with a 90% confidence-level upper limit of 10^{-4} on the CBR quadrupole anisotropy. Since galactic emission at 90 GHz is low, it is not a significant source of systematic error in this experiment.

In the two decades since the discovery of the CBR, our understanding of the nature and history of our universe has increased tremendously. Angular anisotropy measurements, having improved in sensitivity by more than three orders of magnitude, characterize a dipole anisotropy which still has no detectable frequency dependence or higher order moments.

Appendix A

Relativistic Flux Transformation

A.1 Phase Space Density

The intensity I_ν (ergs cm^{-2} sec^{-1} Hz^{-1} str^{-1}) of a radiation field at frequency ν can be shown to be proportional to ν^3 times the Lorentz-invariant photon phase space densityη. Intensity transformation from one reference frame to another is therefore given in terms of the transformation of ν^3.

Phase space density invariance follows from the invariance of the phase space volume element — if a group of particles occupies the same amount of phase space volume in all frames, all observers will measure the same value for the density. As shown below, although the different observers measure different physical space volumes $dx\,dy\,dz$ and momentum space volumes $dp_x\,dp_y\,dp_z$, the product $d^3\mathbf{x}\,d^3\mathbf{x}$ is invariant.

Consider first a group of massive particles occupying physical space element $dx\,dy\,dz$ in its rest frame. An observer moving along the x direction with velocity $\beta = v/c$ measures transverse dimensions dy' and dz' equal to the rest-frame dimensions dy and dz. Her measurement of the longitudinal dimension dx' is made at a single instant in her own frame, so $dt' = 0$ and $dx = \gamma(dx' - \beta c dt') = \gamma\,dx'$. Her Lorentz-contracted length measurement, multiplied by

the unchanged area, gives a physical-space volume compressed by a factor of γ relative to the particle rest frame: $dp_x\,dp_y\,dp_z = d^3\vec{x}' = d^3\vec{x}/\gamma$.

Since kinetic energy is quadratic in momentum, the spread in particle energy $c^2 dp_0$ vanishes (i.e. is of order dp_x^2) in the particle rest frame. The moving observer measures $c\,dp_x' = \gamma(c\,dp_x - \beta c^2 dp_0) = \gamma\,c\,dp_x$. Again, the transverse measurements $dp_y' = dp_y$ and $dp_z' = dp_z$ are unaffected, so $d^3\vec{x}' = \gamma\,d^3\vec{x}$. The total phase space volume is seen to be

$$\begin{aligned} d^3\vec{x}'\,d^3\vec{x}' &= \left(\frac{d^3\vec{x}}{\gamma}\right)(\gamma\,d^3\vec{x}) \\ &= d^3\vec{x}\,d^3\vec{x} \end{aligned} \tag{A.1}$$

for all observers. In the limit as rest mass approaches zero, the identity remains valid, establishing phase space volume and density invariance for photons as well.

A.2 Intensity

Given a photon phase space density, the intensity measured by an observer will depend on the energy of each detected photon and the range of solid angle subtended by the photons. The energy per photon is proportional to ν, and the amount of solid angle per unit momentum space goes as ν^{-2} ($d^3\vec{x} = p^2\,dp\,d\Omega$, with $p = |\vec{x}| \sim \nu$ for photons, so $d\Omega/d^3\vec{x} \sim \nu^{-2}$). Therefore, the intensity is proportional to ν^3 times the phase space density η. (Misner *et. al.*, 1973, p. 589) The ratio I_ν/ν^3, proportional to η, is Lorentz invariant and can be used to transform radiation intensity:

$$\begin{aligned} \frac{I_\nu'}{I_\nu} &= \left(\frac{\nu'}{\nu}\right)^3 \\ I_\nu' &= \left(\frac{\nu'}{\nu}\right)^3 I_\nu. \end{aligned} \tag{A.2}$$

If a radiation field is isotropic in the unprimed frame, this relation gives its angular dependence for an observer in the moving primed frame. Let θ be the angle in the unprimed

frame between the direction from which the photon arrives and the moving observer's velocity. A photon having angular frequency ω and wavevector $\vec{k}$ in the isotropic frame (with $\omega = |\vec{k}|c$) will have

$$\begin{aligned}\omega' &= \gamma(\omega - \beta c k_x) \\ &= \gamma\omega(1 + \beta\cos\theta) \\ &= \omega(1 + \beta\cos\theta) \text{for} \beta << 1,\end{aligned}$$

so for small velocity, $(\nu'/\nu) = (\omega'/\omega) = (1 + \beta\cos\theta)$.

For a spectrum having logarithmic frequency derivative $(\partial \log I \,/\, \partial \log \nu)$ equal to α near frequency ν_0 such that $I \sim I_0(\nu/\nu_0)^\alpha$, we obtain

$$\begin{aligned}I_{\nu'}(\theta') &= \left(\frac{\nu'}{\nu}\right)^3 I_0\left(\frac{\nu}{\nu_0}\right)^\alpha \\ &= I_0\left(\frac{\nu'}{\nu}\right)^3\left(\frac{\nu}{\nu'}\right)^\alpha\left(\frac{\nu'}{\nu_0}\right)^\alpha \\ &= \left[I_0\left(\frac{\nu'}{\nu_0}\right)^\alpha\right]\left(\frac{\nu'}{\nu}\right)^{3-\alpha} \\ &= I_0'(1 + (3 - \alpha)\beta\cos\theta) \qquad (1.4a)\end{aligned}$$

for observations at a fixed frequency ν' in the primed frame.

Appendix B

Radiometers

A microwave radiometer measures electromagnetic energy. The simplest type of radiometer measures the total power collected by an antenna. Added to the amplified input power is noise generated within the radiometer itself, so the output of a *total power radiometer* is a signal proportional to the sum of the incident and the internally-generated power. The *system noise temperature* characterizes noise generated by the radiometer. It is the antenna temperature of a source which, when observed by a noise-free radiometer, produces the same output as the actual radiometer would yield looking at source at zero K.

The radiometer output will fluctuate due to statistical variation in the noise power and to fluctuations in the radiometer gain. These output fluctuations determine the resolution with which the input antenna temperature can be measured. For a total power radiometer with system noise temperature T_{sys}, the RMS output fluctuations when observing incident antenna temperature T_a are

$$\Delta T = (T_{sys} + T_a)\left\{\left(\frac{1}{B\tau}\right) + \left(\frac{\Delta G}{G}\right)^2\right\}^{\frac{1}{2}}, \qquad (B.1)$$

where B is the bandwidth, τ is the net integration time, and $(\Delta G/G)$ is the RMS fractional change in receiver gain over the integration time. ΔT, also known as the *figure of merit*, is the input signal which can be detected with a signal-to-noise ratio of unity.

To minimize the effect of gain fluctuations, a *differential radiometer* (Dicke, 1945) switches between the source and a reference and yields an output proportional to their difference in emitted power. If the source has exactly the same intensity as the reference, the radiometer is *balanced* and has no net output. Gain variations on time scales longer than the switching period in a balanced differential radiometer are cancelled out. If there is an *offset temperature* between source and reference, gain variations will cause some fluctuation in the output. However, these fluctuations will be suppressed by a factor of $T_{\text{offset}}/(T_{\text{sys}} + T_{\text{R}})$ with respect to those of a total power radiometer. If the reference temperature cannot be adjusted to eliminate the offset, the effect of gain variation on the offset can be minimized by interchanging source and reference, as is done when the 90 GHz radiometer rotates 180°. This interchange introduces a further level of differencing, which nulls out gain variations on time scales longer than the interchange period.

The sensitivity of a differential radiometer having offset temperature T_{offset} is given by the expression

$$\Delta T = \left[\left\{ (T_{\text{sys}} + T_{\text{R}}) \left(\frac{K}{\sqrt{B\tau}} \right) \right\}^2 + \left\{ (T_{\text{sys}} + T_{\text{R}}) \left(\frac{\Delta G}{G} \right)_{\substack{\text{switch} \\ \text{period}}} \right\}^2 + \left\{ (T_{\text{offset}}) \left(\frac{\Delta G}{G} \right)_{\substack{\text{inter-} \\ \text{change}}} \right\}^2 + \left\{ (\Delta T_{\text{offset}}) \right\}^2 \right]^{\frac{1}{2}} \qquad (B.2)$$

where the constant K depends on how the synchronous switching and detection are done, and ΔT_{offset} includes drift in the reference temperature. The $(\Delta G/G)$ terms are RMS fractional gain variations over the indicated time periods. If source and reference are not interchanged, the "interchange period" becomes the total observation time.

For an ideal differential radiometer, the factor K in equation (B.2) is 2. The factor comes about because a differential radiometer observes the source only half the time, spending the remainder on the reference. The statistical fluctuations in source and reference measurements are greater by $\sqrt{2}$ than those of a total power radiometer spending the entire time on one or the

other, and fluctuations in differencing the source and reference intensities are another factor of $\sqrt{2}$ greater than those in either measurement alone. In practice, K also depends on details of the synchronous filter design such as the number of harmonics of the switching frequency which are transmitted by stages downstream of the switch. Since the 90 GHz lockin back end passes several switching-frequency harmonics, its value for K should be very close to 2.

Two references which discuss descriptions and properties of different types of microwave radiometers are Evans and McLeish, 1977, and Kraus, 1966.

Appendix C

Calibration

C.1 Primary Calibration

Primary calibration of the radiometer in the laboratory and on the flight line is done by positioning a blackbody target removed from a container of liquid nitrogen in one beam and an ambient-temperature blackbody in the other. The targets are held in position until the lockin output stabilizes, and the output is recorded before the liquid nitrogen target starts to warm up (typically within 10 to 15 seconds). Averaging the difference in outputs between measurements with the targets interchanged removes any offset. The ambient temperature is measured either by a thermometer or by temperature sensors on the radiometer. Ambient temperature uncertainty of two degrees yields a calibration error of one percent and is not a significant source of error. The liquid nitrogen target is assumed to be at the temperature of boiling liquid nitrogen at sea level. The slope of the boiling curve is 0.085 K per percent change in pressure, so atmospheric pressure variations of up to 5% introduce less than 0.5 K uncertainty in the liquid nitrogen temperature. Measurements at 10 GHz and 33 GHz show that an Eccosorb[1] target dipped in and then removed from liquid nitrogen has an antenna temperature within ± 0.3 K of a target

[1]Emerson and Cummings microwave absorber model AN-73

immersed in liquid nitrogen (S. Friedman and G. De Amici, private communication). For the purposes of this experiment, the 77.4 K boiling point T_{LN} of liquid nitrogen is taken to be 77 K.

The primary calibration value, averaged over widely separated measurements in a three-week period before the November flight, was 67.2 Kelvins per lockin output volt with an RMS scatter of 2.6%. No changes affecting system gain were made following that flight, and a corresponding average of calibrations done over two weeks before the April flight was 67.6 K/volt with a scatter of 2.1%. The weighted average of November and April values, 67.5 K/volt, was used in analyzing data from both flights. Calibrations done on the flight line immediately before each flight (66.9 ± 0.9 K/volt in November and 67.6 ± 0.5 K/volt in April; both included in the averages above) were consistent with the laboratory measurements.

C.2 Corrections

Two corrections were made to the calibration constant to yield the value used on flight data. The first of these accounts for the change in lockin gain by a factor of 101.1 ± 0.2 between the scales used for ground calibration (range ± 338 K) and for flight (range ± 3.34 K). The second corrects for slight saturation of the detector diode. If the diode characteristic (voltage out vs. power in) becomes non-linear, its slope is a function of the incident power level. The above calibration procedure measures the slope of the chord connecting the operating points for ambient temperature and liquid nitrogen temperature loads. For a non-linear characteristic, this slope is not necessarily the same as the slope of the characteristic at the operating point maintained by the system when viewing the 3 K CBR.

To determine the slope at the actual operating point, power in the radiometer IF band was attenuated by varying amounts and detected. The resultant diode output voltages were fitted to a cubic polynomial in incident power level. This polynomial was used to find analytically the ratio of the slope of the chord connecting the ambient and LN calibration points to the slope

of the characteristic at the high-altitude operating point. The calibration constant measured with ambient and *LN* loads, in Kelvins per volt, is inversely proportional to the slope of the $(T_{amb} - T_{LN})$ chord. Multiplying the measured calibration constant by the ratio found above, and correcting for the change in gain, yields the calibration constant used at the flight operating point.

The diode characteristic calculated for the 90 GHz radiometer showed a 4.5% non-linearity for an ambient temperature load, a 3.4% non-linearity for liquid nitrogen, and 1.3% for the operating point at altitude. The ratio of the slope of the $(T_{amb} - T_{LN})$ chord to the slope at the operating point is 0.96 with an estimated error of ± 0.02. Using this factor and correcting for the difference in gain, the conversion at altitude from lockin output volts to milliKelvins antenna temperature is 641 mK/volt.

C.3 Stability of and Error in Calibration

C.3.1 Pop-up Calibrator - Description

The in-flight pop-up calibrator is a piece of iron-loaded epoxy microwave absorber 0.35 cm^2 in area, mounted with a temperature sensor on the end of a brass rod 0.31 cm wide. When raised into the beam, the target subtends a solid angle of 1.9×10^{-4} steradians at a distance from the horn of 43 ± 3 cm, depending upon where on the horn the measurement is taken. At that distance, not quite into the far-field of the antenna (which is distances greater than $\pi a^2/\lambda$ from a circular horn of radius a, or 60 cm for this experiment), the horn's gain pattern is not known accurately enough to use the target as an absolute calibration. As a first approximation, the ratio of the target solid angle to the antenna's integrated gain-weighted solid angle of 0.021 ± 0.003 steradians predicts that the target will generate an antenna temperature equal to 0.009 ± 0.0013 of its physical temperature.

Seen from the horn and convolved over the same antenna pattern, the support rod subtends 0.0214 ± 0.015 of the beam, or 2.4 times that of the target. The emissivity of brass is on the order of 10^{-3}, so emission from the arm is negligible. As long as the variations in radiation scattered off the arm are small compared to the target emission, a constant calibrator signal will indicate a stable system calibration. If the scattered contribution is variable, changes in calibrator signal amplitude provide an upper bound to system variability.

C.3.2 Pop-up Calibrator Flight Observations

In-flight calibrator observations were made every 27 minutes during the November, 1981 flight. Each was analyzed by taking the average of six 2.1-second integration periods during which the calibrator was centered in the direct beam, and subtracting the mean of equivalent sections before and after the calibration. The statistical uncertainty of each observation was 0.006 K or 0.2% . During the data-taking portion of the flight, the calibrator temperature varied by 1.4% between 219 and 222 K.

The mean magnitude of the calibrator signals for the November flight was 2.26 K, with an RMS scatter of 0.014 K or 0.6%. The predicted calibrator emission is 1.96 ± 0.33 K, with the error representing uncertainty in the target's true gain-weighted solid angle. Besides emission, power scattered off the arm may have contributed to the signal as well. The total signal generated by the calibrator therefore consisted of emission from the target plus scattering off the arm, minus the sky emission which was blocked by the target and arm. At altitude, the arm sees primarily sky or reflected sky with an angle-independent intensity. Except for power scattered from the earth, radiation scattered by the arm has the same antenna temperature as radiation blocked by the arm. Groundshields prevented most earth emission from reaching the arm and target, although the arm and target could see the horizon in the November, 1981 configuration. During the 13 seconds that the target was in the beam each calibration, the gondola rotated through 85

degrees. Therefore, horizon power scattered by the calibrator was averaged over a large area.

C.3.3 Pop-up Calibrator Ground Observations

Measurements done on the ground could not unambiguously resolve the level to which scattering influenced the in-flight calibrations. The sky was rarely stable enough to permit observations of the pop-up target on the ground using the flight sensitivity. In addition, the $\sec\theta$ variation of atmospheric temperature with zenith angle, along with the presence of warm objects of various sizes on the horizon, cause scattered power in ground observations to have in general a much different temperature than the atmospheric emission which is blocked by the arm. Therefore, scattering should have a greater effect on the calibrator signal in ground observations than it would at altitude.

Crude observations made before the first flight in July showed that the arm without target generated a signal about one-third of that generated by the arm plus target. This result indicates that on the ground, the difference in power scattered minus power obstructed by the arm alone is half the correspouding difference in power emitted minus power obstructed by the target.

Observations of the pop-up calibrator on the ground were made using the flight sensitivity on three widely spaced instances in Texas and in Berkeley. The calibrator physical temperature, sky temperature, and measured signal are shown in Table C.1 along with the predicted signal assuming the target solid angle given earlier. The sol'd angle is highly uncertain but is the same for all observations, so the differences in measured signal give an indication of the variability of the scattered contribution. Calibration constants measured at the time of each observation, along with saturation corrections appropriate to the sky temperature, have been used.

The large variation in signal (from 1.22 to 1.74 times the predicted value) probably

Table C.1. Pop-up calibrator ground observations.

Date	Calibrator Temperature	Sky Temperature	Predicted Signal	Measured Signal
11/82	309 ± 1	48 ± 1	2.35 ± 0.40	3.14 ± 0.07
11/82	307 ± 1	71 ± 2	2.12 ± 0.35	2.59 ± 0.04
4/83	283 ± 1	46 ± 2	2.12 ± 0.35	3.68 ± 0.05

represents the differences in effective horizon temperature. The last measurement above, for example, was made in a parking lot surrounded by trees and buildings.

C.3.4 Error in Calibration Constant

In any given measurement of the system calibration, the temperature difference $T_{amb} - T_{LN}$ and the radiometer output voltage can both be measured to better than one percent. The dominant source of uncertainty is variation arising from system drifts and differences in the beam filling factor for the liquid-nitrogen temperature. Scatter among widely-spaced calibration measurements gives an estimate of these effects and is under 3% for this system. Any systematic change in system behavior between ground and flight, or from flight to flight, will also directly contribute to calibration error. To account for possible systematic errors, the absolute calibration uncertainty has been taken to be $\pm 6\%$ with a relative flight-to-flight uncertainty of 3% . The pop-up in-flight calibrator was replaced with a full-beam calibrator following the April, 1982 flight; unfortunately data with observations of this calibrator at altitude were lost, along with the gondola, during the November, 1982 flight in Brazil.

Appendix D

Linear Least Squares Estimation

D.1 Best Fit Solution

One of the most widely used techniques of modeling noisy data is least squares fitting, which determines the set of model parameters minimizing the squared residuals between the data and the model. Consider a collection of data measurements y_i, each having uncertainty σ_i. The measurements are to be modeled by a function of the p to-be-determined parameters a_j and the l independent coordinates for each observation $\vec{x}_i = (x_i^1, \ldots, x_i^l)$.

Attributing all discrepancy between the best-fit model and the data to noise, we have

$$y_i = W(a_j, \vec{x}_i) + \epsilon_i, \tag{D.1}$$

with the ϵ_i representing randomly distributed noise values. To determine the best-fit parameters a_j, define

$$\chi^2 = \sum_i \left(\frac{\epsilon_i}{\sigma_i}\right)^2 = \sum_i \frac{(y_i - W(a_j, \vec{x}_i))^2}{\sigma_i^2}. \tag{D.2}$$

Minimize χ^2 with respect to the a_j:

$$\frac{\partial \chi^2}{\partial a_j} = 0 \quad \Rightarrow \quad \sum_i \frac{y_i}{\sigma_i^2} \frac{\partial W}{\partial a_j}\bigg|_{\vec{x}_i} = \sum_i \frac{W(a_j, \vec{x}_i)}{\sigma_i^2} \frac{\partial W}{\partial a_j}\bigg|_{\vec{x}_i}. \tag{D.3}$$

For models in which W is linear in the parameters a_j, the *normal equations* defined by (D.3) simplify considerably. If $W = \sum_j a_j f_j(\vec{x}_i)$, where the f_j are a set of basis functions, then $\partial W/\partial a_j = f_j$, and the normal equations become

$$\sum_i \frac{y_i f_j(\vec{x}_i)}{\sigma_i^2} = \sum_i \sum_k \frac{a_k f_j(\vec{x}_i) f_k(\vec{x}_i)}{\sigma_i^2}.$$

Define the *data vector* components D_j to be $\sum_i y_i f_j(\vec{x}_i)/\sigma_i^2$ and the *moment matrix* $\mathbf{M}_{jk} = \sum_i f_j(\vec{x}_i) f_k(\vec{x}_i)/\sigma_i^2$. The normal equations become $D_j = \sum_k \mathbf{M}_{jk} \hat{a}_k$, and the best-fit solution parameters a_k are found by inverting the system to give $\hat{a}_k = \sum_j \mathbf{M}_{jk}^{-1} D_j$.

D.2 Uncertainty in Fitted Parameters

The fitted $\hat{a}_k$ have an uncertainty due to noise in the observations y_i. The $\hat{a}_k$ are also in general *correlated* in that independent errors ϵ_i in the observations y_i will result in changes δa_k to the solution vector components which are not independent. The uncertainties and correlations in the $\hat{a}_k$ can be analyzed by examining the expected value of the covariances $< \delta\hat{a}_j \, \delta\hat{a}_k >$ over independent sets of measurement noise values ϵ_i:

$$\begin{aligned} \delta a_j &= \sum_i \frac{\partial a_j}{\partial \epsilon_i} \delta\epsilon_i; \\ < \delta a_j \, \delta a_k > &= < \sum_i \frac{\partial a_j}{\partial \epsilon_i} \delta\epsilon_i \sum_l \frac{\partial a_k}{\partial \epsilon_l} \delta\epsilon_l > . \end{aligned} \tag{D.4}$$

Now since $a_j = \sum_m \mathbf{M}_{jm}^{-1} D_m$, we have

$$\begin{aligned} \frac{\partial a_j}{\partial \epsilon_i} &= \sum_m \mathbf{M}_{jm}^{-1} \frac{\partial D_m}{\partial \epsilon_i}, \\ &= \sum_m \mathbf{M}_{jm}^{-1} \frac{f_m(\vec{x}_i)}{\sigma_i^2} \end{aligned}$$

upon substituting equation (D.1) into the definition of the data vector. The covariances are

$$< \delta a_j \, \delta a_k > = \sum_{i,l} \sum_{m,n} \mathbf{M}^{-1}_{jm} \frac{f_m(\vec{x}_i)}{\sigma_i^2} \mathbf{M}^{-1}_{kn} \frac{f_n(\vec{x}_i)}{\sigma_l^2} < \delta\epsilon_i \, \delta\epsilon_l >,$$

and since the $\delta\epsilon_i$ are independent,

$$< \delta\epsilon_i \, \delta\epsilon_l > = \begin{cases} \sigma_i^2, & \text{if } i = l; \\ 0, & \text{otherwise.} \end{cases} \qquad (D.5)$$

Therefore

$$\begin{aligned} < \delta a_j \, \delta a_k > &= \sum_{m,n} \mathbf{M}^{-1}_{jm} \sum_i \frac{f_m(\vec{x}_i) f_n(\vec{x}_i)}{\sigma_i^4} \sigma_i^2 \, \mathbf{M}^{-1}_{kn} \\ &= \sum_{m,n} \mathbf{M}^{-1}_{jm} \, \mathbf{M}_{mn} \, \mathbf{M}^{-1}_{kn} \\ &= \mathbf{M}^{-1}_{jk}. \end{aligned} \qquad (D.6)$$

Hence the components of $\mathbf{M}^{-1}$, called the *error matrix*, give the solution parameter covariances, and the diagonal terms $\mathbf{M}^{-1}_{jj}$ are the mean squared errors of the components a_j of the solution vector. The correlations between solution parameters are often expressed as a normalized *correlation matrix* $\mathbf{C}$:

$$\mathbf{C}_{jk} = \frac{\mathbf{M}^{-1}_{jk}}{\sqrt{\mathbf{M}^{-1}_{jj} \mathbf{M}^{-1}_{kk}}}.$$

D.3 Comparison of Independent Solutions

Consider parameter estimates $\hat{a}^1$ and $\hat{a}^2$ fitted to independent data sets. To determine whether the fits are consistent with each other, examine the difference vector $\Delta\hat{a} = \hat{a}^1 - \hat{a}^2$. If the two fits are solutions for the same observables, each component of this difference should have an expectation value of zero, with the expected covariance $<(\hat{a}^1 - \hat{a}^2)_j \, (\hat{a}^1 - \hat{a}^2)_k>$ given by $<(\hat{a}^1_j \hat{a}^1_k)> - <(\hat{a}^1_j \hat{a}^2_k)> - <(\hat{a}^2_j \hat{a}^1_k)> + <(\hat{a}^2_j \hat{a}^2_k)>$. The first and fourth terms, from (D.6), are $\mathbf{M}^{1}_{jk}{}^{-1} + \mathbf{M}^{2}_{jk}{}^{-1}$. The cross terms are zero since the errors $\delta\epsilon^1_i$ and $\delta\epsilon^2_l$, which appear

in the expression equivalent to (D.5) generalized to more than one data set, are independent: $< \delta\epsilon_i^1 \, \delta\epsilon_l^2 >= 0$ even for $i = l$. Therefore,

$$< (\hat{a}^1 - \hat{a}^2)_j (\hat{a}^1 - \hat{a}^2)_k > = \mathbf{M}^1_{jk}{}^{-1} + \mathbf{M}^2_{jk}{}^{-1}. \tag{D.7}$$

If the total error matrix $\mathbf{M}^{-1}$ is defined such that $\mathbf{M}^{-1} = \mathbf{M}^{1\,-1} + \mathbf{M}^{2\,-1}$, the covariance matrix of the p elements of the difference vector $\Delta\hat{a}$ is $\mathbf{M}^{-1}$, and the scalar product

$$S^2 = \Delta\hat{a}^T \mathbf{M} \Delta\hat{a}$$

will be distributed as χ^2 for p degrees of freedom. This distribution is easiest to see in a set of basis functions for which $\mathbf{M}$ is diagonal. $\mathbf{M}$ is symmetric, so such a diagonalization can always be found. Since $\mathbf{M}^{-1}$ is the covariance matrix for the $\Delta\hat{a}_j$, which are uncorrelated in this basis, the elements $\mathbf{M}^{-1}_{jk}$ are equal to $< \Delta\hat{a}_j^2 >$ for $j = k$ and 0 for $j \neq k$. Therefore, $\mathbf{M}_{jk} = < \Delta\hat{a}_j^2 >^{-1}$, and

$$S^2 = \sum_{j=1}^{p} \frac{\Delta\hat{a}_j^2}{< \Delta\hat{a}_j^2 >}$$

which can be seen to have a χ^2_p distribution. The confidence level at which two independent solutions $\hat{a}^1$ and $\hat{a}^2$ agree is the confidence level of drawing S^2 from a χ^2 distribution for p degrees of freedom.

Two useful references discussing estimation and other statistical techniques are Bevington (1969) and Martin (1971).

Appendix E

Generation of Sky Maps

E.1 Normal Equations

A map is a representation of the sky intensity distribution using a set of basis functions f_j which have magnitude unity over a particular area or *pixel* in the sky, are zero elsewhere, and do not overlap. Relevant normal equations are derived by minimizing the following expression for χ^2 (c.f. equation (D.2)):

$$\chi^2 = \sum_i \left(\frac{\Delta T_i - (T_{Ai} - T_{Bi})}{\sigma_i} \right)^2 \qquad (E.1)$$

where T_{Ai} and T_{Bi} are the temperatures of the pixel that radiometer beams A and B observe to give the i^{th} difference ΔT_i.

By adding all measurements linking a particular pair of pixels j and k to give an average temperature difference $\overline{\Delta T}_{jk} \pm \sigma_{jk}$, the sum over data points can be replaced by a double sum over pixels. Let $\{j\}$ be the set of pixels connected to pixel j by at least one observation ΔT_i. (Note that j is not a member of $\{j\}$, since no observation has pixel j in both beams.) An equivalent formulation of χ^2 becomes

$$\chi^2 = \sum_j \sum_{k \in \{j\}} \left(\frac{\overline{\Delta T}_{jk} - (T_j - T_k)}{\sigma_{jk}} \right)^2 . \qquad (E.2)$$

The normal equations are given by setting $(\partial\chi^2/\partial T_{j'}) = 0$ for all $T_{j'}$:

$$\frac{\partial\chi^2}{\partial T_{j'}} = -2\sum_j \sum_{k\in\{j\}} \left(\frac{\overline{\Delta T}_{jk} - (T_j - T_k)}{\sigma^2_{jk}}\right)(\delta^{j'}_j - \delta^{j'}_k)$$

$$= 0, \quad \text{with } \delta^{j'}_j = \begin{cases} 1, & \text{if } j = j'; \\ 0, & \text{otherwise.} \end{cases}$$

We can eliminate the sum over j and replace $\overline{\Delta T}_{kj}$ with $-\overline{\Delta T}_{jk}$ to get

$$\sum_{k\in\{j'\}} \left(\frac{T_{j'} - T_k - \overline{\Delta T}_{j'k}}{\sigma^2_{j'k}}\right) = 0.$$

Expanding, and replacing j' with j,

$$T_j \sum_{k\in\{j\}} \frac{1}{\sigma^2_{jk}} - \sum_{k\in\{j\}} \frac{T_k}{\sigma^2_{jk}} - \sum_{k\in\{j\}} \frac{\overline{\Delta T}_{jk}}{\sigma^2_{jk}} = 0. \tag{E.3}$$

By defining

$$a_{jj} = \sum_{l\in\{j\}} \frac{1}{\sigma^2_{jl}} \tag{E.4a}$$

$$a_{jk} = -\frac{1}{\sigma^2_{jk}}, k \in \{j\}; \quad = 0, \text{ otherwise} \tag{E.4b}$$

$$b_j = \sum_{l\in\{j\}} \frac{\overline{\Delta T}_{jl}}{\sigma^2_{jl}}, \tag{E.4c}$$

equation (E.3) reduces to

$$\sum_k a_{jk} T_k = b_j. \tag{E.5}$$

The coefficients a_{jk} are non-zero only for pixel pairs connected by measurements ΔT_i. If one radiometer beam is viewing a given pixel, there are only a very limited number of pixels which may be observed by the other beam. Therefore, the great majority of the a_{jk} are zero, and the system (E.5) is quite sparse. Since $\overline{\Delta T}_{jk} = -\overline{\Delta T}_{kj}$, implying $\sum_j b_j = 0$, the equations (E.5 are not linearly independent. The data, all differential measurements, are insensitive to the addition of a constant to all pixels. An additional constraint equation is required to remove this degeneracy.

E.2 Gauss-Seidel Sparse Matrix Inversion

The Gauss-Seidel technique is an iterative method of inverting a system of linear equations. The system is expressed as a set of equations in which each unknown parameter is given as a function of the others. If initial estimates are made for all parameters, an updated value for the first unknown can be calculated. This new value, along with the initial guesses for all the other parameters, can be substituted into the equation for the second unknown, and so on. For each unknown, the most recently found estimates of the other parameters are used. Iterations will converge to a solution of the original system for sufficiently well-behaved systems.

Consider the system described by (E.4) and (E.5) above. Each parameter T_k is given in terms of the others by

$$T_k = \frac{b_k}{a_{kk}} - \sum_{j \neq k} \frac{a_{jk}}{a_{kk}} T_j. \qquad (E.6)$$

Here a_{kk} represents the k^{th} diagonal element, rather than the trace, of the coefficient matrix. Initial estimates of all the T_j are made, enabling updated values to be computed. As new values are found, they immediately replace the previous estimates which had been used in the right-hand-sides of the equations (E.6).

Iterative procedures such as the Gauss-Seidel method are particularly suited for sparse matrix inversion since the number of stored parameters and computations required depends on the number of non-zero coefficients. Given the fixed radiometer geometry, and the sky coverage having a single zenith declination, a particular pixel could be linked by measurements to pixels in at most two other regions of the sky. The number of non-zero matrix elements in the normal equations is therefore approximately proportional to the number of observed pixels, rather than to the square of the number of pixels as would be the case if the pixels were more generally interconnected.

A sufficient, but not necessary, condition for the iterations to converge is that the

diagonal coefficient of each row of the coefficient matrix dominate the other terms in the row (Carnahan *et al.*, 1969):

$$|a_{jj}| > \sum_{k \neq j} |a_{jk}|. \tag{E.7}$$

If the coefficients are sufficiently well distributed (there being no $p \times q$ submatrix of the $n \times n$ coefficient matrix which is a zero and for which $p + q = n$), the strict inequality can be relaxed to

$$|a_{jj}| \geq \sum_{k \neq j} |a_{jk}| \tag{E.8}$$

provided that (E.7) holds for at least one row (Hildebrand, 1956).

From the definitions in (E.4) we have $a_{jj} \equiv \sum_{k \neq j} |a_{jk}|$, not satisfying equations (E.7). Nevertheless, the map iterations converge quite rapidly for the 90 GHz data. The RMS and the maximum change in the pixel values per iteration, taken over the entire map, decrease monotonically as iterations increase. Consecutive changes in the value of any given pixel do not necessarily decrease unless that pixel is the one having the greatest change. To provide the required additional constraint, the weighted mean of all pixel values was set to zero by addition of a constant to all pixels. The maps presented in Chapter 5 were the results of 200 iterations; the RMS change in pixel value during the 200^{th} iteration was on the order of tenths of μK per pixel.

E.3 Jacobi Iterative Method

The Jacobi method, like the Gauss-Seidel approach, computes updated parameter values from initial guesses or prior iteration results. However, the new values computed during an iteration are not used in later computations within the same iteration. Instead, all parameter values are updated simultaneously at the end of each iteration. The Jacobi method generally does not converge as fast as the Gauss-Seidel technique and was not used for the 90 GHz maps.

E.4 Non-Iterative Method

A *differential map* can be constructed from differential data without iteration by summing, with the appropriate sign, all observations of a pixel by either radiometer beam. If the radiometer output values ΔT_i are the differences $T_{Ai} - T_{Bi}$, with T_{Ai} and T_{Bi} defined as above, then the differential map value for pixel j is $\sum_i \Delta T_i \delta_j^A - \sum_i \Delta T_i \delta_j^B$. This value is equivalent to the result of one iteration of the Jacobi method if an initial value of zero is selected for all pixels.

Appendix F

Radiometer Parts

Component	Manufacturer and Model
Antenna	Petersen Instruments, 90 GHz scalar feed horn
Batteries, gelled-electrolyte lead-acid	Powersonic PS-1260, PS-1265
Coupler, directional ring	Custom Microwave Components, WR-10 waveguide, gold-plated
Dewar, cryogenic	Infrared Laboratories helium-cooled dewar, Model HD-3(8)
Diode, detector	Hewlett Packard 8472B
Diode, mixer	Chip 2P8-500, GaAs, supplied by Roger Mattauch, Department of Electrical Engineering, University of Virginia, Charlottesville, VA
FETs, GaAs, for cooled IF amp	Mitsubishi MGF-1412
Filter, bandpass	K & L Microwave Model 8B120-1375/295-OP/O
Filter, notch	K & L Microwave Model F6N45-1485.5/40-O/O
Gunn diode oscillator	Central Microwave CMF1210AE
IF amp, uncooled	Miteq Model AM-5A-0420
Mixer block	Custom Microwave Components, WR-10 waveguide, gold-plated
Motor, chopper	Globe/TRW DC Motor 319A101-8
Motor, rotor	Globe/TRW DC Motor 5A561-1
Magnetometers, fluxgate	Develco Model 9200C
Magnetometers, Hall effect	F. W. Bell Model BH-850
Tape logger	Datel Intersil LPS-16
Temperature sensors	Analog Devices AD590
Termination, waveguide	Baytron Co., Model 3R-50

Appendix G

Azimuthal Anisotropy Coefficients

For a differential radiometer having two beams at zenith angle θ which are 180° apart in azimuth, the dependence of the output signal on azimuth angle can be used to find the dipole and quadrupole terms of a spherical-harmonic expansion of the CBR anisotropy.

In terms of the basis functions defined in Table 5.1, the CBR temperature in the direction of unit vector $\hat{n} = (n_x, n_y, n_z)$ towards (right ascension, declination) $= (\alpha, \delta)$ is given by

$$T_{CBR} = T_0 + \sum_{i=x,y,z} T_i\, n_i + \sum_{i=1,5} Q_i\, q_i(\hat{n}). \qquad (G.1)$$

The temperature difference measured between radiometer beams A and B is

$$\Delta T = T_{\hat{n}_A} - T_{\hat{n}_B} = \sum_{i=x,y,z} T_i \cdot \{n_{Ai} - n_{Bi}\} + \sum_{i=1}^{5} Q_i \cdot \{q_i(\hat{n}_A) - q_i(\hat{n}_B)\}. \qquad (G.2)$$

Expressing the functions n_i and $q_i(\hat{n})$ of the direction vector components in terms of the radiometer zenith right ascension α and declination δ, the beam zenith angles θ, and the azimuth angle ϕ of the direct beam A, the temperature difference in (G.2) becomes

$$
\begin{aligned}
\Delta T \;=\; & \Big(\;\; 2\sin\theta \;\; \sin\delta \;\; \cos\alpha\cos\phi \;+\; 2\sin\theta \;\; \sin\alpha\sin\phi \Big)\; T_x \\
+\; & \Big(\;\; 2\sin\theta \;\; \sin\delta \;\; \sin\alpha\cos\phi \;-\; 2\sin\theta \;\; \cos\alpha\sin\phi \Big)\; T_y \\
+\; & \Big(-2\sin\theta \;\; \cos\delta \;\; \cos\phi \Big)\; T_z \\
+\; & \Big(-\tfrac{3}{2}\sin 2\theta \sin 2\delta \;\; \cos\phi \Big)\; Q_1 \\
+\; & \Big(-2\sin 2\theta\cos 2\delta\cos\alpha\cos\phi \;+\; 2\sin 2\theta\sin\delta\sin\alpha\sin\phi \Big)\; Q_2 \\
+\; & \Big(-2\sin 2\theta\cos 2\delta\sin\alpha\cos\phi \;-\; 2\sin 2\theta\sin\delta\cos\alpha\sin\varphi \Big)\; Q_3 \\
+\; & \Big(\;\; \sin 2\theta\sin 2\delta\cos 2\alpha\cos\phi \;+\; 2\sin 2\theta\cos\delta\sin 2\alpha\sin\phi \Big)\; Q_4 \\
+\; & \Big(\;\; \sin 2\theta\sin 2\delta\sin 2\alpha\cos\phi \;-\; 2\sin 2\theta\cos\delta\cos 2\alpha\sin\phi \Big)\; Q_5.
\end{aligned}
\tag{G.3}
$$

In (G.3), the coefficients of $\cos\phi$ and $\sin\phi$ depend on the to-be-found multipole parameters $\{a_j\} = \{T_x, T_y, T_z, Q_1, Q_2, Q_3, Q_4, Q_5\}$ as well on as the sky position and the radiometer geometry. Grouping together the $\cos\phi$ and $\sin\phi$ coefficients, we can define functions W^c and W^s by $\Delta T(\phi) = W^c(\{a_j\}, \alpha, \delta, \theta)\cos\phi + W^s(\{a_j\}, \alpha, \delta, \theta)\sin\phi$. Dividing the radiometer data into intervals and fitting the data over each interval i to an analogous expression $\Delta T(\phi) = (\Delta T_i^c \pm \sigma_i^c)\cos\phi + (\Delta T_i^s \pm \sigma_i^s)\sin\phi$, we can form an expression for χ^2:

$$
\chi^2\{a_j\} = \sum_i \left[\frac{W^c(\{a_j\}, \alpha_i, \delta_i, \theta) - \Delta T_i^c}{\sigma_i^c}\right]^2 + \left[\frac{W^s(\{a_j\}, \alpha_i, \delta_i, \theta) - \Delta T_i^s}{\sigma_i^s}\right]^2. \tag{G.4}
$$

In (G.4), α_i and δ_i are the average right ascension and declination over the i^{th} interval. Minimizing χ^2 with respect to the anisotropy dipole and quadrupole parameters $\{a_j\}$, as described in Appendix D, determines the best-fit parameters.

Acknowledgements

When I first got into the ballooning business, I was promptly regaled with legend and lore about various ballooning disasters of the past, including the "Lost in the Badlands" saga, the "Lost at Sea" story, and the "Great Airport Disaster". I did not expect at the time to make my own contribution to that body of technical literature. Nevertheless, I am grateful for the opportunity I've had to do this experiment and to work with those who have made it possible. Without Phil Lubin's direction, dedication, motivation, and insight, this project would quite literally never have gotten off the ground. The experiment has been the fruition of some of Phil's ideas, and the breeding ground for many more. A special note of thanks is due Phil's family, who endured his absence on more than a few field expeditions, and who probably thought he was done with grad student hours when he finished his own PhD. George Smoot has taught me about data, about analysis, and about what they have to do with science. He has also tried to instill in me some sense of organization. Hal Dougherty's precision mechanical design and construction was as attractive as it was functional. John Gibson designed and built most of the electronics. Both Hal and John were tolerant beyond the call of duty when yesterday's rush job became today's re-design. Tap Lum and the U.C. Radio Astromony Laboratory were invaluable in building the GaAs FET amplifiers; George Jackson and Armi Meuti also helped build the experiment.

I especially thank Rainer Weiss and David Wilkinson for flying, at no insignificant risk to their own experiments, the 90 GHz radiometer on their gondolas. The skilled staff of the

National Scientific Balloon Facility in Palestine, TX has been competent and friendly. I also thank the Instituto de Pesqnisas Espacias in Saõ José dos Campos, SP, Brasil, for their assistance and cooperation. Ted Stubbs and the K-Division Analog Tape Center at Lawrence Livermore National Laboratory helped digitize the Brazilian telemetry data. This thesis has been typeset with the TeX typesetting program (Knuth, 1979).

I've enjoyed working with my fellow students: Scott "i-before-e" Friedman, Chris W-i-t-"e"-as-in-Edward-"b"-as-in-Baker-s-k-y Witebsky, Giovanni De Amici, Phil Melese, and Steve Levin. I also thank two of my predecessors at Princeton and Berkeley, Mark Gorenstein and Brian Corey, for their exceptionally helpful theses. Faye Mitschang and Nancy Gusack have done an admirable job keeping the Astrophysics group running; Nancy also was the one other person in Berkeley who would keep Silver Spring, MD, from going plural. The resources of the Lawrence Berkeley Laboratory have been much appreciated and utilized, as has been the support of the U.C. Berkeley Space Sciences Laboratory. This work has been supported in part by NASA and the Department of Energy. California Space Institute (CalSpace) funding has also been particularly appreciated. The Fannie and John Hertz Foundation has supported me throughout my graduate stay at Berkeley.

References

Alpher, R. and Herman, R., *Phys. Rev.* **75**, 1089 (1949).

Barber, Mark, *IEEE Trans. Microwave Theory Tech.* **MTT-15**, 629 (1967).

Barrow, J. D. amd Matzner, R. A., *Mon. Not. R. Astr. Soc.* **181**, 719 (1977).

Barrow, J. D. and Turner, M. S., *Nature* **298**, 801 (1982).

Bevington, P. R., *Data Reduction and Error Analysis for the Physical Sciences*, McGraw-Hill, New York (1969).

Boldt, E., *Comments Astrophys.* **9**, 97 (1981).

Bondi, H. and Gold, T., *Mon. Not. R. Astr. Soc.* **108**, 252 (1948).

Born, M. and Wolf, E., *Principles of Optics*, Pergamon Press (1964).

Boughn, S. P., Fram, D. M., Partridge, R. B., *Ap. J.* **165**, 439 (1971).

Boughn, S. P., Cheng, E. S., and Wilkinson, D. T., *Ap. J. Lett.* **243**, L113 (1981).

Carnahan, B., Luther, H. A., and Wilkes, J. O., *Applied Numerical Methods*, Wiley, New York (1969).

Carr, B. J. and Rees, M. J., *Nature* **278**, 605 (1979).

Carter, "Large Number Coincidences and the Anthropic Principle in Cosmology," in *Confrontation of Cosmological Theories with Observational Data*, edited by M. S. Longair, I.A.U. Symposium No. 63, D. Reidel, Dordrecht, Holland (1974).

Ceccarelli, C., Dall'Oglio, G., Melchiorri, F., and Pietranera, L., *Ap. J.* **260**, 484 (1982).

Cheng, E. S., Saulson, P. R., Wilkinson, D. T., and Corey, B. E., *Ap. J. Lett.* **232**, L139 (1979).

Cole, A., Court, A., and Kantor, A. J., "Model Atmospheres," in *Handbook of Geophysics and Space Environment*, edited by S. L. Valley, Office of Aerospace Research, USAF, Cambridge Research Lab (1965).

Collins, C. B. and Hawking, S. W., *Ap. J.* **180**, 317 (1973a).

Collins, C. B. and Hawking, S. W., *Mon. Not. R. Astr. Soc.* **162**, 307 (1973b).

Conklin, E. K., *Nature* **222**, 971 (1969).

Corey, B., Ph.D. Thesis, Princeton University (1978).

Danese, L. and De Zotti, G., *Astron. Astrophys.* **94**, L33 (1981).

Davis, Jesse, *NRAO Electronics Division Internal Report* **177** (1977).

Davis, M. and Peebles, P. J. E., *Ap. J.* **267**, 465 (1983a).

Davis, M. and Peebles, P. J. E., *Ann. Rev. Astron. Astrophys.* **21**, 109 (1983b).

De Vaucouleurs, G., Peters, W., Bottinelli, L., Gougenheim, L., Paturel, G., *Ap. J.* **248**, 408 (1981).

Dicke, R. H., *Nature* **192**, 440 (1961).

Dicke, R. H., *Rev. Sci. Inst.* **17**, 268 (1946).

Dicke, R. H., Beringer, R., Kyhl, R. L., and Vane, A. B., *Phys. Rev.* **70**, 340 (1946).

Dicke, R. H., Peebles, P. J. E., Roll, P. G., and Wilkinson, D. W., *Ap. J.* **142**, 414 (1965).

Evans, G. and McLeish, C., *RF Radiometer Handbook*, Artech House, Inc., Dedham, MA. (1977).

Fabbri, R., Guidi, I., Melchiorri, F. and Natale, V., *Phys. Rev. Lett.* **44**, 1563 (1980).

Fabbri, R., Guidi, I., and Natale, V., *Ap. J.* **257**, 17 (1982).

Fall, S. M., and Jones, B. J. T., *Nature* **262**, 467 (1976).

Fixsen, D., Ph.D. Thesis, Princeton University (1982).

Fixsen, D. J., Cheng, E. S. and Wilkinson, D. T., *Phys. Rev. Lett.* **50**, 620 (1983).

Gamow, G., *Phys. Rev.* 70, 572 (1946).

Gamow, G., *Phys. Rev.* **74**, 505 (1948).

Gorenstein, M. V., Ph.D. Thesis, University of California, Berkeley (1978).

Gorenstein, M. V. and Smoot, G. F., *Ap. J.* **244**, 361 (1981).

Guth, A. H., *Phys. Rev. D* **23**, 347 (1981).

Harrison, E. R., *Cosmology, the Science of the Universe*, Cambridge Universe Press, Cambridge (1981).

Hart, L., and Davies, R. D., *Nature* **297**, 191 (1982).

Hawking, S., *Mon. Not. R. Astr. Soc.* **142**, 129 (1969).

Haslam, C. G. T., Salter, C. J., Stoffel, H., and Wilson, W. E., *Astron. Astrophys. Suppl. Ser.* **47**, 1 (1982).

Heiles, C., and Habing, H. J., *Astron. Astrophys Suppl. Ser.* **14**, 1 (1974).

Hildebrand, F. B., *Introduction to Numerical Analysis*, McGraw-Hill, New York (1956).

Hogan, C. J., Kaiser, N., and Rees, M. J., *Phil. Trans. R. Soc. Lond. A* **307**, 97 (1982).

Janssen, M., Bednarczyk, S., Gulkis, S., Marlin, H., and Smoot, G. F., *IEEE Trans. Ant. Prop.* **AP-27**, 551 (1979).

Kerr, Anthony, *IEEE Trans. Microwave Theory Tech.* **MTT-23**, 781 (1975).

Knuth, Donald E., *TeX and Metafont, New Directions in Typesetting*, Digital Press, Bedford, MA (1979).

Kraus, John D., *Radio Astronomy*, McGraw-Hill, New York (1966).

Kuhn, Thomas S., *The Copernican Revolution, Planetary Astronomy in the Development of Western Thought*, Harvard University Press, Cambridge, MA (1957).

Kuhn, Thomas S., *The Structure of Scientific Revolutions*, Chicago University Press, Chicago (1970).

Lubin, P., Epstein, G., and Smoot, G., *Phys. Rev. Lett.* **50**, 616 (1983a).

Lubin, P., Melese, P., and Smoot, G., *Ap. J. Lett.* **273**, L51 (1983b).

Lubin, P., Fixsen, D., Cheng, E., and Epstein, G., *Ap. J.*, submitted (1983c).

Martin, B. R., *Statistics for Physicists*, Academic Press, London (1971).

Mather, J. and Kelsall, T., *Physica Scripta* **21**, 671 (1980).

Meyer, D. H. and Jura, M., *Ap. J. Lett.* **276**, L1 (1984).

Mie, E., *Zeitschrift für Astrophysik* **6**, 1 (1933).

Misner, C. W., Thorne, K. S., and Wheeler, J. A., *Gravitation*, W. H. Freeman and Co., San Francisco (1973).

Misner, C. W., *Ap. J.* **151**, 431 (1968).

NASA Goddard Space Flight Center, *Interim Study Report for Cosmic Background Explorer*, p. 48 (1977).

Owens, D. K., Muehlner, D. J., and Weiss, R., *Ap. J.* **231**, 702 (1979).

Partridge, R. P. and Wilkinson, D. T., *Phys. Rev. Lett.* **18**, 557 (1967).

Peebles, P. J. E., *Physical Cosmology*, Princeton University Press, Princeton, New Jersey (1971).

Peebles, P. J. E. and Wilkinson, D. T., *Phys. Rev.* **174**, 2168 (1968).

Peebles, P. J. E., *Ap. J. Lett.* **243**, L119 (1981).

Peebles, P. J. E., *Ap. J.* **259**, 442 (1982).

Penzias, A. A. and Wilson, R. W., *Ap. J.* **142**, 419 (1965).

Press, W. H., "Galaxies may be Single Particle Fluctuations from an Early False-Vacuum Era," in *Cosmology and Particles*, edited by Audouze *et al.*, Proceedings of the Sixteenth Rencontre de Moriond Astrophysics Meeting, Singapore National Printers (1981).

Rees, M. J., *Ap. J. Lett.* **153**, L1 (1968).

Roll, P. G. and Wilkinson, D. W., *Phys. Rev. Lett.* **16**, 405 (1966).

Roll, P. G. and Wilkinson, D. W., *Annals of Physics* **44**, 289 (1967).

Rubin, V. C., Thonnard, N., Ford, W. K., and Roberts, M. S., *Astron. Jour.* **81**, 719 (1976).

Sandage, A. and Tammann, G. A., *Ap. J. Lett.* **207**, L1 (1976).

Sciama, Dennis, *Modern Cosmology*, Cambridge, University Press, Cambridge (1971).

Silk, Joseph, *The Big Bang*, W. H. Freeman and Company, San Francisco (1980).

Silk, J. and Wilson, M., *Ap. J. Lett.* **244**, L37 (1981).

Smoot, G., De Amici, G., Friedman, S., Witebsky, C., Mandolesi, R., Partridge, B., Sironi, G., Danese, L., and De Zotti, G., *Phys. Rev. Lett.* **51**, 1099 (1983).

Smoot, G. F., Gorenstein, M. V., and Muller, R. A., *Phys. Rev. Lett.* **39**, 898 (1977).

Smoot, G. F. and Lubin, P. M., *Ap. J. Lett.* **234**, L83 (1979).

Ulaby, Fawwaz T., Moore, Richard K., and Fung, Adrian K., *Microwave Remote Sensing, Active and Passive, Vol. 1*, Addison-Wesley, London (1981).

Weaver, H., and Williams, D. R. W., *Astron. Astrophys. Supp. Ser.* **8**, 1 (1973).

Weinreb, Sander and Kerr, Anthony, *IEEE J. Solid-State Circuits* **SC-8**, 58 (1973).

Weinberg, S., *Gravitation and Cosmology: Principles and Applications of the General Theory of Relativity*, John Wiley and Sons, New York (1972).

Weinberg, S., *The First Three Minutes*, Basic Books, New York (1977).

Weiss, R. W., *Ann. Rev. Astron. Astrophys.* **18**, 489 (1980).

Williams, D. R. and Lum, W., *Microwave Journal* **23**, No. 11, 73, (October 1980).

Wilson, R. W., *Science* **205**, 866 (1979).

Wilson, R. W. and Penzias, A. A., *Science* **156**, 1100 (1967).

Witebsky, C., *Univ. Cal. Berkeley Space Sciences Laboratory Astrophysical Note* **374** *(COBE Memo # 5019)*, unpublished (1978).

Woody, D. P. and Richards, P. L., *Phys. Rev. Lett.* **42**, 925 (1979).

Yahil, A., Tammann, G. A., and Sandage, A., *Ap. J.* **217**, 903 (1977).

Yang, J., Schramm, D., Steigman, G., and Rood, R., *Ap. J.* **227**, 697 (1979).